LINEAR AND MULTILINEAR METHODS FOR GUIDANCE, NAVIGATION, AND CONTROL OF SATELLITE FORMATION FLIGHT

A Dissertation
Presented to the Faculty of the Graduate School
of Cornell University
in Partial Fulfillment of the Requirements for the Degree of
Doctor of Philosophy

by
Jackson Kulik
August 2024

LINEAR AND MULTILINEAR METHODS FOR GUIDANCE, NAVIGATION, AND CONTROL OF SATELLITE FORMATION FLIGHT

Jackson Kulik, Ph.D.

Cornell University 2024

Guidance, navigation, and control of satellites–especially in the study of rendezvous and formation flight–relies heavily on methods that leverage local linear approximations of dynamical systems and measurement functions. This thesis focuses mainly on cases in which linear approximations are insufficient to solve dynamics, control, or estimation problems. In such cases, we employ tools from numerical multilinear algebra on tensors arising from higher-order Taylor series. The inherently quadratic nature of some quantities, the linear unobservability of some estimation problems, and the need to quantify the performance of linear methods make these higher-order techniques useful in the setting of guidance, navigation, and control.

BIOGRAPHICAL SKETCH

Jackson Kulik received his Bachelor of Science in Mathematics from Texas Tech University in May 2020. After graduating, he began studying for a PhD at the Cornell Center for Applied Mathematics as part of the Space Imaging and Optical Systems Lab under Dmitry Savransky. His work on guidance, navigation, and control for relative motion of satellites has been funded by a NASA Student University Research Partnership as well as the DOD National Defense Science and Engineering Fellowship. He interned at the Aerospace Corporation in their Astrodynamics Department for most of his undergraduate career as well as his first year of graduate school. He has also worked at True Anomaly as a Modeling and Simulation Engineer and a Flight Dynamics Engineer during the latter part of his graduate studies. He has particularly enjoyed mentoring Masters, undergraduate, and high school students in his time at Cornell, having supervised just short of a dozen mathematics and engineering projects.

This thesis is dedicated to the students and friends I have worked with during my time at Cornell–you guided me through these last four years.

ACKNOWLEDGEMENTS

I would like to thank a number of people who have brought my life to where it is. My parents seem a good place to start. Thank you for giving me the drive I needed to get here, but even more, thank you for teaching and reminding me to take it easy and enjoy life so that drive is not a pointless thing. I love you very much.

I'm thankful to all my friends who make life sweet. To those far away–thanks for being here for me even when we weren't always here with me. And to all my friends at the Center for Applied Math and Cornell broadly–thank you, you've made this a great place to be.

My mathematics education and outlook on the world was most profoundly impacted by Josh Howard, my geometry teacher; Glenn Hoit, my calculus teacher; Katharine Long, my numerical linear algebra and mathematical physics professor; and Will Clark, my dynamical systems and brewing professor. Thank you all for teaching me. You have all perfected an art.

My practical education in engineering was most shaped by Jason Buhler, my robotics coach; George Pollock, the best manager I'm likely to ever have; Jamie Wilson, a close runner up and my favorite aerospace historian; Matt Schmitt, colleague, mentor, friend, and boss; Andrew Rogers, about whom nothing specific can be said out of an abundance of caution; Tucker Wheeler, partner in crime; Shane Dirks, partner in crime and mentor; Andy Sinclair, my AFRL mentor and one of my favorite authors; and Josue Munoz, a man of boundless technical expertise and experience. Thank you all for inspiring my love of astrodynamics and humoring me while I speak in my slow cadence about math.

Penultimately, I would like to thank my advisor Dmitry Savransky. You have read my work in a timely fashion and always given good, honest, and most of all helpful feedback. You also have a good sense of humor and tell your students to take vacations. Thank you for being flexible while mentoring me. You've shown me how to be a good mentor to my students as well. It's really been a nice time working with you.

Finally, to my partner, Katerina, thank you for supporting me and helping to give direction to my future. I couldn't ask for a better potato friend. I also love you very much.

As a postscript, I would like to thank my cats Izze, Charlie, and Ivy. Izze was there to help me write my first ever paper, and Ivy is here now to help close out my thesis. I thank them for any stray letters or typos the reader might happen upon. Charlie, on the other hand, has not earned a coauthor credit because he is one of the rare sorts of cats that doesn't sit on keyboards.

Table of Contents

List of Tables

List of Figures

CHAPTER 1

INTRODUCTION

The work described in this thesis shares a common setting in addition to a common set of tools. The setting can be described broadly as the fields of dynamics, control, and estimation or–in more standard but not exactly equivalent terminology guidance, navigation, and control (GNC). Guidance, navigation, and control can be described as the study of how a vehicle understands where it is and gets where it wants to go. For a more nuanced understanding of the field as a whole, the *Journal of Guidance Control and Dynamics* (JGCD) recently published a number of very worthwhile articles from the deputy editors discussing the meaning of each term in guidance [88, 87], navigation [25], and control [63] as well as the overall identity of the field.

Most applications in this thesis will focus on guidance, navigation, and control specifically for the relative motion of satellites under either two- or three-body dynamics in the Earth, Sun-Earth, and Earth-Moon systems. Understanding the relative motion of satellites is important in the context of rendezvous, proximity operations, and docking (RPOD)–any activities that involve two satellites getting close together for inspection or in order to make contact for exchange of materials, personnel, or servicing. Understanding relative motion of satellites is also crucial for the study of formation flight, a typically longer-term relative motion in which two or more satellites remain close together for the purpose of some common mission. Some examples of formation flight include historic scientific missions such as the Magnetospheric Multiscale Mission (MMS) [103] as well as mission concepts such as the starshade for directly observing exoplanets [65, 41]. More broadly, formation flight is important for creating lower-cost, redundant, distributed systems of satellites to effectively replace potentially more costly monolithic individual satellites that require exquisite engineering and testing. Keeping these formation flight and RPOD applications in mind, each chapter in this thesis will employ a common methodology that takes advantage of the proximity of the satellites.

Performing the Taylor expansion of dynamics and measurement functions around the orbit of one satellite or an orbit near both satellites is a standard approach to simplify the study of relative motion of satellites. When the motion takes place on a smaller distance scale as compared with the scale of the dynamical system as a whole, low-order Taylor expansions form a good approximation of the full nonlinear function. Within the GNC field, first-order approximations of dynamics or measurements are the most common Taylor-expansion. Linearization of the flow of a satellite orbit dates back at least to the work of Hill and his Lunar theory [51], but finds its modern setting with artificial satellites during the space race with the work of Clohessy and Wiltshire [24]. The simplest application of linearized dynamics is to approximately propagate the motion of one satellite relative to another nearby satellite. However, linear approximations of dynamics are used for more than propagation in a number of guidance, navigation, and control algorithms that involve applying linear algebraic methods to solve inverse problems pertaining to the dynamics. This thesis discusses some of these linear methods and introduces new analysis with them in the first two chapters. Beyond employing just the first term in the Taylor series, taking additional terms in the expansion can increase the accuracy of propagation of relative motion. However, the second- and higher-order coefficients of a Taylor series of a vector-valued multivariate function, such as the flow of a dynamical system, are third- and higher-order tensors. In practice, these higher-order Taylor series can be difficult to apply to the solution of interesting problems in the context of GNC algorithms because techniques from numerical linear algebra cannot be applied directly to the tensors arising in the higher-order expansion. However, some ad hoc approaches involving slicing these tensors or linearizing the multilinear operators they represent can be employed to solve problems that require higher-order methods. These approaches are the subject of the penultimate two chapters of this thesis as applied to problems in optimal control and orbit determination. Further, recent advances in the numerical analysis of tensors can be applied to gain new understanding and tools for the analysis of algorithms for guidance, navigation, and control based on linearization or higher-order series reversion. These advances underpin the final chapter of the thesis which utilizes generalizations of eigenvalues to tensors in order to study the linearization error introduced by common GNC algorithms. Before developing these novel methods in the remainder of the thesis, we will begin by reviewing two- and three-body dynamics, summarizing the tensors arising in GNC, and finally presenting series reversions methods for vector-valued multivariate functions.

1.1 Dynamics

In the following examples, we will be considering Keplerian two-body dynamics as well as circular restricted three body dynamics, which we will define here.

1.1.1 Two-Body Dynamics

The equations of motion for the two-body problem in an inertial frame are

$$\mathbf{F}(\mathbf{x}) = \begin{bmatrix} \dot{x} \\ \dot{y} \\ \dot{z} \\ \frac{-\mu x}{||\mathbf{r}||^{3/2}} \\ \frac{-\mu y}{||\mathbf{r}||^{3/2}} \\ \frac{-\mu z}{||\mathbf{r}||^{3/2}} \end{bmatrix} \tag{1.1}$$

where the state vector is $\mathbf{x} = [x, y, z, \dot{x}, \dot{y}, \dot{z}]^T$, an overdot denotes a time derivative, μ represents the standard gravitational parameter for the central body, and $\mathbf{r} = [x, y, z]^T$ is the position vector from the central body to the satellite [126].

1.1.2 Circular Restricted Three Body Dynamics

The equations of motion for the circular restricted three-body problem are given in the synodic frame as

$$\mathbf{F}(\mathbf{x}) = \begin{bmatrix} \dot{x} \\ \dot{y} \\ \dot{z} \\ 2\dot{y} + \frac{\partial \overline{U}}{\partial x} \\ -2\dot{x} + \frac{\partial \overline{U}}{\partial y} \\ \frac{\partial \overline{U}}{\partial z} \end{bmatrix} \tag{1.2}$$

where $\overline{U}(x, y, z) = \dfrac{1-\mu^*}{||\mathbf{r}_1||} + \dfrac{\mu^*}{||\mathbf{r}_2||} + \dfrac{x^2+y^2}{2}$ is the effective potential given the reduced mass $\mu^* = \dfrac{m_2}{m_1+m_2}$ for the two primary bodies with mass m_1, m_2 located along the x-axis at $[-\mu^*, 0, 0]$ and $[1-\mu^*, 0, 0]$ with respect to their common barycenter at the origin. $\mathbf{r}_1, \mathbf{r}_2$ give the position of the satellite of interest with respect to the two primary bodies, respectively [71].

1.2 Tensors in Guidance Navigation and Control

1.2.1 Local Dynamics Tensors

Given an autonomous dynamical system in $\mathbb{R}^n$, the state vector $\mathbf{x} \in \mathbb{R}^n$ evolves according to the system of ordinary differential equations

$$\frac{d}{dt}\mathbf{x} = \mathbf{F}(\mathbf{x}), \quad \mathbf{x}(0) = \mathbf{x}_0 \tag{1.3}$$

Local dynamics tensors are defined as the partial derivative tensors of the vector field $\mathbf{F}(\mathbf{x})$ evaluated at some point $\mathbf{x}^*$:

$$\left[\left(\frac{\partial^m \mathbf{F}}{\partial \mathbf{x}^m}\right)\bigg|_{\mathbf{x}^*}\right]^i_{j_1 \dots j_m} = \left(\frac{\partial F^i}{\partial x^{j_1} \dots \partial x^{j_m}}\right)\bigg|_{\mathbf{x}^*} \tag{1.4}$$

The mth order local dynamics tensor is a $(1, m)$-tensor, where an (l, m)-tensor has m covariant indices and l contravariant indices. An interpretation of this is that the tensor operates on m vectors or m copies of a single vector to produce one vector as a result. Since a dynamical system evolves so that $\mathbf{x}^*$ changes over time, local dynamics tensors are most meaningful on their own at equilibria of that dynamical system. Analysis of the eigenvalues of these tensors has been discussed in previous literature [54], and is not expanded upon here. However, local dynamics tensors are a necessary for calculating partial derivative tensors of the flow of the dynamical system.

1.2.2 State Transition Tensors

The first and second-order variational equations associated with a dynamical system are derived in Ref. [102]. The notion of state transition tensors is also explored in Refs. [95, 8]. We will describe commonly known properties of the state transition matrix in both matrix and component form to build intuition for properties of the second-order variational state transition tensor which is most clearly described in component form.

Given an autonomous dynamical system in $\mathbb{R}^n$, the state vector $\mathbf{x}$ evolves according to the system of ordinary differential equations

$$\frac{d}{dt}\mathbf{x} = \mathbf{F}(\mathbf{x}), \quad \mathbf{x}(0) = \mathbf{x}_0 \tag{1.5}$$

The associated flow map is defined such that

$$\frac{d}{dt}\varphi_t(\mathbf{x}) = \mathbf{F}(\varphi_t(\mathbf{x})), \quad \varphi_0(\mathbf{x}) = \mathbf{x} \tag{1.6}$$

The flow map possesses the semigroup property in time

$$\varphi_t \circ \varphi_s = \varphi_{t+s} \tag{1.7}$$

The Jacobian of the flow map yields the state transition matrix (STM) $\mathbf{\Phi}(\mathbf{x}_0; t, 0)$ associated with a given flow starting at the reference state $\mathbf{x}_0$ from time 0 to time t. We adopt indexing for the state transition matrix rows i and columns j

$$\mathbf{\Phi}^i_j(\mathbf{x}_0; t, 0) = \frac{\partial \varphi^i_t(\mathbf{x}_0)}{\partial x^j_0} \tag{1.8}$$

where the upper index i of the flow map refers to the ith component of the output. When the reference orbit initial state $\mathbf{x}_0$ is understood, the state transition matrix will be abbreviated as simply $\mathbf{\Phi}(t, 0)$. Exchanging the order of temporal and spatial derivatives (assuming F has continuous spatial derivatives) and applying the chain rule yields the n^2 first-order variational equations

$$\frac{d\mathbf{\Phi}(t,0)}{dt} = \frac{\partial \mathbf{F}(\mathbf{x})}{\partial \mathbf{x}}\mathbf{\Phi}(t,0), \quad \mathbf{\Phi}(0,0) = I_n \tag{1.9}$$

where I_n gives the n by n identity matrix. Alternatively, in components where summation with respect to l is understood and δ^i_j is the Kronecker delta

$$\frac{d\mathbf{\Phi}^i_j(t,0)}{dt} = \frac{\partial F_i(\mathbf{x})}{\partial x_l}\mathbf{\Phi}^l_j(t,0), \quad \mathbf{\Phi}^i_j(0,0) = \delta^i_j \tag{1.10}$$

The cocycle property is most recognizable in matrix form and stems from application of the chain rule to the semigroup property

$$\mathbf{\Phi}(t_2,t_0) = \mathbf{\Phi}(t_2,t_1)\mathbf{\Phi}(t_1,t_0) \tag{1.11}$$

or, in components

$$\mathbf{\Phi}^i_j(t_2,t_0) = \mathbf{\Phi}^i_l(t_2,t_1)\mathbf{\Phi}^l_j(t_1,t_0) \tag{1.12}$$

Note that the relationship in Eq. 1.12 is not commutative. Given knowledge of the STM over the entire time interval and the STM over the initial stage, the STM over the latter subinterval can be calculated with the inverse matrix $\mathbf{\Phi}^{-1}(t_1,t_0)$

$$\mathbf{\Phi}(t_2,t_1) = \mathbf{\Phi}(t_2,t_0)\mathbf{\Phi}^{-1}(t_1,t_0) \tag{1.13}$$

Moving on to the second-order variational equations, we define the second-order (2,1)-state transition tensor (STT) $\mathbf{\Psi}(t,0)$

$$\mathbf{\Psi}^i_{j,k}(\mathbf{x}_0;t,0) = \frac{\partial^2 \varphi^i_t(\mathbf{x}_0)}{\partial x^j_0 \partial x^k_0} \tag{1.14}$$

Again, when the reference orbit initial state $\mathbf{x}_0$ is understood, the notation $\mathbf{\Psi}(t,0)$ will be used to denote the second-order state transition tensor. Applying the product rule to Eq. 1.10, we find that the n^3 equations in Eq. 1.15 depend not only on the values of $\mathbf{\Psi}$ but also $\mathbf{\Phi}$

$$\frac{d\mathbf{\Psi}^i_{j,k}(t,0)}{dt} = \frac{\partial^2 F_i(\mathbf{x})}{\partial x_l \partial x_q}\mathbf{\Phi}^l_j(t,0)\mathbf{\Phi}^q_k(t,0) + \frac{\partial F_i(\mathbf{x})}{\partial x_l}\mathbf{\Psi}^l_{j,k}(t,0), \quad \mathbf{\Psi}^i_{j,k}(0,0) = 0 \tag{1.15}$$

The second-order generalization to the cocycle conditions come from differentiating Eq. 1.12

$$\boldsymbol{\Psi}^i_{j,k}(t_2,t_0) = \boldsymbol{\Psi}^i_{l,m}(t_2,t_1)\boldsymbol{\Phi}^l_j(t_1,t_0)\boldsymbol{\Phi}^m_k(t_1,t_0) + \boldsymbol{\Phi}^i_l(t_2,t_1)\boldsymbol{\Psi}^l_{j,k}(t_1,t_0) \tag{1.16}$$

Given STTs for the overall time interval and along the initial subinterval, the second-order STT over the latter subinterval can be calculated after finding the STM along the latter subinterval with Eq. 1.13

$$\boldsymbol{\Psi}^i_{j,k}(t_2,t_1) = [\boldsymbol{\Psi}^i_{l,m}(t_2,t_0) - \boldsymbol{\Phi}^i_q(t_2,t_1)\boldsymbol{\Psi}^q_{l,m}(t_1,t_0)](\boldsymbol{\Phi}^{-1})^l_j(t_1,t_0)(\boldsymbol{\Phi}^{-1})^m_k(t_1,t_0) \tag{1.17}$$

This relationship is exact but requires one more level of contraction than the approximate solution presented in [31] by using the STTs associated with the inverse flow map. With the STM and second-order STT, a second-order approximation of a perturbation to the flow map is given by a truncated Taylor series:

$$\varphi^i_t(\mathbf{x}_0 + \delta\mathbf{x}_0) \approx \varphi^i_t(\mathbf{x}_0) + \boldsymbol{\Phi}^i_j(\mathbf{x}_0; t, 0)\delta x^j_0 + \frac{1}{2}\boldsymbol{\Psi}^i_{jk}(\mathbf{x}_0; t, 0)\delta x^j_0 \delta x^k_0 \tag{1.18}$$

or, in shorthand to represent the single and double contractions:

$$\varphi_t(\mathbf{x}_0 + \delta\mathbf{x}_0) \approx \varphi_t(\mathbf{x}_0) + \boldsymbol{\Phi}(\mathbf{x}_0; t_f, t_0)\delta\mathbf{x}_0 + \frac{1}{2}\boldsymbol{\Psi}(\mathbf{x}_0; t_f, t_0)\delta\mathbf{x}^2_0 \tag{1.19}$$

Variational equations and cocycle conditions describing the sensitivity of states with respect to fixed parameters can be derived [92]. However, these are typically only presented up to first-order, because they become increasingly complex as mixed partial derivatives of states and parameters appear at higher-orders. To avoid these complications, we note that parameters are simply state variables from an augmented dynamical system in which the parameters have zero time derivatives. Thus, sensitivities with respect to these parameters can be handled without deriving specific equations treating parameters separately from state variables.

This is potentially less efficient than treating these equations separately, but the additional cost only comes from additional multiplications and additions of zero when performing numerical integration or using cocycle conditions. Higher-order state transition tensors and variational equations can be derived [14], though we will only deal with the first two state transition tensors in this work. Some applications of state transition tensors are summarized in the applications section of this thesis; however, more information on higher-order state transition tensors, their analytical computation [62], and their applications for dynamics [102, 8, 26], control [12, 73], and navigation/uncertainty propagation [95, 90, 10, 74] exists across the literature of the last few decades. Parallel to the state transition tensor approach, differential algebra (DA) [101] is a technique for computing the Taylor expansion of an arbitrary function whether it be the flow of a dynamical system or another arbitrary nonlinear function. While DA is not employed in this paper, computing state transition tensors using higher-order variational equations becomes increasingly complicated at each order. As such, the DA approach offers a more convenient and typically efficient approach for computing the Taylor series up to a given order, from which the coefficients can be trivially collected into the corresponding partial derivative tensors such as state transition tensors. DA has been employed for uncertainty propagation [127, 134], filtering [108], orbit determination [7], and control purposes among others [33, 83]. Many of the algorithms described in the DA literature leverage efficient computations for manipulating formal power series and approximating the inverse of a truncated series. These methods can be used to efficiently obtain tensors related to and arising from the state transition tensor series such as the inverse flow of the system or the higher-order Cauchy-Green strain tensors described below.

1.2.3 Higher-Order Cauchy-Green Strain Tensors

Higher-order Cauchy-Green strain tensors are the coefficient tensors arising in the series expansion for the squared 2-norm of the final perturbation of a dynamical system as a function of some initial perturbation. These tensors were introduced to examine the stretching behavior of a dynamical system around some reference trajectory as well as the associated nonlinearity index [54, 55].

$$\delta\mathbf{x}^T(t_f)\delta\mathbf{x}(t_f) = \sum_{m=2}^{\infty} \mathbf{C}^{(m)}\delta\mathbf{x}_0^m = \sum_{p,q\geq 1}^{\infty} \frac{1}{p!q!}\left(\mathbf{\Psi}^{(p)}\delta\mathbf{x}^p(t_0)\right)^T\left(\mathbf{\Psi}^{(q)}\delta\mathbf{x}^q(t_0)\right) \tag{1.20}$$

where $\mathbf{C}^{(m)}$ is the mth order Cauchy-Green strain tensor. This series converges assuming that the flow map is infinitely differentiable. Note that the higher-order Cauchy-Green strain tensors are covariant and not generally supersymmetric except in the case of the first-order 2-tensor. These tensors can be calculated in component form in terms of the Euclidean metric tensor $g_{i,j} = \delta_{i,j}$ which is simply the Kronecker delta:

$$C_{i_1 \ldots i_m} = \sum_{p+q=m;p,q\geq 1} \frac{1}{p!q!} \Psi^{j_1}_{i_1\ldots i_p}\delta_{j_1,j_2}\Psi^{j_2}_{i_{p+1}\ldots i_m} \tag{1.21}$$

The first Cauchy-Green strain tensor is given by the square of the state transition matrix $\mathbf{C}^{(2)} = \mathbf{\Phi}^T\mathbf{\Phi}$, where the matrix is understood to represent a covariant (0,2)-tensorNotably, the singular value decomposition of the state transition matrix yields right singular vectors that are the same as the eigenvectors of the Cauchy-Green strain tensor, and singular values that are the same as the square root of the eigenvalues of the Cauchy-Green strain tensor. In a similar fashion, tensor eigenvalues of the higher-order Cauchy-Green strain tensors describe the stretching behavior of the higher-order terms in the state transition tensor series. For study with tensor eigenvalues, the supersymmetric tensor denoted $\hat{\mathbf{C}}^{(m)}$ is often used in calculations and surrounding theory. This is a tensor which produces the same result as $\mathbf{C}^{(m)}$ when operating on the same m vectors, but is supersymmetric. Details about symmetrization, as well as avoiding symmetrization in calculations can be found in Sec. 6.2.4 and Appendix B.1.

1.2.4 Measurement Partial Derivative Tensors

Given a d-dimensional measurement function $h(x) : \mathbb{R}^n \to \mathbb{R}^d$, the partial derivative tensors of this function play a role in some higher-order estimation algorithms such as the $\jmath$th-moment Kalman filter [89] as well as in the context of assessing the error in using linearizations of measurement function for measurement underweighting schemes in Kalman filters [89, 138]. The order $(1, m)$ partial derivative tensors arise in the Taylor series expansion of the measurement function about some prior estimated state $\mathbf{x}^-$

$$\mathbf{h}(\mathbf{x}^- + \delta\mathbf{x}) = \mathbf{h}(\mathbf{x}^-) + \sum_{m=1}^{\infty} \frac{1}{m!} \left(\frac{\partial^m \mathbf{h}}{\partial \mathbf{x}^m} \right)_{\mathbf{x}=\mathbf{x}^-} \delta\mathbf{x}^m \tag{1.22}$$

In this work, we particularly look at the first- and second-order partial derivatives from the series above.

1.3 Series Reversion

Series reversion or inversion of series is a powerful classical technique for approximating the inverse of a function. Here, we review the single variable and multiple variable cases. These methods will feature in the final chapter of the thesis to describe the Taylor series involved with a certain guidance problem.

1.3.1 Single Variable Case

Given a scalar-valued formal power series in terms of a single variable

$$y = f(x) = a_1 x + a_2 x^2 + ... \tag{1.23}$$

the inverse formal power series can be computed if $a_1 \neq 0$ such that the composition of the two series results in the identity mapping

$$x = g(y) = b_1 y + b_2 y^2 + ... \tag{1.24}$$

The coefficients of the inverse series can be computed by equating coefficients in the equation

$$\begin{aligned} y &= f(g(y)) && (1.25) \\ &= a_1 b_1 y + (a_1 b_2 + a_2 b_1^2) y^2 + (a_1 b_3 + 2 a_2 b_1 b_2 + a_3 b_1^3) y^3 + ... && (1.26) \end{aligned}$$

where the first coefficient should be unity and all remaining coefficients should be zero. The first few coefficients of the inverse series are

$$b_1 = a_1^{-1} \tag{1.27}$$

$$b_2 = -a_1^{-3} a_2 \tag{1.28}$$

$$b_3 = 2 a_1^{-5} a_2^2 - a_1^{-4} a_3 \tag{1.29}$$

1.3.2 Multivariate Generalization

Multivariate generalizations of series reversion and Lagrange inversion theorem have been discussed generally in the astrodynamics literature [125, 59]. These techniques have been used in particular for higher-order guidance calculations (solving Lambert's problem approximately in the vicinity of some reference orbit) in the state transition tensor and differential algebra literature [49, 83, 139].

In order to generalize series reversion to multivariate functions $\mathbf{F} : \mathbb{R}^n \longrightarrow \mathbb{R}^n$, we note the connection to Newton's method in the process above where we equated coefficients. First, let the ith component of the output $\mathbf{y}$ be defined as

$$y^i = (\mathbf{F}(\mathbf{x}))^i = A^i_{j_1} x^{j_1} + A^i_{j_1,j_2} x^{j_1} x^{j_2} ... \tag{1.30}$$

where the number of lower indices implicitly defines the order in the series for the given coefficient tensor $\mathbf{A}^{(m)}$. We will define the mth order truncated power series associated with $\mathbf{F}$ by

$$\mathbf{F}(\mathbf{x}) = \mathbf{F}^{(m)}(\mathbf{x}) + \mathcal{O}(\mathbf{x}^{m+1}) \tag{1.31}$$

If we express the inverse series as

$$x^i = (\mathbf{G}(\mathbf{y}))^i = B^i_{j_1} y^{j_1} + B^i_{j_1,j_2} y^{j_1} y^{j_2} ... \tag{1.32}$$

then the first-order approximation of $\mathbf{G}$ is given by solving for the coefficient tensor $\mathbf{B}^{(1)}$ (matrix in this case) that satisfies

$$y^i = A^i_j B^j_k y^k \tag{1.33}$$

this is given by

$$\mathbf{B}^{(1)} = (\mathbf{A}^{(1)})^{-1} \tag{1.34}$$

if the first term is invertible. Thus, the first-order approximation of the inverse series is given by the inverse of the first-order term in the original series

$$\left(\mathbf{G}^{(1)}(\mathbf{y})\right)^i = \left((\mathbf{A}^{(1)})^{-1}\right)^i_j y^j \tag{1.35}$$

The higher-order approximations of the inverse series can be iteratively obtained using Newton's method in the following fashion

$$\left(\mathbf{G}^{(m+1)}(\mathbf{y}) - \mathbf{G}^{(m)}(\mathbf{y})\right)^i = -\left((\mathbf{A}^{(1)})^{-1}\right)^i_l \left(\left(\mathbf{F}(\mathbf{G}^{(m)}(\mathbf{y}))\right)^{(m+1)} - \mathbf{y}\right)^l_{j_1 \cdots j_{m+1}} \tag{1.36}$$

where $\left(\mathbf{F}(\mathbf{G}^{(m)}(\mathbf{y}))\right)^{(m+1)}$ is the $(m+1)$-th order approximation of the residual from composition of the forward series with the inverse series:

$$\mathbf{F}(\mathbf{G}^{(m)}(\mathbf{y})) = \left(\mathbf{F}(\mathbf{G}^{(m)}(\mathbf{y}))\right)^{(m+1)} + \mathcal{O}(\mathbf{y}^{m+2}) \tag{1.37}$$

This is the linear polynomial $\mathbf{y}$ summed with an $(m+1)$-th order homogeneous polynomial in $\mathbf{y}$, because $\mathbf{G}^{(m)}(\mathbf{y})$ is constructed so that the m-th order approximation of the composition is the identity mapping

$$\left(\mathbf{F}(\mathbf{G}^{(m)}(\mathbf{y}))\right)^{(m)} = \mathbf{y} \tag{1.38}$$

Using this Newton iteration approach, the first couple terms in the general multivariate series reversion are given by

$$B^i_j = \left((A^{(1)})^{-1}\right)^i_j \tag{1.39}$$

$$B^i_{j,k} = -\left((A^{(1)})^{-1}\right)^i_{l_1} A^{l_1}_{l_2,l_3} \left((A^{(1)})^{-1}\right)^{l_2}_j \left((A^{(1)})^{-1}\right)^{l_3}_k \tag{1.40}$$

Implementation of this procedure is easily possible using differential algebra techniques and is a part of many standard packages for differential algebra. For more than the first few terms in the inverse series, one should fall back to one of these computational tools [101].

CHAPTER 2

STARSHADE STATIONKEEPING ANALYSIS VIA EIGENVECTORS OF THE ACCELERATION JACOBIAN

2.1 Introduction

Given a space-based telescope, nominally along an Earth-Sun L2 Halo orbit, a starshade located at a fixed distance from the telescope, and a target star, we analyze the costs and timing metrics associated with maintaining the starshade in a nominal position, within some tolerance, to block out light from the given star. Our work is in the same vein as previous analyses from [38, 113, 117]; however, we take a more approximate analytical approach with the goal of furthering understanding and speeding up computation. We model the use of impulsive burns to maintain the starshade within a one meter lateral tolerance of the line of sight between telescope and target star [107]. Fuel costs and number of stationkeeping maneuvers required during an observation can serve as important considerations in deciding between target stars for observation. These stationkeeping metrics may be used in an objective function that would ideally evaluate quickly as part of a larger scheduling problem optimization such as those described in [60, 104, 115, 116].

A stationkeeping strategy that maximizes time between impulsive burns is given by [38]. This strategy for deadbanding assumes constant differential acceleration between telescope and starshade. The authors of [117] further explored this strategy in a variety of scenarios, analyzing a wider variety of pertinent stationkeeping metrics. Both papers numerically solved ordinary differential equations (ODEs) with event driven application of the impulses to find stationkeeping metrics. This is a computationally expensive operation and it would not be desirable to carry out these integrations as part of a larger mission design optimization process, motivating the need for a fast method to approximate the stationkeeping metrics, and a comparison of its accuracy with respect to the methods above.

We summarize the work of [38], and then compare their analytical strategy under ideal conditions against numerical results from [117]. This serves to validate the use of the inexpensive analytical model for stationkeeping. From there, we continue the linear analysis of [38] on the lateral differential acceleration, focusing on the locations of its minima. We present a geometric picture of differential lateral acceleration, and an analytical expression to approximate these locations associated with low stationkeeping costs. Among starshade positions constrained to the surface of a sphere centered about the telescope, minima of differential lateral acceleration lie on a great circle and its corresponding poles. This intuition and analytical expression for the minima could be used as a heuristic to reduce the design space for scheduling of an exoplanet imaging mission.

2.2 Analytical Model of Station Keeping Metrics

We consider the inertial accelerations of the telescope $\mathbf{a}_t$ and starshade $\mathbf{a}_s$ with respect to the inertially non-accelerating barycenter at an initial epoch, and then assume that the differences in inertial accelerations between satellites remain constant over the course of the observation. In the inertial frame, this maintains the direction of the relative position vector $\mathbf{r}_{\text{rel}}$ between the starshade at $\mathbf{r}_s$ and telescope at $\mathbf{r}_t$, preserving alignment of the telescope, starshade, and target. For convenience, consider an inertial frame which happens to be aligned with the circular restricted three body problem (CR3BP) rotating frame at the initial epoch and in units of AU. The frame is depicted in Fig. 2.1 with the Earth-Sun barycenter located at the origin. Consider all accelerations from this point forward as inertial.

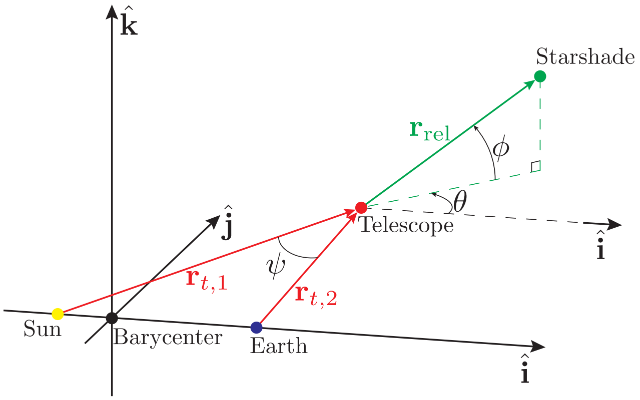

Figure 2.1: The coordinate frame employed in this paper with relevant bodies and angles depicted.

In the inertial reference frame, the acceleration of satellite $j = t, s$ from two bodies is given by

$$\mathbf{a}_j = \mathbf{a}_{j,1} + \mathbf{a}_{j,2} \tag{2.1}$$

$$\mathbf{a}_{j,1} = \frac{(\mu - 1)(\mathbf{r}_j + \mu\hat{\mathbf{i}})}{||\mathbf{r}_j + \mu\hat{\mathbf{i}}||^3} \tag{2.2}$$

$$\mathbf{a}_{j,2} = \frac{-\mu\big(\mathbf{r}_j + (\mu - 1)\hat{\mathbf{i}}\big)}{||\mathbf{r}_j + (\mu - 1)\hat{\mathbf{i}}||^3} \tag{2.3}$$

where μ is the mass parameter, subscript 1 refers to the primary body (the Sun), 2 refers to the secondary body (the Earth), $\hat{\mathbf{i}}$ is the unit vector in the Sun-Earth direction, and $\mathbf{r}$ refers to position. The Sun is assumed to be at $-\mu\hat{\mathbf{i}}$ and the Earth at $(1 - \mu)\hat{\mathbf{i}}$.

The differential acceleration between starshade and telescope is given by the difference in the inertial second time derivatives of position

$$\delta\mathbf{a} = \mathbf{a}_s - \mathbf{a}_t = \ddot{\mathbf{r}}_s - \ddot{\mathbf{r}}_t. \tag{2.4}$$

Starshade position is nominally given by

$$\mathbf{r}_s = \mathbf{r}_t + R(\cos\phi\cos\theta\hat{\mathbf{i}} + \cos\phi\sin\theta\hat{\mathbf{j}} + \sin\phi\hat{\mathbf{k}}) \tag{2.5}$$

where, as seen in Fig. 2.1, $R = \|\mathbf{r}_{\text{rel}}\|$ is the nominal telescope-starshade separation distance, θ, the ecliptic longitude, is the in-plane angle of the star from the Sun-Earth vector at the starting epoch, and ϕ, the ecliptic latitude, is the out-of-plane angle measured from the ecliptic plane as measured with respect to the starshade location.

Consider the axial and lateral components of the differential acceleration, where axial denotes the direction of the telescope line of sight to the target star, and lateral denotes the component orthogonal to the line of sight. The lateral differential acceleration magnitude is given by:

$$\delta a_l = ||\delta\mathbf{a} - (\delta\mathbf{a}\cdot\hat{\mathbf{r}}_{\text{rel}})\hat{\mathbf{r}}_{\text{rel}}||\,, \tag{2.6}$$

where

$$\hat{\mathbf{r}}_{\text{rel}} = \cos\phi\cos\theta\hat{\mathbf{i}} + \cos\phi\sin\theta\hat{\mathbf{j}} + \sin\phi\hat{\mathbf{k}}$$

The starshade has a nominal relative position with respect to the telescope and a lateral tolerance r_{tol} from this position. We consider lateral stationkeeping, disregarding axial stationkeeping, because axial tolerances are typically larger than the distances traversed during a typical observation [117].

In the optimal strategy outlined in [38], the starshade begins some nominal axial distance from the telescope and at the edge of the r_{tol} lateral tolerance disc in the direction of lateral relative acceleration. The starshade is initialized with lateral relative velocity chosen in the opposite direction of lateral relative acceleration.

The magnitude of the velocity is chosen such that the starshade will reach the exact opposite end of the disk with radius given by the lateral tolerance, and then come back down to its initial position under the constant lateral acceleration. At this point, the starshade applies an impulsive burn to repeat the process. The resulting stationkeeping metrics are given as follows:

$$T = 4\sqrt{\frac{r_{\mathrm{tol}}}{\delta a_l}} \tag{2.7}$$

$$N = \mathrm{floor}\left(\frac{\tau_{\mathrm{obs}}\sqrt{\delta a_l}}{4\sqrt{r_{\mathrm{tol}}}}\right) \tag{2.8}$$

$$\Delta \mathrm{v} = 4N\sqrt{\delta a_l r_{\mathrm{tol}}}\,, \tag{2.9}$$

where τ_{obs} is the overall observation/stationkeeping time, T is the amount of time between impulsive burns, N is the number of burns after the initial epoch (not counting the initialization of the starshade), and Δv is the cost in terms of impulsive velocity changes to perform the stationkeeping. These results were presented in nondimensional form in more generality for arbitrary initialization positions on the tolerance disk [38]. Notice that Δv is largely independent of the stationkeeping tolerance, and varies as $\tau\delta a_l$, the product of observation time and acceleration magnitude. We can obtain various other metrics as a function of these as in [117].

These metrics are relatively simple to evaluate compared to the numerical solution of an ODE that depends on repeatedly evaluating the differential acceleration. As each of these metrics depends simply on differential lateral acceleration, we study this quantity as a proxy. A plot of lateral differential acceleration is given in Fig. 8 of [38]. However, only a small region around a maximum is depicted as worst case scenarios were the primary focus of the work. The overall structure of the differential acceleration is not given, and in particular, the minima are not shown. Fig. 2.2 sheds some light on the structure of differential lateral acceleration and resembles the color plots seen in Fig. 9 of [117]. Looking at

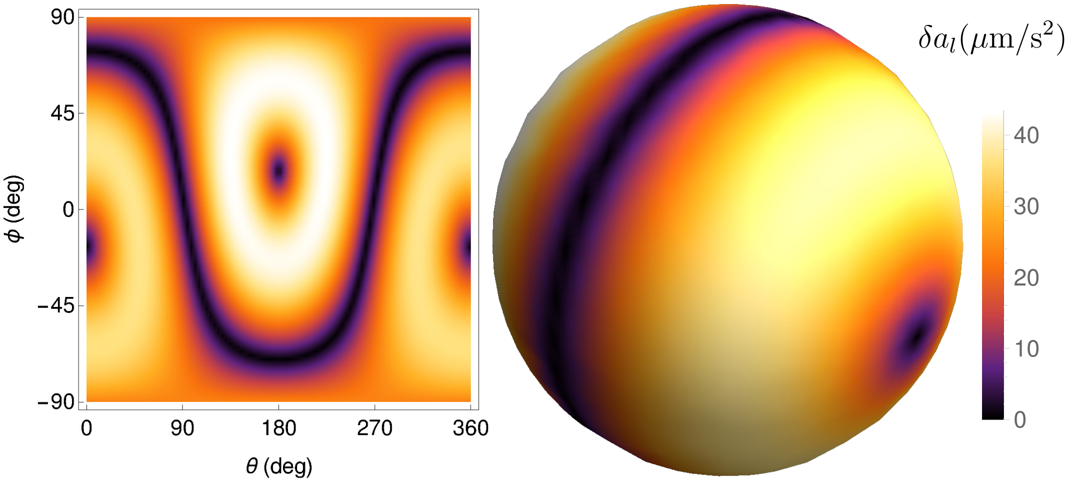

Figure 2.2: The differential lateral acceleration in $\mu\text{m/s}^2$ as a function of target coordinates. The density plot on the left is accompanied by its projection onto the unit sphere on the right.

the same data plotted over the unit sphere centered about the telescope, we can understand that the minima of lateral acceleration magnitude lie on a great circle and its corresponding poles. In Fig. 2.2, the telescope is assumed to be at $(x, y, z) = (1 + 2.5/150, 0, 1/150)$. The starshade is assumed to be $R = 100,000$ kilometers away from the telescope. The existence of the great circle and poles can be explained by the rejection of the axial component of acceleration: Fig. 2.3 shows a plot of the differential acceleration vector field, demonstrating that the vector field is orthogonal to the sphere in the axial or anti-axial direction along the same great circle and at the two corresponding poles. More specifically, the vector field in Fig. 2.3 points outwards on the far left and right, and then inwards towards the origin along the circle lying between the two extreme points. We also depict the cosine of the angle between relative position and differential acceleration in Fig. 2.3. This gives a less intuitive but more clear representation of the direction of the differential acceleration vector. Values of $-1, 0, 1$ correspond to differential acceleration that is purely anti-axial, lateral, and axial respectively.

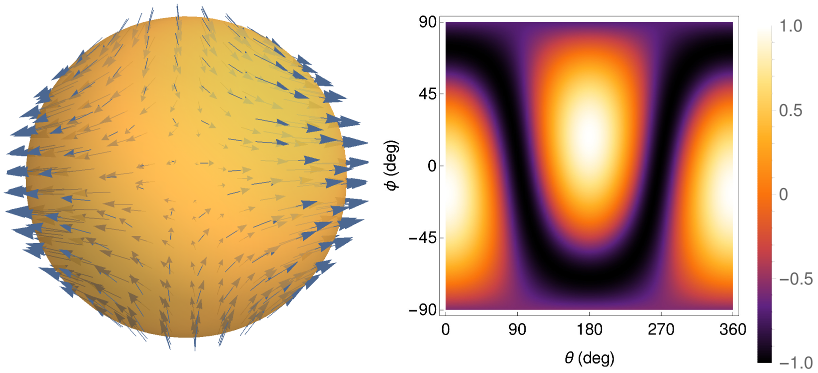

Figure 2.3: On the left, the differential acceleration vector field along the unit sphere about the telescope. On the right, the cosine of the angle between relative position and differential acceleration.

Figure 2.4 demonstrates the similarity between the numerically computed and analytically computed Δv metric for a telescope 340 days from initialization of the halo orbit. Analytical computation is described above, while the numerical computation is carried out with only gravitational effects as in [117]. We see that the two metrics agree very well except along the minima of Δv, where they differ by up to half of the analytical value. The effects of nonconstant differential lateral acceleration are a plausible explanation of these differences. It is reasonable to believe that at these minima induced by the direction of differential acceleration, small changes in differential acceleration direction would have greater effects than at other locations. However, the overall structure from the two approaches is the same, with minima in the nearly the same locations.

2.3 Approximate Minima of Lateral Acceleration

The location of one of the poles shown in Fig. 2.2 can be computed by numerical minimization. Along our six month reference halo orbit depicted in Fig. 2.5, we give the angular locations of the pole in Fig. 2.6.

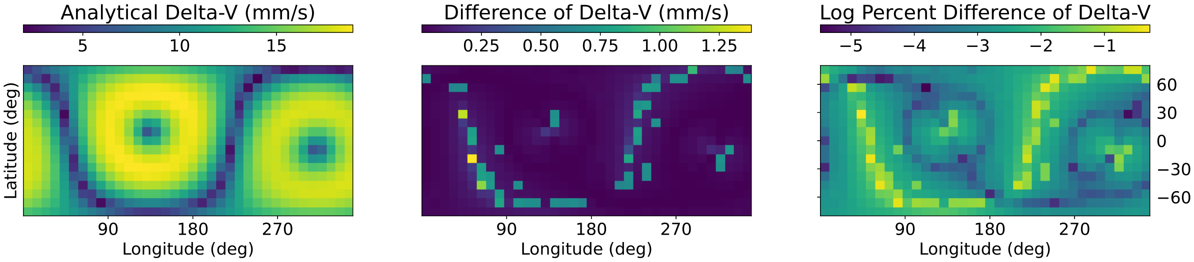

Figure 2.4: Comparison between numerical and analytical models of the average delta-v to perform a single stationkeeping impulse in mm/s during an observation at 340 days from the start of the reference halo orbit.

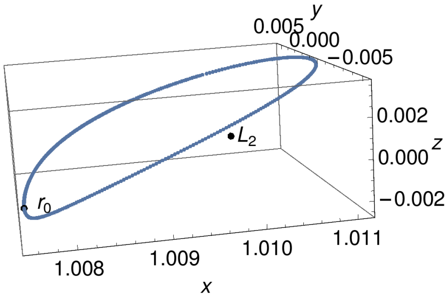

Figure 2.5: The six month period reference halo orbit, with the initial position labeled in canonical units of the CR3BP.

Employing a poor initial guess can cause numerical methods to identify minima along the great circle rather than the pole. Serving as an initial guess for numerical minimization, a quick approximation of the pole's location can be obtained from the eigenvectors of the Jacobian matrix D of the inertial acceleration vector of the telescope.

$$\delta \mathbf{a}(\mathbf{r}_t) = \mathbf{a}(\mathbf{r}_t + \mathbf{r}_{\text{rel}}) - \mathbf{a}(\mathbf{r}_t) \approx D\mathbf{a}(\mathbf{r}_t) \cdot \mathbf{r}_{\text{rel}} \tag{2.10}$$

Equation 2.10 demonstrates that differential acceleration will be completely

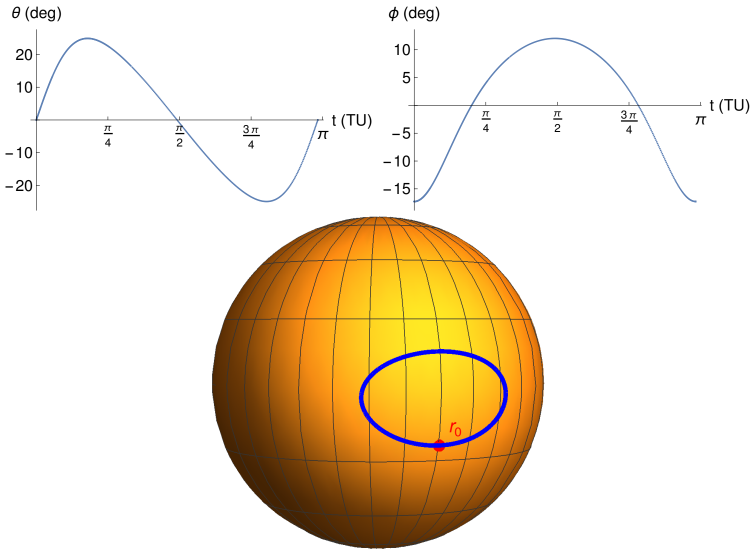

Figure 2.6: Pole location as the telescope moves along the reference halo orbit trajectory in terms of ecliptic longitude, latitude and location on the unit sphere.

axial in the corresponding linear system precisely when the differential acceleration $\delta\mathbf{a}(\mathbf{r}_t)$ is parallel or antiparallel to the offset vector between telescope and starshade $\mathbf{r}_{\text{rel}}$. This is the case when $\mathbf{r}_{\text{rel}}$ is an eigenvector of $D\mathbf{a}(\mathbf{r}_t)$. Given the structure of the vector field in Fig. 2.3, the eigenvector corresponding to the pole will be the one corresponding to a positive eigenvalue. The other two eigenvectors correspond to points on the great circle. In the case of our reference halo orbit, the difference in angular position of the pole between the numerical method in Fig. 2.6 and the linear approximation is on the order of a degree for $R = 100,000$km, scaling linearly with R.

Even with the relatively easy to compute and robust eigenvector interpretation, we still seek an analytical expression for the pole locations. We begin by approximating the differential acceleration by a binomial series as in [126] page 391.

$$\begin{aligned}
\delta \mathbf{a} &= \delta \mathbf{a}_1 + \delta \mathbf{a}_2 && (2.11)\\
\delta \mathbf{a}_j &\approx \frac{a_{t,j}\mathbf{r}_{\mathrm{rel}}}{r_{t,j}} - \frac{3\mathbf{a}_{t,j}}{r_{t,j}}(\hat{\mathbf{a}}_{t,j} \cdot \mathbf{r}_{\mathrm{rel}}) && (2.12)\\
\delta a_{j,l} &\approx \frac{3a_{t,j}\sin\theta_j}{r_{t,j}}(\hat{\mathbf{a}}_{t,j} \cdot \mathbf{r}_{\mathrm{rel}}) = \frac{3Ra_{t,j}\sin\theta_j\cos\theta_j}{r_{t,j}}\,, && (2.13)
\end{aligned}$$

where j denotes the relevant body (1 for Sun and 2 for Earth), the subscript l denotes the lateral component of the acceleration and θ_j the angle between $\mathbf{r}_{\mathrm{rel}}$ and $\mathbf{a}_{t,j}$ or equivalently between $\mathbf{r}_{\mathrm{rel}}$ and $-\mathbf{r}_{t,j}$. We will use a, r to denote the norms $\|\mathbf{a}\|, \|\mathbf{r}\|$ respectively. In order to find configurations that induce axial differential acceleration, we find values of $\mathbf{r}_{\mathrm{rel}}$ that balance $\delta\mathbf{a}_1$ against $\delta\mathbf{a}_2$ so that their sum is in the direction of $\mathbf{r}_{\mathrm{rel}}$. This corresponds to when their lateral components δa_{1l} and δa_{2l} are equal as shown in Fig. 2.7. Since the first term in the approximate differential acceleration from each body is in the direction of $\mathbf{r}_{\mathrm{rel}}$, the problem reduces to balancing the second terms of Equation 2.12. After dividing by common terms, axial differential acceleration is equivalent to the following conditions:

$$\begin{aligned}
\delta a_{1,l} &= \delta a_{2,l} && \iff && (2.14)\\
0 &= \frac{a_{t,1}}{r_{t,1}}\cos\theta_1\sin\theta_1 - \frac{a_{t,2}}{r_{t,2}}\cos\theta_2\sin\theta_2 && \iff && (2.15)\\
0 &= \frac{a_{t,1}}{r_{t,1}}\sin 2\theta_1 - \frac{a_{t,2}}{r_{t,2}}\sin 2\theta_2\,. && && (2.16)
\end{aligned}$$

Defining $\psi = \theta_1 + \theta_2$ as the angle between the vectors from the telescope to the two bodies, such that:

$$\psi = \arccos\left(\frac{r_{t,1}^2 + r_{t,2}^2 - 1}{2r_{t,1}r_{t,2}}\right), \qquad (2.17)$$

equation 2.16 becomes:

$$0 = \frac{a_{t,1}}{r_{t,1}}\sin 2\theta_1 - \frac{a_{t,2}}{r_{t,2}}\sin(2\psi - 2\theta_1) \qquad (2.18)$$

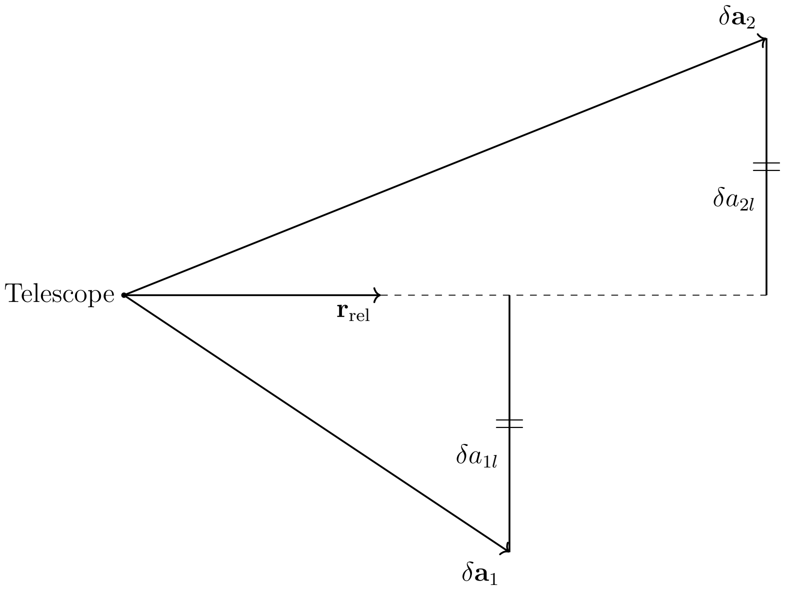

Figure 2.7: The desired orientation of the telescope to starshade vector ($\mathbf{r}_{\mathrm{rel}}$) relative to differential acceleration vectors from Sun and Earth gravity ($\delta\mathbf{a}_1, \delta\mathbf{a_2}$).

Expanding the trigonometric term in equation 2.18, we obtain

$$\theta_1 = \frac{1}{2}\arctan\left(\frac{\sin(2\psi)a_2/r_2}{a_1/r_1 + \cos(2\psi)a_2/r_2}\right) \tag{2.19}$$

dropping the subscript t for readability.

To summarize, the location of one of the poles is in the plane of the Earth, Sun, and telescope, situated between the telescope to Earth vector ($\mathbf{r_{t,2}}$) and the telescope to Sun vector ($\mathbf{r}_{t,1}$), θ_1 in angle away from the telescope to Sun vector, $\mathbf{r}_{t,1}$. One may rotate a unit vector in the direction from the telescope to the Sun, $\hat{\mathbf{r}}_{t,1}$, about the $-z_t\hat{\mathbf{j}} + y_t\hat{\mathbf{k}}$ axis by θ_1 to obtain a unit vector in the direction of the pole. Note that the results of this approach are identical to the eigenvector approach as well as numerical minimization of the approximate linear differential lateral acceleration. Given the location of a single pole that we have described, the other pole and the corresponding great circle are also known.

The great circle is of particular interest since it is a higher dimensional object than the two poles. Many more stars will be easily observable along the great circle than on or near the poles. As a result, it becomes important to quantify how low the differential lateral acceleration is along the great circle. We employ equation 2.19 to find a unit vector in the approximate direction of the pole and potentially improve on this by numerical minimization. Upon obtaining the approximate or the exact pole location, the corresponding great circle consists of all of the unit vectors orthogonal to the pole vector. We may parameterize this great circle arbitrarily with a parameter τ. Figure 2.8 presents the differential lateral acceleration along the great circles corresponding to the exact and approximate pole locations at each point along the halo orbit. Position of the telescope along the halo orbit is given along the x-axis by the time t from the initial epoch when the telescope is located at $\mathbf{r}_0$ as shown in Fig. 2.5. At each of these values of t, the position of the telescope leads to a direction for a pole given by equation 2.19, which correspond to the values in Fig. 2.6. Each time t maps to a pole location, which in turn maps to a single corresponding great circle. Position along the great circle is given on the y-axis by τ, the arbitrarily chosen phasing parameter. Note that time values near 0 and π lead to generally higher differential lateral accelerations as the two satellites are closer to the Earth at this point in the halo orbit. One can see that as the telescope moves along its halo orbit, even at its closest point to Earth, the differential lateral acceleration along the corresponding great circle is consistently one to two orders of magnitude below the highest values shown in Fig. 2.2. Using equations 2.7-2.9, with a lateral position tolerance of 1 meter, this translates to a difference between six stationkeeping maneuvers per hour in the worst case and fewer than one interruption per hour for observations along the great circle. Considering both the exact or approximate great circle effectively determines convenient choices of stars for more fuel efficient and less frequently interrupted observations.

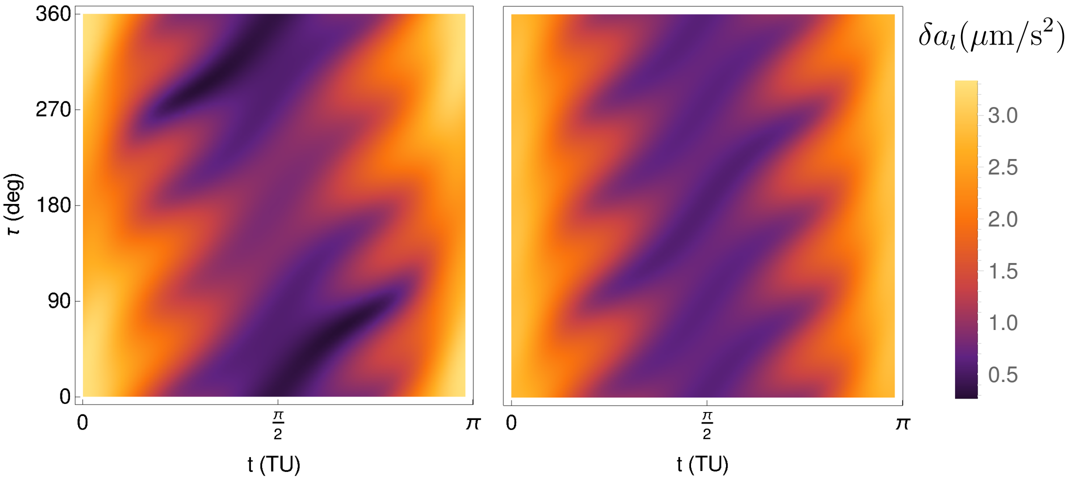

Figure 2.8: Differential lateral acceleration in μm/s^2 is depicted along the great circle for a telescope moving along the reference halo orbit. Exact (left) and approximate (right) pole positions describe the great circle.

2.4 Conclusion

We have explored trends involving station keeping metrics for observation of exoplanets with a telescope and starshade pair. Differential lateral acceleration proved to be an effective proxy for metrics such as time between interruptions for starshade orbit maintenance and delta-v. Using this metric as a proxy enables mission design software to estimate stationkeeping costs with a simple analytical calculation rather than a numerical integration as has been previously done.

Additionally, understanding of trends in stationkeeping costs has increased as a result of this analytical approach. For a fixed position of the telescope, differential lateral acceleration as a function of the line-of-sight vector from telescope to target star proved to possess minima along two poles and their corresponding great circle. We derived an analytical approximation for the location of these minima, and demonstrated that for a design reference mission, observing stars along the great circle yields magnitudes of differential lateral acceleration that are one or two orders of magnitude lower than if the target were chosen indiscriminately. We advocate cognizance of this great circle of easy to observe targets during design of exoplanet missions. By considering targets as they cross this great circle, one may potentially pare down the large design space for scheduling problems related to exoplanet imaging missions.

CHAPTER 3

SINGULARITIES IN LINEAR GUIDANCE METHODS AND ORBITAL DEBRIS PINCH POINTS

3.1 Introduction

Approaches to problems in relative satellite dynamics, control, and estimation vary in the variables used for analysis, from relative Cartesian state to any number of relative or differential orbital element sets. While simple and well-studied, linear analysis with Cartesian states still offers insights to be explored and connected at the intersection of distribution propagation, collision avoidance, uniqueness of solutions to boundary value problems, and reachable set theory.

Reachable set theory applied to reconfiguration problems has been explored by [23, 131, 129]. Pinching points at which the reachable set over time collapses to a lower dimensional manifold are described by [37, 131, 129], and attributed to singularities in the associated linear variational equations. The reduced dimension reachable set appears at a singular transfer time, and can be given in terms of the null space of a block of the state transition matrix. Through another lens, this dimension reduction can be seen as the presence of non-unique and impossible relative transfers depending on the specific boundary values. The existence of non-unique transfers warns of potential threats for collision in the deployment of subsatellites, or of secondary collisions after the creation of a debris field from a collision.

Closely related to reachable set theory, the relative Lambert problem, including its singularities, has been explored by [22, 56, 93, 130]. Transfer singularities were first explored in Cartesian state variables by [118] and later independently by [93], while [22, 130] explore the problem in relative orbital elements. [22] links these transfer singularities to the minimum time, multi-revolution Lambert solution through numerical computation, and [118] makes the connection by relating the state transition matrix and the sensitivity of transfer ellipse semimajor axis with respect to time of flight. We offer an alternative proof using the work of [119] to prove the relationship between transfer singularities in the linearized model and unique multi-revolution transfers in the Lambert problem. From here, we leverage the work of [109] to generalize this relationship to two point boundary value problems associated with arbitrary second-order differential equations with sufficient smoothness properties. This extends the result's applicability to the three body problem and beyond.

Finally, we explore the two impulse formation reconfiguration problem with variable transfer duration and initiation epoch. Using singular value decomposition, we present a description of the magnitude of the final impulse as a function of duration and the difference between the initial actual and desired relative states. The effects of transfer singularities appear in this general example, and the Δv for the final impulse of the reconfiguration is optimized as transfer time approaches the singularity.

3.2 Singular Transfers in the Clohessy-Wiltshire Equations

Consider the motion of a deputy satellite in the rotating reference frame of some chief (reference) satellite in a nearly circular orbit. The chief is assumed to be at the origin of a coordinate system associated with a non-inertial frame travelling along the chief's orbit, and the position of the deputy with respect to the chief is given in radial, in-track, and cross-track coordinates as $x\hat{r} + y\hat{s} + z\hat{w}$, where $\hat{r}$ is defined as the direction from Earth center to chief satellite, $\hat{w}$ is in the direction of specific angular momentum of the chief satellite, and $\hat{s} = \hat{w} \times \hat{r}$ completes the right-handed system. In the case of a circular reference orbit, $\hat{s}$ corresponds to the direction of the velocity vector of the reference satellite.

The Clohessy-Wiltshire equations describe relative motion of a deputy satellite in close proximity to a chief satellite in a nearly circular reference orbit [24, 93]. The equations are given in matrix form as

$$\mathbf{x} = \begin{bmatrix} x, y, z, \dot{x}, \dot{y}, \dot{z} \end{bmatrix} \tag{3.1}$$

$$\mathbf{x}_t = \Phi_0^t \mathbf{x}_0 \tag{3.2}$$

$$\Phi_0^t = \begin{bmatrix} 4-3c & 0 & 0 & s/n & 2/n-2c/n & 0 \\ -6nt+6s & 1 & 0 & -2/n+2c/n & 4s/n-3t & 0 \\ 0 & 0 & c & 0 & 0 & s/n \\ 3ns & 0 & 0 & c & 2s & 0 \\ -6n+6nc & 0 & 0 & -2s & -3+4c & 0 \\ 0 & 0 & -ns & 0 & 0 & c \end{bmatrix} \tag{3.3}$$

$$\Phi_0^t = \begin{bmatrix} \Phi_{\mathbf{rr}} & \Phi_{\mathbf{rv}} \\ \Phi_{\mathbf{vr}} & \Phi_{\mathbf{vv}} \end{bmatrix} \tag{3.4}$$

where $s = \sin(nt)$ and $c = \cos(nt)$ and n is the mean motion of the reference orbit with units consistent with the spatial units from $\mathbf{x}$ and temporal units from t. The state transition matrix Φ_0^t maps an initial Cartesian relative state to a final relative state at some time t in the future. Each block of Φ_0^t is a three by three matrix giving the sensitivity of the final state of the first variable listed (relative position or velocity), with respect to the initial state of the second variable listed.

A standard problem in the study of relative motion is calculating impulsive transfers to send a deputy satellite at an initial position $\mathbf{r}_0$ at the initial epoch to some desired position $\mathbf{r}_t$ at the final epoch t. When the inverse of $\Phi_{\mathbf{rv}}$ exists, the unique initial velocity to achieve the given transfer is given as:

$$\mathbf{v}_0 = \Phi_{\mathbf{rv}}^{-1}(\mathbf{r}_t - \Phi_{\mathbf{rr}}\mathbf{r}_0) \tag{3.5}$$

More interesting is the case when $\Phi_{\mathbf{rv}}$ is singular. Clearly, this can occur when the third column of $\Phi_{\mathbf{rv}}$ is all zeros, which corresponds to $s/n = 0$ meaning that nt is a multiple of π. Geometrically, this refers to the fact that a half or full period from an impulsive plane change maneuver, the satellite will be along the intersection of the new plane and the old plane, regardless of the plane change magnitude. An impulse cannot change the cross-track location of a deputy satellite at multiples of half a reference period from the impulse. Since the cross-track dynamics are uncoupled from the in-plane dynamics, we move on to just examining the in-plane component of the transfer problem, and singularities arising therein.

Let $\tau = nt$ and

$$\Theta_0^\tau = \frac{1}{n}\begin{bmatrix} \sin\tau & 2 - 2\cos\tau \\ -2 + 2\cos\tau & 4\sin\tau - 3\tau \end{bmatrix} \tag{3.6}$$

We see that when τ is a multiple of 2π, Θ_0^τ has only -3τ in the last entry, and zeros everywhere else. So, $\Theta_0^{2\pi k}$ is a singular matrix for integer k. This indicates that only the in-track location of the deputy changes at exactly one reference period later, regardless of the initial velocity of the deputy.

Further, the determinant of Θ_0^τ is zero when τ satisfies the transcendental equation

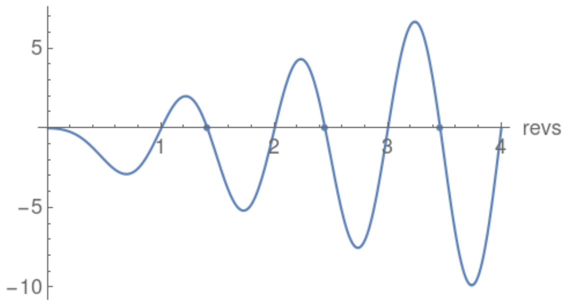

Figure 3.1: A plot showing the zeros of the determinant of Θ_0^τ.

$$\frac{3}{8}\tau \sin \tau + \cos \tau - 1 = 0 \tag{3.7}$$

We plot the determinant of Θ_0^τ in Fig. 3.1. The first three nontrivial roots (not multiples of 2π) occur at approximately 1.4067, 2.4453, and 3.4612 periods.

The eigenvectors of Θ_0^τ give the active and inactive spaces of the initial velocity for a deputy satellite in this system. Table 3.1 shows that the inactive space is radial for full reference periods, and nearly radial otherwise. At these singular transfers times, any trajectory that began at the origin at time zero, will have in-plane component orthogonal to the inactive space regardless of initial velocity.

Figure 3.2 shows the evolution of a swarm of trajectories which all begin at the origin with random initial velocities inside the unit square in the non-dimensional form of the problem. The swarm is displayed at .5, 1, 1.25, and approximately 1.4067 reference periods. At time 0, the swarm begins on a 2-dimensional manifold in the $x, y, \dot{x}, \dot{y}$ radial, in-track phase space. At .5 and 1.25 reference periods, we see the general case in which the swarm occupies a 2 dimensional manifold when projected into x, y space. Finally, at 1 reference period, and 1.4067 reference periods, the swarm collapses to occupy only a 1-dimensional manifold in x, y space. This corresponds to the notion of a pinch point as outlined in [37].

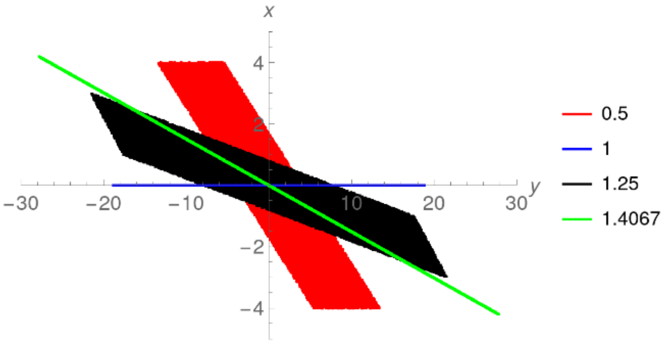

Figure 3.2: Four snapshots of a cloud of particles which begin at the origin at the initial epoch, and evolve to occupy a one or two-dimensional manifold in their in-plane projection. The legend gives the number of reference revolutions from the initial epoch for the given snapshot. Equation 3.6 is used for propagation with $n = 1$. A different choice of n or units scale results.

This implies that the boundary value problem associated with relative motion transfers at these singular time values does not have unique solutions. Boundary value problems where the end point is not along the active eigenspace will not have any solution, while an endpoint orthogonal to the image of the inactive space gives rise to infinitely many solutions.

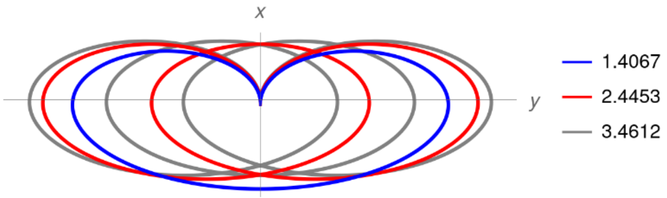

Figure 3.3: Null transfer trajectories, which begin and end at the origin after the given number of reference periods.

Figure 3.3 shows null transfers for the first three nontrivial singular transfer times (the roots of equation 3.7 shown in Fig. 3.1). These are trajectories which begin at the origin and end at the origin, but are not the fixed point solution at the origin. The initial velocity is in the direction of the eigenvector corresponding to zero. Multiplying this initial velocity by a constant gives rise to infinitely many scaled versions of the same null transfer.

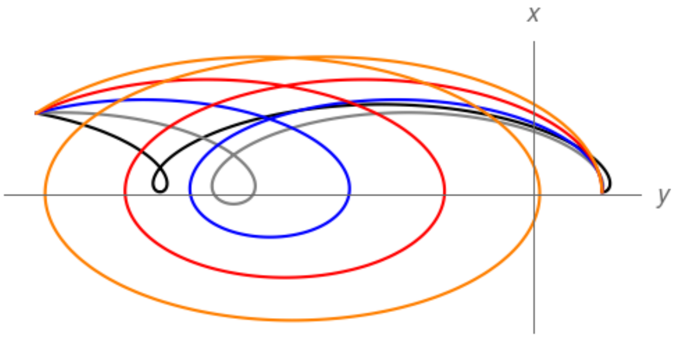

Figure 3.4: Five of the infinitely many trajectories which begin and end at a common location around 1.4067 reference periods later with differing initial velocity in the linear model of relative motion.

Figure 3.4 shows the non-uniqueness of a more arbitrary transfer with transfer time corresponding to the first nontrivial root. Each of these transfers shares the same active initial velocity component, but varies in the orthogonal component whose corresponding eigenvalue is zero.

The singularities we have presented arising from boundary value problems in the Clohessy-Wiltshire equations suggest a number of interpretations. From a probabilistic standpoint, they imply that there are times where initial certainty in position implies some level of certainty of position in the future regardless of uncertainty in initial velocity. That is, under the action of the Perron-Frobenius operator [40] associated with the Clohessy-Wiltshire equations, the support of a distribution projected into a subspace of the phase space changes dimensions at times when blocks of the state transition matrix are singular. This phenomena invites exploration in other linear systems, as well as its approximate effects in non-linear systems.

From a practical standpoint, there are two other important implications of this exploration of singularities. The first implication is in explaining trends in the cost and feasibility of relative transfers that we will explore in section 3.6. The second implication is in understanding situations in which multiple objects leave a single satellite at the same time. Example situations include modeling a collision or other breakup of a satellite, as well as the deployment of multiple objects from one single vehicle. In the case of debris modeling when a collision time is well known, these singular transfer times may give important opportunities to image and catalog debris, when it is known that objects will all approximately lie in a lower dimensional manifold and be less likely to obscure one another. These times are also likely candidates for observing secondary collisions given the non-uniqueness of the transfer problem. On the other hand, this analysis can be used in planning the deployment of satellites from a single vehicle. Satellites deployed with the same active component of initial velocity at the same time will collide under the Clohessy-Wiltshire equation model of relative dynamics at the singular transfer time corresponding to that active component of initial velocity. Thus, the null space of Θ_0^τ becomes important to avoid deployments that could cause collisions at singular transfer times. The unit vectors in the nullspace of Θ_0^τ for the first three nontrivial singularity times are given in table 3.1. Objects deployed with differences in initial velocity in the direction of vectors from this table are at risk of colliding at the relevant singular transfer time.

Table 3.1: The inactive components of initial velocity corresponding to singular transfer times.

$\tau/2\pi$	$\dot{x}$	$\dot{y}$
1	1	0
1.4067	0.9888	-0.1492
2.4453	0.9962	-0.0865
3.4612	0.9981	-0.0612

These inactive velocity vectors are in the direction of $(3\tau, -4)$. This inactive component results in the final relative position coming to some multiple of $(4, -3\tau)$, perpendicular to $(3\tau, 4)$ as identified by [37] where the ordering of the in-track and radial coordinates in reversed in their notation.

3.3 Singular Transfers in the Tschauner-Hempel Equations

Following much the same procedure as the previous section, we may examine the same block of the Yamanaka-Ankersen state transition matrix [29, 123, 136] solution to the Tschauner-Hempel equations. In doing so, we see that transfer singularity times become dependent on reference eccentricity, and the initial chief true anomaly. Figure 3.5 gives combinations of initial true anomaly θ_0 and change in mean anomaly ΔM or change in true anomaly $\Delta\theta$ of the reference orbit that yield transfer singularities for various values of the reference eccentricity. In the right pane, the change in chief true anomaly serves as a proxy for the transfer time, while in the left pane, change in reference mean anomaly is directly proportional to the transfer time. While the zero reference eccentricity case agrees with our previous results, we see that for other reference eccentricities the singular transfer times are no longer independent of initial reference true anomaly. Further, the singular transfer time varies very quickly when the initial chief anomaly is near apogee. A wide variety of transfer times (proportional to ΔM) are singular, and so there is not one single time that a mission designer may avoid.

3.4 Relation to Unique Solutions of the Multi-Revolution Lambert Problem

An important question is how well the infinitely non-unique linear behavior outlined above imitates the actual nonlinear behavior of satellite relative motion in

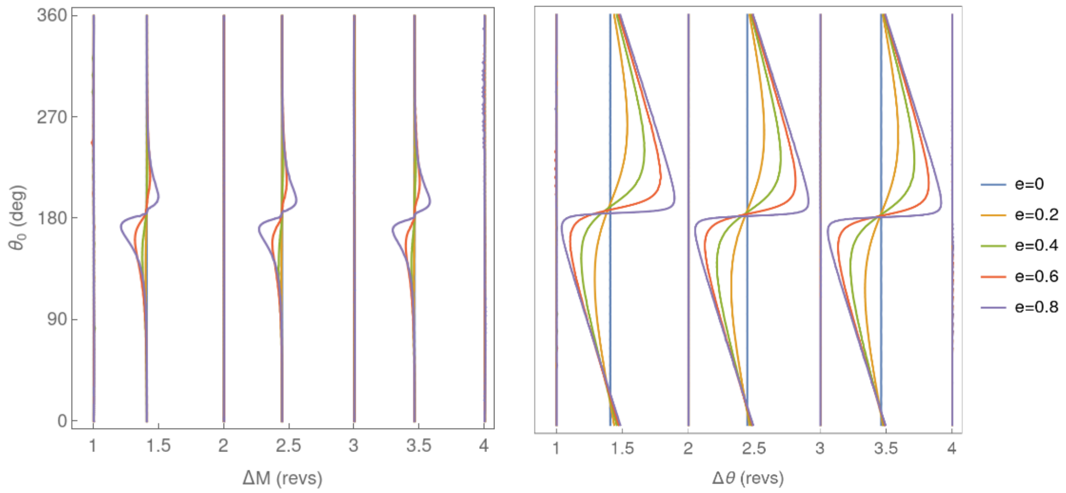

Figure 3.5: Singular relative transfers of various reference orbit eccentricities and initial reference true anomaly. The transfer time is measured in revolutions of reference mean anomaly on the left (periods), and revolutions of reference true anomaly on the right.

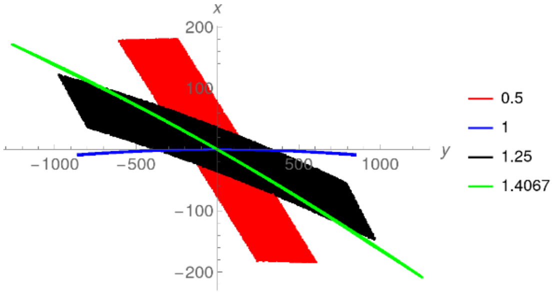

Figure 3.6: The same swarm as Fig. 3.2, but specifically about a geosynchronous reference orbit, with propagation performed using the full two-body dynamics. The labeled times are still in periods of the geosynchronous orbit and units are in kilometers.

the two-body problem. Figure 3.6 presents a replication of Fig. 3.2 in the two-body dynamic model without linearization. The dimension reduction of the swarm seems to approximately carry over to the two-body model with curvature of the nearly one-dimensional manifold as the only immediately discernible difference.

Regardless of Fig. 3.6 and its similarity to 3.2, we know that there are qualitative differences in the number of solutions to the boundary value problems from the approximate linear and full nonlinear models. While we have established the existence of zero or infinitely many solutions to the boundary value problem in the approximate system, it is well-known that multi-revolution Lambert problems have either zero, one, or two prograde solutions [3, 119].

Thus, the approximately one-dimensional manifold in Fig. 3.6 cannot be one-dimensional since the flow map of the two-body dynamics is continuous in the state vector and the inverse of a point in the codomain has at most two values. If there were a function from a two-dimensional manifold to a one-dimensional manifold that had this property, removing two points from the domain ($\mathbb{R}^2$) would result in the function taking a connected set to a disconnected set (the one-dimensional manifold missing a point). No continuous function can do this, and so the image of the full two-body flow map at a singular transfer time is not actually one-dimensional as it appears to be and is in the linearized dynamics case.

While the general case is the existence of two prograde solutions, we will show that the singularities in the transfers of the linearized relative motion equations correspond to the unique minimum time multi-revolution transfers in the Lambert problem: trajectories which represent a sort of bifurcation point in the Lambert problem. We offer here a proof for the circular case.

Following [119], define the nondimensional variables X, Y:

$$X^2 = 1 - \frac{r_1 + r_2 + |\mathbf{r}_2 - \mathbf{r}_1|}{4a} \tag{3.8}$$

$$Y^2 = 1 - \frac{r_1 + r_2 - |\mathbf{r}_2 - \mathbf{r}_1|}{4a} \tag{3.9}$$

where $\mathbf{r}_1$ and $\mathbf{r}_2$ are the initial and terminal points of the Lambert transfer with respect to the central body, and a is the semi-major axis associated with the transfer between the two points. We now turn our attention to determining the number of solutions to the Lambert problem when the solution is constrained to revolve around the central body at least n times. Sun [119] gives the necessary conditions for the solution of the multi-revolution Lambert problem to be unique:

$$\frac{1}{3}\left(\frac{(2+X^2)\sqrt{1-X^2}}{X}-\frac{(2+Y^2)\sqrt{1-Y^2}}{Y}\right)-\left(\cot^{-1}\left(\frac{X}{\sqrt{1-X^2}}\right)-\cot^{-1}\left(\frac{Y}{\sqrt{1-Y^2}}\right)\right)=n\pi \tag{3.10}$$

If a trajectory satisfies equation 3.10 (equation 12 from [119]), then it is the unique minimum time n-revolution Lambert transfer between the initial and terminal points $\mathbf{r}_1, \mathbf{r}_2$. Given the duration between these two points t^*, there are no n-revolution transfers between the initial and terminal points in less than t^* time, there is only the single n-revolution transfer in the given time t^*, and higher transfer times t^* give rise to two n-revolution transfers. When transfer time t is viewed as a bifurcation parameter, the trajectory satisfying equation 3.10 is a bifurcation point among the trajectories which solve the Lambert problem between two given points.

To assess trajectories arising from circular orbits to see if they are minimum time multi-revolution Lambert transfers, we let $r_1 = r = r_2 = a$, and let $\psi \in [0, \pi]$ be the angle between the two vectors. From the law of cosines we obtain

$$|\mathbf{r}_2 - \mathbf{r}_1| = r\sqrt{2(1-\cos\psi)} = 2\sin(\psi/2) \tag{3.11}$$

$$X^2 = \frac{1}{2}(1-\sin(\psi/2)) = \sin^2\left(\frac{\psi+\pi}{4}\right) \tag{3.12}$$

$$Y^2 = \frac{1}{2}(1+\sin(\psi/2)) = \cos^2\left(\frac{\psi+\pi}{4}\right) \tag{3.13}$$

Defining an intermediate variable $\xi = \frac{\psi+\pi}{4}$, and choosing X as positive in the region of interest to give rise to the low transfers Sun predicts in the minimum time case [119], we have

$$X = \sin \xi \tag{3.14}$$

$$Y = \pm \cos \xi \tag{3.15}$$

Substituting this into equation 3.10, we obtain

$$\pm\frac{1}{3}\left((2+\sin^2(\xi))\cot(\xi) - (2+\cos^2(\xi))\tan(\xi)\right) \mp \left(\cot^{-1}(\tan\xi) - \cot^{-1}(\cot\xi)\right) = n\pi \implies \tag{3.16}$$

$$\pm\frac{2}{3}(\cot\xi - \tan\xi) \pm \psi/2 = n\pi \implies \tag{3.17}$$

$$\pm\frac{4}{3}(\cot\psi - \csc\psi) \pm \psi/2 = n\pi \implies \tag{3.18}$$

$$\frac{3}{8}(\psi \mp 2n\pi)\sin\psi + \cos\psi - 1 = 0 \tag{3.19}$$

Note, the inverse cotangent identity used above is valid for ψ in our given range, and stems from the inverse cotangents being symmetric about $\pi/4$. Thus, their difference is twice the difference of ξ and $\pi/4$, or simply $\psi/2$.

Thus, given $\tau = \psi + 2n\pi$, solutions to equation 3.7 are also solutions to equation 3.19, and so the combinations of reference trajectories and transfer times at which the Clohessy-Wiltshire singularities appear are also unique minimum time transfers in the two-body dynamics. This means that the infinitely many null transfers of the Clohessy-Wiltshire equations are not representative of the nonlinear dynamics.

One may determine whether a trajectory is a minimum time transfer between two points by checking that Equation 11 from [119] is satisfied for the given trajectory. In this manner, we produced plots identical to Fig. 3.5 which are not presented here to avoid redundancy, suggesting that reference trajectories for which the upper right block of the Yamanaka-Ankersen state transition matrix is singular are also minimum time Lambert transfers among elliptical orbits.

Another more elegant proof of the correspondence of singularity in the upper right block of the inertial state transition matrix and the minimum time solution of the multi-revolution Lambert problem appears in [118] where the relationship between semimajor axis of the transfer ellipse and the transfer time is leveraged. This proof is general in its application to elliptical orbits. We keep our proof of the circular orbit case above as it ties back to [119] and offers a different perspective. In the next section, we present a proof that is even more general than [118] in that it applies not only to elliptical orbits in the two-body problem but also to systems beyond the two-body problem. We go on to relate the singularity of the upper right block of the rotating frame Yamanaka-Ankersen state transition matrix with the inertial state transition matrix, tying together existing literature from [118, 119] and our own work.

3.5 Generalized Bifurcation in Number of Solutions

This relationship between the state transition matrix and bifurcation in number of solutions to a boundary value problem is not unique to two-body motion, the associated Lambert problem, and the Yamanaka-Ankersen state transition matrix. There are other dynamical systems for which singularity of the upper right block of the state transition matrix solution to the first-order variational equations indicates a bifurcation in the number of solutions to a two point boundary value problem with the value of the independent variable at the second boundary as the bifurcation parameter.

Following [109], we may generalize to arbitrary k-dimensional second-order ordinary differential equations for which the right hand side $\mathbf{f}(\mathbf{x}, t)$ is twice differentiable with all continuous second partial derivatives. This is a notable specific case of the general problem discussed in [109] since this may be represented as $2k$-dimensional first-order system with continuous first-order partial derivatives.

In order to bring the bifurcation parameter into the dynamics rather than the boundaries, the boundary value problem

$$\ddot{\mathbf{r}} = \mathbf{f}(\mathbf{r}, t) \tag{3.20}$$

$$\mathbf{r}(0) = \mathbf{r}_0 \tag{3.21}$$

$$\mathbf{r}(t_f) = \mathbf{r}_f \tag{3.22}$$

may be reframed by a time change as

$$\mathbf{r}'' = t_f \mathbf{f}(\mathbf{r}, \tau) \tag{3.23}$$

$$\mathbf{r}(0) = \mathbf{r}_0 \tag{3.24}$$

$$\mathbf{r}(1) = \mathbf{r}_f \tag{3.25}$$

where $'$ denotes the derivative with respect to τ.

Consider the corresponding $2k$ dimension first-order system, $\mathbf{x}' = F$, as well as $\Phi(\tau)$, the state transition matrix solution to the first-order variational equations associated with these dynamics

$$\Phi' = \frac{\partial \mathbf{F}}{\partial \mathbf{x}}\Phi, \Phi(0) = I_{2k} \tag{3.26}$$

$$\mathbf{x} = \begin{bmatrix} \mathbf{r} \\ \mathbf{v} \end{bmatrix}, \mathbf{F} = \begin{bmatrix} \mathbf{v} \\ \mathbf{f} \end{bmatrix} \tag{3.27}$$

and the boundary conditions represented as

$$0 = \mathbf{g}(\mathbf{x}(0), \mathbf{x}(1)) = \begin{bmatrix} \mathbf{r}(0) - \mathbf{r}_0 \\ \mathbf{r}(1) - \mathbf{r}_f \end{bmatrix} \tag{3.28}$$

Then, [109] tells us that a sufficient condition for a branch point is that a trajectory solves the boundary value problem, and in addition,

$$\det\left(\frac{\partial \mathbf{g}}{\partial \mathbf{x}(0)} + \frac{\partial \mathbf{g}}{\partial \mathbf{x}(1)}\Phi(1)\right) = 0 \implies \tag{3.29}$$

$$\det\left(\begin{bmatrix} I_k & 0 \\ 0 & 0 \end{bmatrix} + \begin{bmatrix} 0 & 0 \\ I_k & 0 \end{bmatrix}\Phi(1)\right) = 0 \implies \tag{3.30}$$

$$\det\left(\begin{bmatrix} I_k & 0 \\ \Phi_{rr}(1) & \Phi_{rv}(1) \end{bmatrix}\right) = 0 \implies \tag{3.31}$$

$$\det(\Phi_{rv}(1)) = 0 \tag{3.32}$$

here I_k is the k-dimensional identity matrix.

To conclude, for a sufficiently smooth vector field corresponding to a second-order ordinary differential equation and a two point boundary value problem with boundary conditions only on the state variable (and not its derivative), we have found a test function for branch/bifurcation points in the number of solutions. When the upper right block of the state transition matrix to the associated first-order variational equations about the trajectory, $\det(\Phi_{rv})$, is zero, a change in the number of solutions to the boundary value problem occurs when the bifurcation parameter is varied around the value at the branch point.

We specifically were interested in the value of the independent variable at the second boundary as the bifurcation parameter, but note that this assumption was never used in proving the sufficiency of $\det(\Phi_{rv}) = 0$ to indicate the trajectory is a branch point. The bifurcation parameter may be a more general part of the dynamics or boundaries and this result will still apply.

We now apply this general result to prove that when the upper right block of the Yamanaka-Ankersen or Clohessy-Wiltshire state transition matrix is singular, the reference trajectory is a minimum time multi-revolution Lambert solution (a branch point of the bifurcation problem depending on transfer time as a bifurcation parameter).

Since the Yamanaka-Ankersen and Clohessy-Wiltshire state transition matrices are given in a rotating coordinate system, the determinant of the upper right block of the state transition matrix is invariant under a change of coordinates from an inertial frame to the rotating RSW frame. The upper right block of the rotating frame STM Φ'_{rv} in terms of the inertial frame STM Φ_{rv} is

$$\Phi'_{rv} = T_f^{-1} \Phi_{rv} T_0 \tag{3.33}$$

where T is the rotation transformation of position vectors from the inertial to the rotating frame at the given epoch (final or initial). Since T is given by an orthogonal matrix, the determinants of the two STMs will be equal. Note that preservation of the determinant does not necessarily hold for the other three blocks from the STM. The change of coordinates yields products with skew symmetric matrices from the velocity coordinate change in each of these [28].

Thus, the general theory of branch points in bifurcation problems for two point boundary value problems applies to the specific problems we have encountered here.

3.6 Two Impulse Formation Reconfiguration

We turn our attention to an application problem. Rather than attempting to target a specific final relative position at a specific final time, it is of common interest to attain or maintain some relative orbit. This is often specified in terms of differential orbital element [27, 45, 72, 105] or relative orbital element set [86]. However, we may equivalently consider the full Cartesian desired state of the deputy at some reference epoch, as this will uniquely correspond to any of the relative or differential orbital element sets. We employ the epoch of the initial impulse as our reference. This is to say, we will be looking for a two impulse reconfiguration $(\Delta\mathbf{v}_0, \Delta\mathbf{v}_f)$ of a deputy satellite beginning at $\mathbf{x}_0$ which will arrive at a final relative state $\mathbf{x}_f$ that also evolves from the "desired" initial state $\mathbf{x}_0 + \delta\mathbf{x}_0$ without control. We study the problem of determining $\Delta\mathbf{v}_f$ in the following equation:

$$\Theta\left(\mathbf{x}_0 + \begin{bmatrix}\mathbf{0} & \Delta\mathbf{v}_0\end{bmatrix}^T\right) + \begin{bmatrix}\mathbf{0} & \Delta\mathbf{v}_f\end{bmatrix}^T = \mathbf{x}_f = \Theta(\mathbf{x}_0 + \delta\mathbf{x}_0) \tag{3.34}$$

In the reconfiguration problem, the terminal Δv can be characterized solely by the transfer time and the difference in initial position of the actual and desired states. In contrast, the initial Δv depends on the relative initial velocities at the initial time. We consider here only the terminal impulse and demonstrate the appearance of transfer singularities in the analysis of its magnitude. The initial relative position will affect the final velocity as mapped through Θ_{vr}, and the relative velocity after the initial impulse (conveniently given by $\Theta_{rv}^{-1}\Theta_{rr}\delta\mathbf{r}_0$) will affect the final velocity as mapped through Θ_{vv}. Thus, the final impulse can be given as

$$\mathbf{\Delta v}_f = (\Theta_{vr} + \Theta_{vv}\Theta_{rv}^{-1}\Theta_{rr})\delta\mathbf{r}_0 \tag{3.35}$$

with the singular value decomposition of the mapping given by

$$(\Theta_{vr} + \Theta_{vv}\Theta_{rv}^{-1}\Theta_{rr}) = U\Sigma V^T \tag{3.36}$$

Figure 3.7 shows the singular values σ_i associated with the mapping in equation 3.35. The two singular values differ greatly in magnitude, and avoiding singular transfer times is important in keeping the final impulse value low. Initial relative positions that are multiples of the right singular vector $\mathbf{v}_2$ corresponding to the lower singular value, σ_2, are generally very close to exclusively in-track. To characterize the direction of $\mathbf{v}_2$, we define the quantity β, the angle of $\mathbf{v}_2$ from the radial axis, oriented such that β is 90 degrees at the positive in-track axis. We plot β as a function of τ in Fig. 3.7. It is only at the singular transfer times that the orientation changes and moves to the nullspace vectors from table 3.1. Generally, the direction of the relative position vector at the first impulse is key in determining the cost of the final impulse. Unless the transfer time is one for which Θ_{rv} is singular, low cost final impulses are associated with in-track only initial position differences. If achieving this is impossible without a high initial impulse, then choosing transfer times which minimize σ_1 becomes important. Numerical minimization demonstrates these transfer times are always approximately 0.062 reference periods away from a whole period.

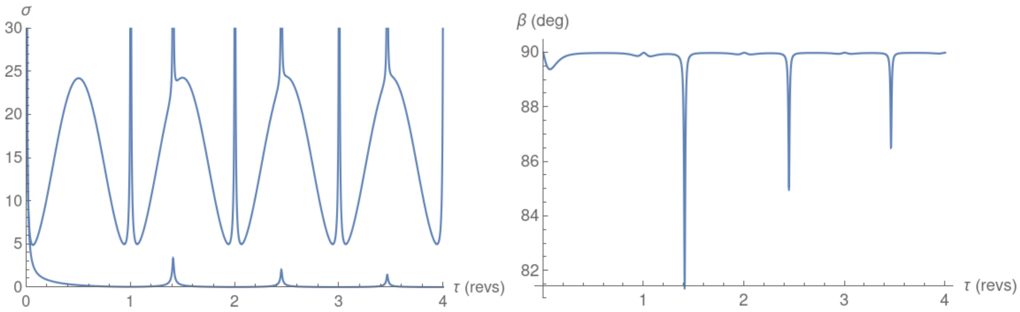

Figure 3.7: On the left, the singular values of the mapping in equation 3.35 for various transfer times. On the right, the angle from the radial axis of the vector v_2.

3.7 Conclusion

We have explored the probabilistic and debris/collision based interpretations of the singularities in the relative motion transfer problem, finding a reduction in dimension of the support of a probability distribution or swarm of satellites at singular times. This may have consequences in space situational awareness after a collision as well as planning for the safe release of sub satellites from a single original vehicle. Plots depicting singularities of transfers associated with elliptical reference orbits warned mission designers of the possibility of encountering transfer singularities for a wide variety of transfer times depending highly on the reference true anomaly at the start of the transfer. When performing optimization of transfers, calculation of the location of these singularities can be used to avoid infeasible transfers a priori. Next, we demonstrated the correspondence between infinite non-uniqueness and uniqueness of transfers in the linear dynamics and nonlinear dynamics respectively. This is mainly of theoretical interest, but may yield an alternative method of calculating how many multi-revolution Lambert solutions to expect in certain cases. We framed the connection between the Clohessy-Wiltshire equations and the multi-revolution Lambert problem in terms of general theory on the singularity of the upper right block of a state transition matrix with branch points in the number of solutions to a two point boundary value problem associated with a system of second-order ordinary differential equations. In doing so, we expanded the general theory of bifurcations in boundary value problems by simplifying a general result when applied to boundary value problems coming from second-order differential equations. Finally, singularities in the upper right block of the Clohessy-Wiltshire state transition matrix appeared in a singular value decomposition approach to analyzing the magnitude of the final Δv in a two impulse reconfiguration problem. We showed two important heuristics for transfer duration and transfer initiation in determining transfers which are optimal in the final Δv. Future work lies in exploring the possibility that these heuristics can make for a simple and effective strategy to achieve nearly optimal two impulse reconfiguration in the total Δv. It is also possible that this work may offer inspiration in developing new methods to quickly find the minimum time Lambert transfer.

CHAPTER 4

FAST COMPUTATION OF LOCAL ENERGY OPTIMAL CONTROL

4.1 Introduction

With this chapter, we begin our study of higher-order approximations of the flow of a dynamical system, and their use for optimal control purposes. Here, the use of higher-order approximations is motivated to increase accuracy of a local model of dynamics and optimal control as well as to represent energy, which is an inherently quadratic quantity.

Trajectory and mission design problems often require bilevel optimizations to determine optimal trajectories that balance mission goals with operational constraints. For example, Refs. [70, 116] deal with doubly bilevel optimizations of formation flight behavior to determine the optimal observation schedule that maximizes science yield while minimizing control costs for coordinated flight of a telescope and starshade in Sun-Earth space. In order to meet these objectives, a traveling salesman type problem is posed to determine which stars to observe and on what schedule. A proposed itinerary is judged partially on the basis of the fuel costs to maneuver the starshade accordingly. The fuel cost for one leg of the journey may be assessed by solving a continuous-thrust, optimal control problem. Thus, computation of multiple continuous-thrust optimal control problems is just one step in evaluating the objective function for one proposed itinerary when considering the overall scheduling problem. Efficient algorithms to solve continuous-thrust, optimal relative control problems in the context of three-body dynamics are necessary to facilitate solutions of this variety of bilevel optimization problems. In particular, this work will primarily focus not only on computing the optimal control, but on quickly approximating the fuel cost of that optimal control.

The continuous-thrust optimal control of one satellite relative to another has been extensively studied in the context of the two body problem [35, 19, 20, 17, 18, 21, 78]. These methods generally rely on the analytical form of the state transition matrix solutions to the Clohessy-Wiltshire or Tschauner-Hempel equations, which are not available in the context of the three-body problem. On the other hand, relative impulsive control of formations in the three-body problem has also been well studied [36, 52, 53, 99] with some recent advances in continuous optimal control. Franzini et al. [39] examined continuous-thrust control applied to relative motion in the elliptical three-body problem using an adjoint method. While this methodology improves fidelity and speed of computation, numerical integration is still required each time a new optimal control problem is posed and may be unsuitable for applications in which high computational speed of this subproblem is required to render some overarching problem tractable. Park et al. [94] presented a method using generating functions to solve optimal continuous-thrust rendezvous problems, which generalizes well for use in the three-body problem where no analytical form of the state transition matrix is known. While this approach allows for solution of the problem with arbitrary boundary conditions after a single computation of the generating function, the generating function must be recomputed from scratch whenever the time of flight or initial epoch of the problem is adjusted. Similarly, Boone et al. [11] achieved solutions of low thrust problems by differential dynamic programming with state transition tensors to obtain feedback control laws for arbitrary motion near a reference orbit and over a specified time of flight. Their more recent work on impulsive maneuvers has allowed for this method to be extended to not just calculate for a single time of flight, but a neighborhood of time of flight using one of two methods that store temporal derivatives or use

Taylor approximations in time [12, 13]. However, these methods still do not work for arbitrary initial epoch and arbitrary time of flight outside of some small region.

We aim to approximately solve continuous-thrust optimal relative control problems with arbitrary initial epoch, time of flight, and boundary conditions without performing numerical integration online. We also seek to limit storage requirements from precomputed data, and to obtain fitness metrics related to fuel use without numerical integration. In order to accomplish these goals, we begin by reviewing the properties of the first and second-order variational equations. From there, we will formulate a basic optimal control problem. Finally, we outline an algorithm to precompute and interpolate variational data associated with a reference trajectory in the dynamical system of states and costates. Our interpolation scheme is specially motivated by power series solutions of differential equations and employs a variable order for each entry of the state transition tensor being interpolated. The interpolated linear variational data yields initial costates which approximately solve the optimal control problem after only a few matrix products and the solution of a linear system twice the size of the initial state space. The second-order variational data then allows for approximation of metrics related to fuel use with another product involving the state transition tensor. Additionally, the second-order variational data may be used in a Newton iteration scheme to find more accurate solutions of the optimal control problem than would be available with just the linear variational information. Examples of motion around a reference Halo orbit are used to evaluate the approximation error for these approaches in a rendezvous setting.

A similar approach to precomputation and interpolation was taken by the authors in a previous work considering only impulsive maneuvers applied to the relative motion dynamics of a space-telescope working in conjunction with a starshade [75]. Another recent approach to interpolating state transition tensors uses regularization methods to distribute interpolation points effectively and then Chebyshev polynomials to perform the interpolation [31]. This Chebyshev interpolation approach was used to propose a relative motion model for the Gateway mission, but not employed in the context of calculating continuous-thrust maneuvers. Much of the work in the present paper could be performed within the Chebyshev interpolation framework; however, we explore interpolation leveraging cocycle conditions and the form of series solutions to variational equations. The resulting interpolation scheme is designed to work quickly and with low memory requirements when generating coarse approximations of the cost to perform optimal control. We would like to emphasize before deriving our approximation procedure that this work is intended primarily for analysis and itinerary development on the ground and not tailored for performing control onboard a satellite.

4.2 Interpolating Short Time State Transition Tensors

We examine the problem of approximating $\mathbf{\Phi}(\alpha t, 0)$ with $\alpha \in [0, 1]$ given knowledge of $\mathbf{\Phi}(t, 0)$. The most straightforward way to approach this is entrywise linear interpolation between the state transition matrix over zero time, $\mathbf{\Phi}(0, 0)$ (the identity matrix), and the original state transition matrix being interpolated from, $\mathbf{\Phi}(t, 0)$.

$$\mathbf{\Phi}^i_j(\alpha t, 0) \approx I_n + \alpha(\mathbf{\Phi}^i_j(t, 0) - I_n) \tag{4.1}$$

Error from the approximation in Eq. 4.1 will be quadratic in the time span t. Here, we present a method for interpolating state transition tensors with the same number of operations as entrywise linear interpolation, but with greater accuracy.

This method exploits the structure of state transition tensors and the underlying variational equations that produce them. We may approximate the first-order variational equations over small spans of time by assuming that the Jacobian of the dynamics stays approximately constant along the reference trajectory

$$\frac{d\mathbf{\Phi}(t,0)}{dt} \approx \frac{\partial \mathbf{F}(\mathbf{x}_0)}{\partial \mathbf{x}}\mathbf{\Phi}(t,0), \quad \mathbf{\Phi}(0,0) = I_n \tag{4.2}$$

The solution to this related equation is given by the matrix exponential

$$\mathbf{\Phi}(t,0) \approx e^{\mathbf{A}t} = \sum_{k=0}^{\infty} \frac{t^k}{k!}\mathbf{A}^k \tag{4.3}$$

where we define $\mathbf{A} = \dfrac{\partial \mathbf{F}(\mathbf{x_0})}{\partial \mathbf{x}}$ and $\mathbf{A}^0 = I_n$ for convenience. Here, $\mathbf{A}^k$ denotes the kth power of the matrix $\mathbf{A}$. The STM along a subinterval is approximated by

$$\mathbf{\Phi}(\alpha t,0) \approx e^{\mathbf{A}\alpha t} = \sum_{k=0}^{\infty} \frac{(\alpha t)^k}{k!}\mathbf{A}^k \tag{4.4}$$

In components, as for small t

$$\mathbf{\Phi}^i_j(\alpha t,0) \approx I_n + \alpha^{P^i_j}(\mathbf{\Phi}^i_j(t,0) - I_n) \tag{4.5}$$

where

$$P^i_j = \min\{p \in \mathbb{N} \quad | \quad (\mathbf{A}^p)^i_j \neq 0\} \tag{4.6}$$

That is, the terms of the STM along the subinterval are the original terms multiplied by powers of α where the power of α is determined by the first nonzero power of $\mathbf{A}$ for which the given term in the matrix is nonzero. For example, energy optimal control in the circular restricted three-body problem as described later by Eqs. 4.17 and 1.2 has a Jacobian that consists mostly of zeros. As the Jacobian is multiplied with itself repeatedly, fewer and fewer terms remain zero. Figure 4.1 depicts the matrix P for energy optimal control in the circular restricted three-body problem with generic initial conditions in the states and zero initial conditions in the costates (corresponding to a reference trajectory undergoing natural motion).

White regions in the graphical representation of P are those for which the matrix exponential has zero values and the values of P are undefined and unnecessary.

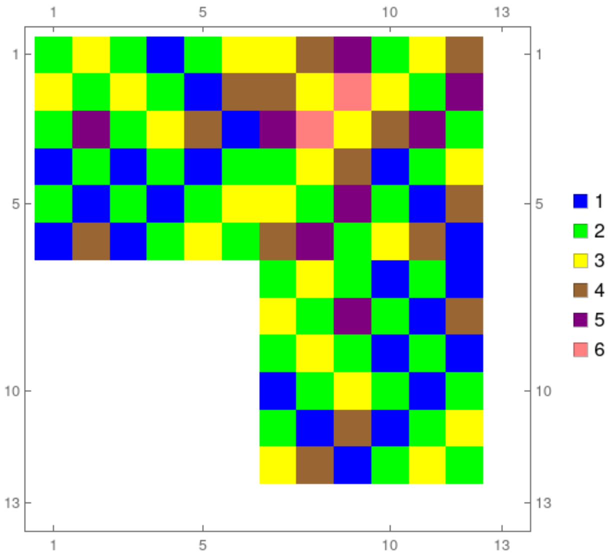

Figure 4.1: The matrix P represents the lowest power of the Jacobian $\mathbf{A}$ where the corresponding entry is non-zero.

Next, we consider $\mathbf{\Psi}(t, 0)$ and $\mathbf{\Psi}(\alpha t, 0)$. The solution to Eq. 1.15 can be written in power series in terms of unknown coefficient tensors B_N as

$$\mathbf{\Psi}^i_{j,k}(t, 0) = \sum_{N=0}^{\infty} \frac{t^N}{N!} (B_N)^i_{j,k} \tag{4.7}$$

For small t

$$\mathbf{\Psi}^i_{j,k}(\alpha t, 0) \approx \alpha^{Q^i_{j,k}} \mathbf{\Psi}^i_{j,k}(t, 0) \tag{4.8}$$

where

$$Q^i_{j,k} = \min\{p \in \mathbb{N} \quad | \quad (B_p)^i_{j,k} \neq 0\} \tag{4.9}$$

One could solve for the power series solution of $\mathbf{\Psi}$ and determine the unknown coefficient tensors B_N; however, the simplest method to obtain the tensor $Q^i_{j,k}$ is by numerically integrating $\mathbf{\Psi}$ for some short t and also $t/2$ and rounding the logarithm of their quotient

$$Q^i_{j,k} = \text{round}\left(\log_2\left(\frac{\boldsymbol{\Psi}^i_{j,k}(t,0)}{\boldsymbol{\Psi}^i_{j,k}(t/2,0)}\right)\right) \tag{4.10}$$

We term this scheme entrywise leading order interpolation. Note that we have written expressions for $\boldsymbol{\Phi}(\alpha t, 0)$, but assuming that the Jacobian of the dynamics stays nearly constant over a short time interval, $\boldsymbol{\Phi}(t_0 + \alpha t, t_0) = \boldsymbol{\Phi}(\alpha t, 0)$ for some arbitrary t_0 if $t_0 + \alpha t \leq t$. The same is true for $\boldsymbol{\Psi}$. The primary benefit of this form of interpolation is that Eq. 4.5 only requires a single multiplication per entry of the matrix. This means that we take almost as little time as entrywise linear interpolation, but manage higher-order approximations for most entries. Only the powers of α need to be calculated online when the desired value of α is known. Note that P and Q need only be computed one time for a given dynamical system, regardless of the reference orbit.

We emphasize that most terms in the STM and STT are well approximated for small t by higher-order polynomials and not by linear functions. Thus, we expect leading order interpolation to significantly outperform linear interpolation of the STM and STT. To compare short time interpolation approximations using entrywise linear interpolation (Eq. 4.1) with entrywise leading order interpolation (Eq. 4.5), we refer to Fig. 4.7 which depicts the results of using either approximation in the prediction of maneuver costs in the circular restricted three-body problem. The resulting errors are two orders of magnitude lower when leading order interpolation is used instead of linear interpolation.

4.3 Optimal Control Problem

We examine the energy optimal unconstrained thrust problem as outlined in [16, 70]. While energy is not the most applicable metric for fuel use, this problem is more tractable for treatment with variational equations than the fuel optimal and bounded thrust problems, which possess discontinuous derivatives in the mass or costate equations stemming from the switching function in the bang-bang control [16].

The governing dynamical system without control is given by Eq. 1.5. For example, later in this paper, we will specifically analyze optimal control in the circular restricted three body problem given by Eq. 1.2, though we emphasize that the dynamical system employed can be as arbitrary as that given by Eq. 1.5. We seek to satisfy twelve boundary conditions on the initial and final states which are each six dimensional vectors consisting of three dimensional position and velocity $\mathbf{x} = [\mathbf{r}^T \quad \mathbf{v}^T]^T$

$$\mathbf{x}(t_0) = \mathbf{x}_0, \quad \mathbf{x}(t_f) = \mathbf{x}_f \tag{4.11}$$

Simultaneously, we seek to minimize the quadratic integral in the control vector $\mathbf{u}$

$$J = \int_{t_0}^{t_f} \frac{1}{2}\mathbf{u}^T\mathbf{u}\,\mathrm{d}t \tag{4.12}$$

The Hamiltonian corresponding to this problem and the dynamical system given by Eq. 1.5 is

$$H = \frac{1}{2}\mathbf{u}^T\mathbf{u} + \boldsymbol{\lambda}^T\mathbf{F} + \mathbf{p}^T\mathbf{u} \tag{4.13}$$

where $\boldsymbol{\lambda}$ is a six dimensional collection of costates and $\mathbf{p} = (\lambda_4, \lambda_5, \lambda_6)^T$. The resulting system of twelve ordinary differential equations is given by Eq. 1.5 augmented with the control $\mathbf{u}$ on the last three components and

$$\frac{d}{dt}\boldsymbol{\lambda} = -\left(\frac{\partial \mathbf{F}(\mathbf{x})}{\partial \mathbf{x}}\right)^T \boldsymbol{\lambda} \tag{4.14}$$

A two-point boundary value problem arises from Eqs. 1.5 and 4.14 along with the boundary conditions from Eq. 4.11. Solution of this system yields the optimal control effort $\mathbf{u} = -\mathbf{p}$ as a function of the initial costates after integration of the system. From these, Eq. 4.12 can be integrated and the performance metric can be evaluated. Typically, repeated numerical integration as a part of a shooting method is required for the solution of this indirect optimal control problem. Note that the solution of the two-point boundary value problem gives only necessary conditions for an optimal trajectory and that the generalized Legendre–Clebsch conditions along the trajectory should be checked as an additional necessary conditions for local optimality,

$$\frac{\partial^2 H}{\partial u^2} > 0 \tag{4.15}$$

We attempt to perform numerical integration of variational equations ahead of time to avoid numerical integration each time a new optimal control problem needs to be solved online. By using the variational equations, we assume that our optimal control occurs in a neighborhood of some reference trajectory.

4.4 Approximate Optimal Relative Control

Assume an uncontrolled reference trajectory with initial conditions $\mathbf{x}(0) = \mathbf{x}_0$, following the dynamics given in Eq. 1.5 until it reaches state $\mathbf{x}(t_f) = \mathbf{x}_f$ at some final time t_f. This reference trajectory represents the natural motion of some chief satellite under a given set of dynamics. We are interested in controlling another nearby deputy satellite with initial state $\mathbf{x}_0 + \delta\mathbf{x}_0$, so that it arrives at the final desired state $\mathbf{x}_f + \delta\mathbf{x}_f$ at some time t_f. $\delta\mathbf{x}(t)$ is the relative state at time t and gives the difference in state between the deputy and chief satellite states.

We now turn to the approximation of solutions to our optimal control problem and the performance metric. Consider the augmented state vectors for the reference trajectory

$$\mathbf{y} = [\mathbf{x}^T \quad \boldsymbol{\lambda}^T]^T, \quad \mathbf{z} = [\mathbf{x}^T \quad \boldsymbol{\lambda}^T \quad J]^T \tag{4.16}$$

We may calculate the solutions to the first and second-order variational equations as described in Section 1, applied to the augmented system for $\mathbf{z}$

$$\frac{d}{dt}\mathbf{z} = \mathbf{G}(\mathbf{z}) = \left[\left(\mathbf{F}(\mathbf{x})^T + \begin{bmatrix} \mathbf{0} & \mathbf{u}^T \end{bmatrix} \right) \quad -\boldsymbol{\lambda}^T \left(\frac{\partial \mathbf{F}(\mathbf{x})}{\partial \mathbf{x}} \right) \quad \frac{1}{2}\mathbf{u}^T\mathbf{u} \right]^T \tag{4.17}$$

In particular, the variational equations can be solved about the reference trajectory without control applied. In this case, the initial costates of the reference orbit are all set to zero ($\boldsymbol{\lambda}_0 = \mathbf{0}$). The resulting state transition matrix $\mathbf{\Phi}$ and tensor $\mathbf{\Psi}$ can be used to approximately describe natural and optimally controlled motion in the vicinity of the reference trajectory. Note that even though the costates of the reference trajectory will stay zero over the entire trajectory, the sensitivity of states to variations in the initial costates reflected in the STM and STT will not be zero since the first six components of the dynamics $\mathbf{G}(\mathbf{z})$ depend linearly on the control $\mathbf{u}$ which is given by the last three costates. The optimal control problem of relative motion given a specified initial relative state $\delta\mathbf{x}_0$ and final relative state $\delta\mathbf{x}_f$ can then be solved up to first-order in the following manner:

$$\delta\boldsymbol{\lambda}_0 \approx \left(\mathbf{\Phi}^{\mathbf{x}}_{\boldsymbol{\lambda}}(t_f, t_0)\right)^{-1} \left(\delta\mathbf{x}_f - \mathbf{\Phi}^{\mathbf{x}}_{\mathbf{x}}(t_f, t_0)\delta\mathbf{x}_0\right) \tag{4.18}$$

where

$$\mathbf{\Phi}^{\mathbf{a}}_{\mathbf{b}}(t_f, t_0) = \frac{\partial \mathbf{a}(t_f)}{\partial \mathbf{b}(t_0)} \tag{4.19}$$

However, the performance metric $J(t_f) = J_f$ cannot be approximated by the first-order variational equations given that it is defined by a quadratic term (it can be approximated, but only trivially as zero). For this, we require the second-order variational equations:

$$J_f \approx \frac{1}{2} \mathbf{\Psi}^{J}_{\boldsymbol{y},\boldsymbol{y}}(t_0, t_f) \delta \mathbf{y}_0 \delta \mathbf{y}_0 \tag{4.20}$$

with

$$\mathbf{\Psi}^{\mathbf{a}}_{\mathbf{b},\mathbf{c}}(t_f, t_0) = \frac{\partial^2 \mathbf{a}(t_f)}{\partial \mathbf{b}(t_0) \partial \mathbf{c}(t_0)} \tag{4.21}$$

Since J is an inherently quadratic quantity, $\mathbf{\Phi}^{J}_{a} = \delta^{J}_{a}$ where δ^{J}_{a} is the Kronecker delta. A consequence of this fact is that the generalized cocycle conditions (Eq. 1.16) for the energy component of the second-order state transition tensor are independent of other components of the second-order state transition tensor:

$$\mathbf{\Psi}^{J}_{j,k}(t_2, t_0) = \mathbf{\Psi}^{J}_{l,m}(t_2, t_1) \mathbf{\Phi}^{l}_{j}(t_1, t_0) \mathbf{\Phi}^{m}_{k}(t_1, t_0) + \mathbf{\Psi}^{J}_{j,k}(t_1, t_0) \tag{4.22}$$

Additionally, we may improve the approximation of $\delta \boldsymbol{\lambda}_0$ from Eq. 4.18 by using Newton's method to numerically solve Eq. 4.23 for $\delta \boldsymbol{\lambda}_0$ given $\delta \mathbf{x}_0$ and $\delta \mathbf{x}_f$:

$$\delta \mathbf{x}_f \approx \mathbf{\Phi}^{\mathbf{x}}_{\mathbf{y}} \delta \mathbf{y}_0 + \frac{1}{2} \mathbf{\Psi}^{\mathbf{x}}_{\mathbf{y},\mathbf{y}} \delta \mathbf{y}_0 \delta \mathbf{y}_0 \tag{4.23}$$

where the Jacobian $\mathbf{\Phi}^{\mathbf{x}}_{\boldsymbol{\lambda}}$ is used as the derivative in the Newton iteration scheme. Note that the reference trajectory is trivially the globally optimal solution of the energy minimal control problem with boundary conditions $\mathbf{x}(0) = \mathbf{x}_0$ and $\mathbf{x}(t_f) = \mathbf{x}_f$ given that it satisfies the boundary conditions without any control effort. The generalized Legendre–Clebsch condition is satisfied along the reference trajectory, and further, $\frac{\partial^2 H}{\partial u^2} > 0$ on a neighborhood around the reference trajectory. For sufficiently small $\delta\mathbf{x}_0$ and $\delta\mathbf{x}_f$ as well as nonsingular $\mathbf{\Phi}^{\mathbf{x}}_{\boldsymbol{\lambda}}(t_f, t_0)$, the generalized Legendre–Clebsch condition will also be satisfied along the controlled deputy satellite trajectory, ensuring that the control is a local minimum for the cost function in Eq. 4.12.

To summarize: given an initial time t_0, final time t_f and a reference trajectory we can compute the STM and STT associated with energy optimal control around that reference orbit by integrating Eqs. 1.9 and 1.15 with the vector field given by Eq. 4.17. In the case of an original dynamical system that is 6-dimensional, the resulting system will be 13-dimensional consisting of states, costates, and the energy cost. Given a relative motion boundary value problem where initial relative state $\delta\mathbf{x}_0$ and final relative state $\delta\mathbf{x}_f$ are specified, Eq. 4.18 or Eq. 4.23 allow for a solution of $\delta\boldsymbol{\lambda}_0$ directly or by Newton iteration, respectively. This solves our optimal relative motion control problem, up to first or second-order. The states, costates, and energy can be propagated from this initial solution by using the second-order approximation of the dynamics. In particular, the maneuver cost is given by Eq. 4.20. In this manner, we can approximately solve for the cost of any relative optimal control problem with arbitrary boundary conditions sufficiently close to a reference orbit given a fixed initial epoch and time of flight for the reference trajectory.

4.5 Precomputation of Variational Data

In order to expand our methodology to solve optimal relative control problems with arbitrary boundary conditions as well as arbitrary initial epoch and time of flight along a reference orbit, we turn to cocycle conditions and develop a methodology to interpolate variational data.

We detail an algorithm consisting of a precomputation and storage phase, along with a second online phase in which specific optimal control problems are solved. The precomputation assumes a given reference orbit, specified by initial conditions as well as a time range. For a periodic orbit, the time range can be assumed infinite. A discretization size of 2^m given $m \in \mathbb{N}$ is chosen and the time range or period is broken into 2^m intervals of equal length. Along each interval, the reference trajectory variational equations are integrated, and the first and second-order state transition tensors $\boldsymbol{\Phi}(\Delta_{m,j}), \boldsymbol{\Psi}(\Delta_{m,j})$ along the intervals $\Delta_{m,j}$ are stored with

$$\Delta_{m,j} = \left(T_0 + \frac{T_f - T_0}{2^m} j, T_0 + \frac{T_f - T_0}{2^m}(j+1)\right) \tag{4.24}$$

where T_0 and T_f give the initial and final epochs of the reference trajectory under consideration. For a periodic orbit T_0 is assumed to be zero, and T_f is the period of the orbit.

The cocycle property and generalized cocycle property in equations 1.12 and 1.16 can be used to calculate and store $\boldsymbol{\Phi}(\Delta_{i,j}), \boldsymbol{\Psi}(\Delta_{i,j})$ for decreasing values of i from $m-1$ to 0. This yields precomputed variational data at $m+1$ different levels of discretization, all the way from our original finest discretization on up to state transition tensors for the entire reference trajectory (or periodic orbit) at $i = 0$. Figure 4.2 depicts the multi-level discretization of a periodic orbit. In it, $\Delta_{i,j}$ is shown for various indices along the first half of the orbit up to the mth level of discretization. While our method is depicted with a periodic orbit, it will work for finite time horizons on non-periodic orbits without modification. This can be useful when modeling in a higher fidelity model where the reference satellite performs

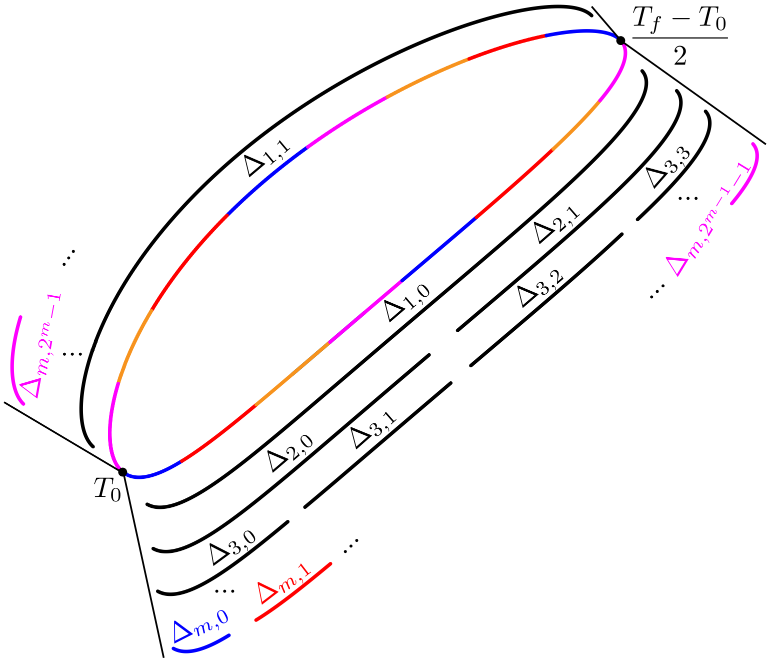

Figure 4.2: A notional multi-level discretization of a periodic orbit with the halfway point in time labeled.

trajectory correction maneuvers, and the reference trajectory can be recomputed and used between each of these. This concludes the precomputation step of the algorithm, which requires approximately $2^{m+1}(2n)^2$ floating point entries of data to be stored for the first-order state transition tensor, an additional $2^{m+1}(2n)^2$ entries for the second-order sensitivity of the performance metric J, and optionally $2^{m+1}(2n)^3$ entries for $\mathbf{\Psi}^{\mathbf{y}}_{\mathbf{yy}}$ where n is the dimension of the state variables and $2n$ is the dimensions of the combined states and costates. Note that in order to use second-order terms to find an improved set of initial costates, $\mathbf{\Psi}^{\mathbf{x}}_{\mathbf{y},\mathbf{y}}$ is all that is required for Eq. 4.23. However, unlike the STT associated with energy J, an STT associated with the states over a given time interval $\mathbf{\Psi}^{\mathbf{x}}_{\mathbf{yy}}(t_2, t_0)$ depends on the STT associated with costates along a smaller subinterval $\mathbf{\Psi}^{\boldsymbol{\lambda}}_{\mathbf{yy}}(t_1, t_0)$ in the generalized cocycle conditions from Eq. 1.16. Thus, the STTs for the states and costates must be stored along intervals even if the STTs for costates do not need to be known for their own sake. For a relatively fine discretization ($m = 7$ giving slightly less than single day precision on a six month Sun-Earth L2 Halo orbit), and storage of all first and second-order variational information in double precision format, storage requirements amount to approximately 4 megabytes which fits manageably within the RAM of a modern desktop computer. Cutting second-order variational information that does not pertain to fuel usage (since Eq. 4.22 only relies on portions of the second-order state transition tensor), leads to memory usage on the order of hundreds of kilobytes. In the future, a method of storing sparse directional variational data rather than the whole variational system could cut storage requirements by orders of magnitude at some cost to accuracy [14]. A Fourier representation of the variational data along a periodic orbit may also be a possible way to reduce storage costs though we do not explore that further here [50]. A cubic spline interpolation framework has also been suggested [31].

For the online stage of the algorithm, many optimal relative control problems may be solved in succession. Given arbitrary t_0, t_f in the time range corresponding to the precomputed reference trajectory, $\mathbf{\Phi}(t_f, t_0), \mathbf{\Psi}(t_f, t_0)$ are computed with the cocycle conditions by piecing together precomputed state transition tensors.

Specifically, the lowest index i^* is found where there exists j^* such that $\Delta_{i^*,j^*} \subseteq (t_0, t_f)$. From here, the process is repeated on the left and right disconnected portions of the original interval with the inner interval removed, $(t_0, t_f) \setminus \Delta_{i^*,j^*}$. A running approximation of the state transition tensors is kept using the cocycle conditions. This continues until $i = m$, at which point $\mathcal{O}(m)$ operations have taken place and the state transition tensors approximations are $\mathbf{\Phi}(t'_f, t'_0), \mathbf{\Psi}(t'_f, t'_0)$ where $0 \leq t'_0 - t_0, t_f - t'_f \leq (T_f - T_0)2^{-m}$.

We approximate $\mathbf{\Phi}(t'_0, t_0), \mathbf{\Psi}(t'_0, t_0)$ as well as $\mathbf{\Phi}(t_f, t'_f), \mathbf{\Psi}(t_f, t'_f)$ and then use the cocycle conditions to augment $\mathbf{\Phi}(t'_f, t'_0), \mathbf{\Psi}(t'_f, t'_0)$ and come up with our final approximation of $\mathbf{\Phi}(t_f, t_0), \mathbf{\Psi}(t_f, t_0)$. We may use the entrywise leading order interpolation scheme from equations 4.5 and 4.8 where $\alpha = \frac{t_0' - t_0}{\|\Delta_{m,j}\|}$ given that $(t_0, t_0') \subseteq \Delta_{m,j}$ or $\alpha = \frac{t_f - t_f'}{\|\Delta_{m,j}\|}$ given that $(t_f', t_f) \subseteq \Delta_{m,j}$.

With approximations for $\mathbf{\Phi}(t_f, t_0)$ and $\mathbf{\Psi}(t_f, t_0)$ obtained in $\mathcal{O}(mn^3)$ and $\mathcal{O}(mn^4)$ operations, respectively (due to matrix and tensor multiplication in the cocycle equations), we may solve Eq. 4.18 with cost dominated by a single solution of an n dimensional linear system with $\mathcal{O}(n^3)$ complexity. Any future boundary value problems with the same boundary times can be solved in $\mathcal{O}(n^2)$ time as long as the relevant LU factorization is stored from the first solution of Eq. 4.18. The estimate of the performance metric in Eq. 4.20 also only requires $\mathcal{O}(n^2)$ operations.

A relevant question is how to choose the level of discretization m. This choice will vary based on the dynamical system, specific reference orbit, and the relative tolerance for error. In order to tune m, one can examine each of the smallest subintervals, approximating the STM and STT along one half of the subinterval by entrywise leading order interpolation. These approximations can be compared against the true value of the STM along the half subinterval. The norm of their difference normalized by the norm of the true STM gives an approximation for the relative error in forward computations involving the STM. The level of discretization, m, can be increased until this relative error approximation is at an acceptable level. To check whether a given m satisfies specific absolute tolerances for computations with bounded relative states over bounded control time horizons, one can perform comparisons of full fidelity calculations against their approximate counterparts when the control time windows are chosen to begin and end at midpoints of the smallest subintervals. The largest distances within that region of application, and the longest time horizons for control should be used as these will generate the highest absolute errors. See Fig. 4.5 and Fig. 4.6 as well as relevant discussion for an example of this process.

It is worth emphasizing that the computation of the STM and STT ahead of time could need to be repeated if for any reason the reference orbit of interest changes over time. In this situation, the computation of the STM and STT along each subinterval takes the same amount of time as it would to calculate one single sweep of the STM and STT over the whole period of interest. In the case of a periodic orbit, this would amount to around one to two orders of magnitude more computation time than the very standard operation of numerically integrating the STM to find the monodromy matrix of the original six-dimensional dynamical system.

4.6 Applications

4.6.1 Controlled Circular Restricted Three Body Problem

The equations of motion for the circular restricted three-body problem are given in the synodic frame as

$$\mathbf{F}(\mathbf{x}) = \begin{bmatrix} \dot{x} \\ \dot{y} \\ \dot{z} \\ 2\dot{y} + \frac{\partial \overline{U}}{\partial x} + u_x \\ -2\dot{x} + \frac{\partial \overline{U}}{\partial y} + u_y \\ \frac{\partial \overline{U}}{\partial z} + u_z \end{bmatrix} \tag{4.25}$$

where the state vector is $\mathbf{x} = [x, y, z, \dot{x}, \dot{y}, \dot{z}]^T$, $\mathbf{u} = [u_x, u_y, u_z]^T$ denotes the control acceleration, an over dot denotes time derivative, and $\overline{U}(x, y, z) = \frac{1-\mu^*}{||\mathbf{r}_1||} + \frac{\mu^*}{||\mathbf{r}_2||} + \frac{x^2+y^2}{2}$ is the effective potential given the reduced mass $\mu^* = \frac{m_2}{m_1+m_2}$ for the two primary bodies with mass m_1, m_2 located along the x-axis at $[-\mu^*, 0, 0]$ and $[1-\mu^*, 0, 0]$ with respect to their common barycenter at the origin. $\mathbf{r}_1, \mathbf{r}_2$ give the position of the satellite of interest with respect to the two primary bodies respectively [70].

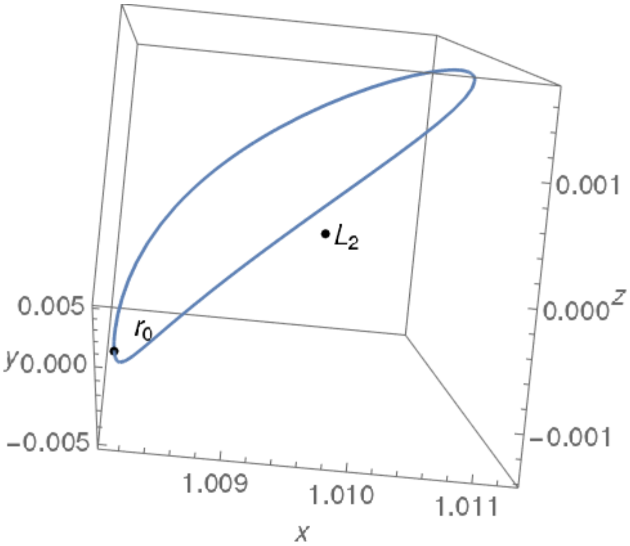

Figure 4.3: The reference Sun-Earth L2 Halo orbit in canonical distance units.

We present an example around a Sun-Earth L2 Halo orbit with initial out-of-plane position of 986,000 km shown in canonical units in Fig. 4.3. Note that all numerical integration from this point forward is performed with an Adams/BDF adaptive step method with absolute local truncation error kept below 10^{-8} in canonical units, though fixed time step methods are typically recommended for STM and STT computation [97]. We show the cost for a deputy satellite to rendezvous with the reference orbit after two weeks when the deputy begins on a 10,000 km radius sphere centered at the reference orbit initial position with the same rotating frame velocity as the reference satellite. While our methodology allows for computation of transfers to and from arbitrary relative states, we chose the rendezvous problem from a sphere to the origin in order to reduce the dimensions of the space for visualization and demonstration purposes. A radius of 10,000 km was chosen to stress the method, and because this value is on the order of distances proposed in starshade mission design [70]. In that application, the starshade nominally transfers between points on some baseline sphere around the telescope while maintaining zero relative inertial velocity at the boundaries to enable observation of exoplanets. However, the cost of transfers between arbitrary points on the sphere in this application setting is difficult to visualize given the four-dimensional design space. Figure 4.4 shows eight examples of energy optimal rendezvous trajectories from points on the 10,000 km sphere to the reference trajectory at the origin. Initial costates for the rendezvous were solved with Newton iteration on Eq. 4.23, and then the states and costates were propagated with the same equation. Note that the out-of-plane rendezvous trajectory stays approximately rectilinear.

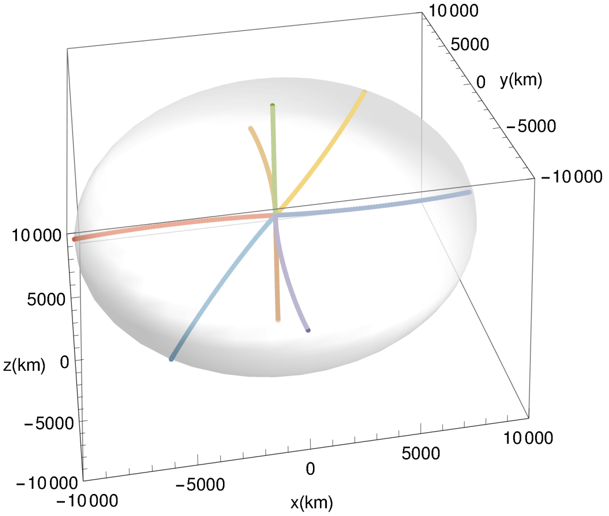

Figure 4.4: Eight examples of the two week rendezvous trajectories from the 10,000 km sphere around the reference orbit.

The control cost J from Eq. 4.12 is given in Fig. 4.5, where initial position on the sphere is parameterized by the ecliptic longitude θ, measured counterclockwise from the x-axis, and the ecliptic latitude $\mathbf{\Phi}$, measured from the ecliptic. This figure takes less than a second to generate using the second-order approximation to the initial costate solution and the second-order approximation to the cost J. We see that the optimal control cost varies by about 25% of its maximum value depending on the initial location, with lowest cost starting relative positions roughly orthogonal to the reference orbit to Sun vector. This feature was found in almost no computation time at all; however, we are more interested in the methodology and how it performs.

Figure 4.6 shows the error in the final position in kilometers of the deputy satellite given the control derived in two different ways: first, by solving for a second-order approximation in Eq. 4.23 using Newton's method (with a 10^{-8} tolerance), and second by the first-order approximation in Eq. 4.18. These errors are calculated by direct numerical integration of the initial states and costates calculated by the two approximation methods. Errors in the final position are on the order of 0.01% and 0.1% of the distance traversed for the second-order and first-order approximations, respectively. In simulations below 1,000 km distances, negligible difference in the position error between the two approximations is achieved, while the error from the linear approximation varies linearly with the distance. As relative distances increase beyond 10,000 km and exceed 100,000 km, the final position error rapidly increases, as the approximated optimal control problem becomes increasingly far removed from the actual optimal control problem.

Figure 4.5 also shows that errors in the estimated control cost from Eq. 4.20 are on the order of 0.1% percent of the actual cost computed by numerical integration along the approximately computed trajectory. This means that the second-order state transition tensor gives a reliable indicator of the performance metric of the optimal control that we can calculate without online numerical integration. Interestingly, the error is zero seemingly along a great circle on the sphere of initial locations of the deputy satellite. This great circle also happens to correspond to the locations of minimal cost rendezvous.

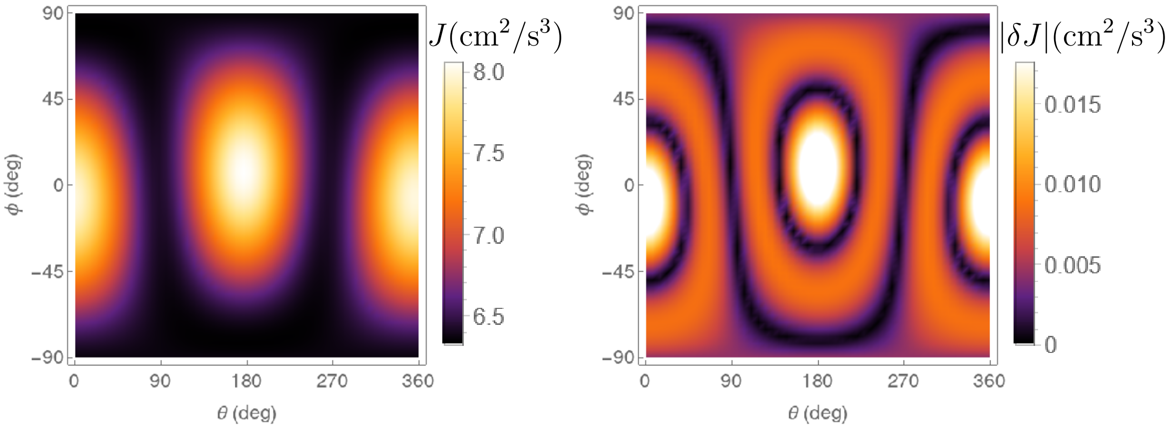

Figure 4.5: The rendezvous control cost approximated by second-order state transition tensor and the error in its approximation versus numerical integration.

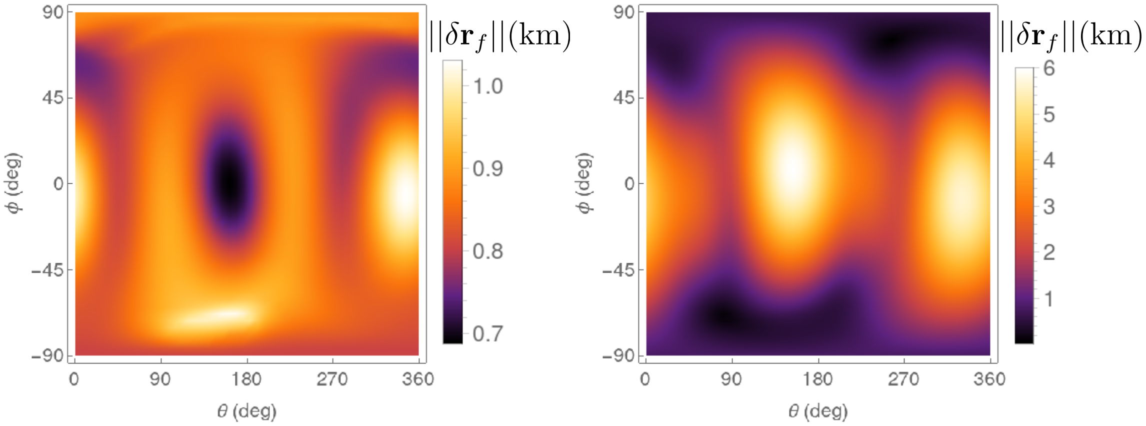

Figure 4.6: The error in final position due to the approximation of the rendezvous optimal control by second-order and first-order methods respectively.

We examine the worst-case error when computing the energy cost J using STTs at the $m = 7$ level of discretization (the finest level of granularity is a little over a day) for 5,000 randomly generated transfers from the 10,000 km sphere around the chief satellite to the chief satellite. This test is conducted over time spans from 1 to 30 days. Worst-case error is achieved by employing approximated STTs at the end points of the transfer with exactly half the time span of the finest discretization. We see in Fig. 4.7 that error in approximations of cost due to interpolation for 1 to 30 day rendezvous remains below around 0.1 percent of the actual value of the maneuver cost when leading order interpolation is used in the approximation of the STTs at the endpoints. There exists a small bias in the error, such that energy cost of a maneuver tends to be slightly overestimated. On the other hand, when linear interpolation is used for the STTs at the endpoints, we witness up to 30 percent errors in the maneueuver cost. In this case the bias in the calculation dwarfs the support of the distribution of the 5000 points, so that each distribution appears only as a point relative to the scale of the graphs. This serves as evidence of the efficacy of leading order interpolation of linear interpolation for our present problem. The nominal 0.1% effect of the error at the scale of single-day transfers may be sufficient as it is on the same level of fidelity as the use of the STT approximation in the first place as seen in Fig. 4.5. Fidelity may be additionally tuned to desired levels by refining the discretization. Accuracy needs will vary by application, but discretizations with minimum times around one day or $m = 7$ are reasonable in the approximately 0.1 percent error created during interpolation. Any reduction in this error will be balanced by increased

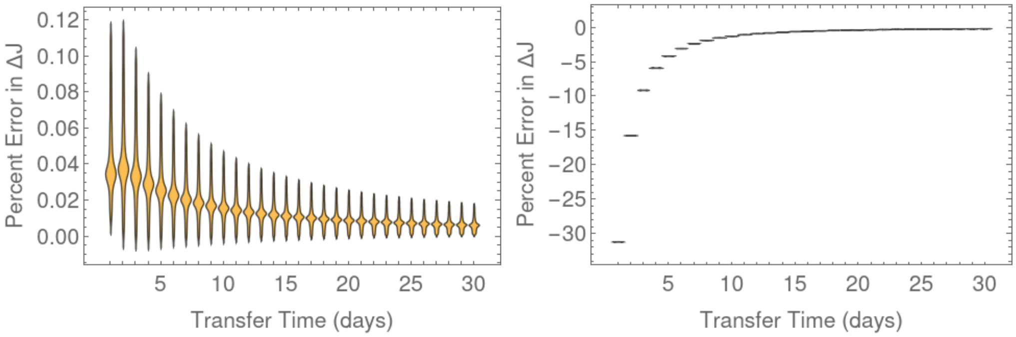

Figure 4.7: Distribution plot of rendezvous cost error from leading order (left) and linear (right) STT interpolation.

memory costs and very small increases in online computational costs due to the number of matrix multiplications required to form the state transition tensors from precomputed components. Dynamical systems that are more sensitive to initial conditions magnify the approximation error in short time STMs as they are used to form a longer time STM. This means that finer discretizations may be required when computing approximate models of relative motion and optimal control in the vicinity of near rectilinear Halo orbits in the Earth-Moon system.

4.6.2 Sensitivity to Earth's Eccentricity

We have presented an application of the STT indirect optimal control interpolation methodology in the circular restricted three-body problem approximation of the Sun-Earth system, but the question remains whether results yielded from this approach on a low fidelity model are valid in higher fidelity models of this system. To answer this question, we examine the sensitivity of our results to the eccentricity in the equations of motion for the elliptical restricted three-body problem (ER3BP) [120].

$$\mathbf{F}(\mathbf{x}) = \begin{bmatrix} \dot{x} \\ \dot{y} \\ \dot{z} \\ 2\dot{y} + \frac{\partial \overline{U}^*}{\partial x} + u_x \\ -2\dot{x} + \frac{\partial \overline{U}^*}{\partial y} + u_y \\ \frac{\partial \overline{U}^*}{\partial z} + u_z \end{bmatrix} \tag{4.26}$$

where the state vector in pulsating coordinates is $\mathbf{x} = [x, y, z, \dot{x}, \dot{y}, \dot{z}]^T$, $\mathbf{u} = [u_x, u_y, u_z]^T$ denotes the control acceleration, an overdot denotes time derivative, and the effective potential is given by

$$\overline{U}^*(x, y, z) = \left(\frac{1-\mu^*}{||\mathbf{r}_1||} + \frac{\mu^*}{||\mathbf{r}_2||} + \frac{x^2+y^2+z^2}{2}\right)\frac{1}{1+e\cos\nu} - \frac{z^2}{2} \tag{4.27}$$

where ν is the true anomaly of the secondary in its elliptical orbit around the common barycenter. $\mathbf{r}_1, \mathbf{r}_2$ give the position of the satellite of interest with respect to the two primary bodies respectively in pulsating coordinates.

For optimal control in the ER3BP, it is important to scale the cost function so that acceleration in a non-pulsating coordinate frame is considered, leading to the energy integral.

$$J = \int_{t_0}^{t_f} \frac{(1+e\cos(\nu))^2}{2(1-e^2)^2}\mathbf{u}^T\mathbf{u}\,\mathrm{d}t \tag{4.28}$$

The differential equation for the costates remains the same as in Eq. 4.14, but the control law is given in pulsating coordinates by

$$\mathbf{u} = -\left(\frac{1-e^2}{1+e\cos(\nu)}\right)^2(\lambda_4, \lambda_5, \lambda_6)^T \tag{4.29}$$

We may examine sensitivity to eccentricity by including the parameter in our augmented state vector and describing the parameter as evolving with a zero time derivative. As noted before, this is not the most efficient method for computing the sensitivities, but is easy to implement in the current STM and STT computational framework with the cost being unnecessary multiplications with the value zero during numerical integration.

$$\mathbf{z}^* = [\mathbf{x}^T \quad \boldsymbol{\lambda}^T \quad J \quad e]^T \tag{4.30}$$

$$\frac{d}{dt}\mathbf{z}^* = \mathbf{G}^*(\mathbf{z}^*) = \left[\left(\mathbf{F}(\mathbf{x})^T + \begin{bmatrix}\mathbf{0} & \mathbf{u}^T\end{bmatrix}\right) \quad -\boldsymbol{\lambda}^T\left(\frac{\partial \mathbf{F}(\mathbf{x})}{\partial \mathbf{x}}\right) \quad \frac{(1+e\cos(\nu))^2}{2(1-e^2)^2}\mathbf{u}^T\mathbf{u} \quad 0\right]^T \tag{4.31}$$

When taking the Jacobian and Hessian of the vector field given in Eq. 4.31, the first and second partial derivatives of ν with respect to e evaluated at $e = 0$ are required. These may be obtained from the series expansion for the equation of center [114]. They are

$$\left.\frac{\partial \nu}{\partial e}\right|_{e=0} = 2\sin(t) \tag{4.32}$$

$$\left.\frac{\partial^2 \nu}{\partial e^2}\right|_{e=0} = 5/2\sin(2t) \tag{4.33}$$

In the second-order Taylor expansion of $\mathbf{z}^*$ with respect to initial states, costates, and the eccentricity of the system, a change in the eccentricity parameter manifests itself in energy cost changes through the mixed partial derivative with respect to e and $\mathbf{y}$. As a result, the second-order approximation of relative position becomes dependent on the STM and STT associated with $\mathbf{G}^*$ integrated around the original trajectory with $e = 0$ as the nominal value of the parameter.

$$\delta \mathbf{x}_f \approx (\mathbf{\Phi}^{\mathbf{x}}_{\mathbf{y}} + \mathbf{\Psi}^{\mathbf{x}}_{\mathbf{y},e} e)\delta \mathbf{y}_0 + \frac{1}{2}\mathbf{\Psi}^{\mathbf{x}}_{\mathbf{y},\mathbf{y}}\delta \mathbf{y}_0 \delta \mathbf{y}_0 \tag{4.34}$$

while Eq. 4.20 for the performance cost remains the same up to second-order. Given an eccentricity value of 0.01671 for the Earth, we quantify the effects of modeling eccentricity on energy costs by comparing the second-order approximation of energy cost from solving Eq. 4.34 and employing Eq. 4.20 versus solving Eq. 4.23 instead. Figure 4.8 shows that the energy cost calculated using Eq. 4.34 and Eq. 4.20 is indistinguishable to the eye when compared with Fig. 4.5 except for a nearly constant increase in the value. The relative changes (neglecting the constant increase) in the energy cost from eccentricity effects are on the order of less than one part in one hundred with respect to the cost anticipated by the CR3BP model. This suggests that the CR3BP model is useful for comparing the cost of relative motion optimal control between different relative states in the vicinity of Halo orbits in the Sun-Earth system. In this simulation, the Earth was assumed to be at perihelion at the initial epoch.

The sensitivity approach taken above to incorporating eccentricity effects allows

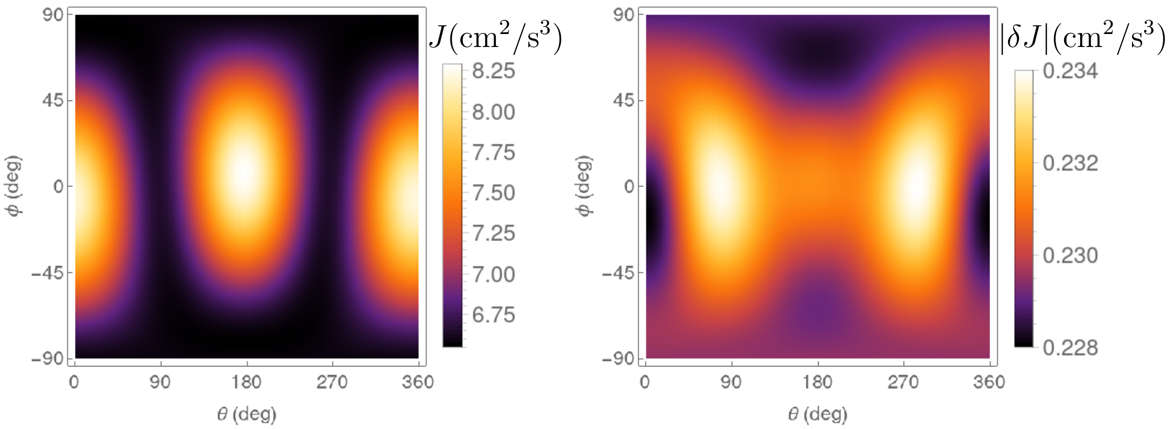

Figure 4.8: The ER3BP rendezvous control cost approximated by second-order state transition tensor and its difference with that calculated using the CR3BP.

one to avoid the problem of finding a corresponding reference orbit in the ER3BP. We present in Fig. 4.9 and Fig. 4.10, the calculation of optimal control costs and errors around an explicit orbit in the ER3BP system. The corresponding orbit we chose was found by taking the initial conditions for the previous Halo orbit, scaling to pulsating coordinates, and performing differential correction to find an orbit which kept the same original out-of-plane amplitude that would intersect the x, z-plane with velocity perpendicular to the plane. With these initial conditions, we used Eq. 4.31 (without the tracking the last zero term corresponding to the eccentricity parameter in this case) with Earth's eccentricity value of $e = 0.01671$ to generate Fig. 4.9 and Fig. 4.10 in exactly the same manner that Eq. 4.17 was used to generate 4.5 and Fig. 4.6. This shows that the approximation error from using the STM and STT in the ER3BP is almost identical to the CR3BP case, though the energy cost is larger by a constant shift than either the CR3BP or the CR3BP with eccentricity sensitivity calculations predicted. The larger, almost constant, shift in the energy cost in this calculation versus the calculation using Eq. 4.34 could come from the specific choice of orbit corresponding to the original Halo, or also from the fact that by not examining sensitivities up to 3rd order in $\mathbf{z}^*$, the sensitivity of energy cost to eccentricity showed up only indirectly in the Eq. 4.34, and not explicitly in a correction to Eq. 4.20. Note that in both simulations, we considered the same 10,000 km sphere of initial conditions, and needed to scale the distances to pulsating coordinates so that the true distances would match between the CR3BP test case and the ER3BP test cases.

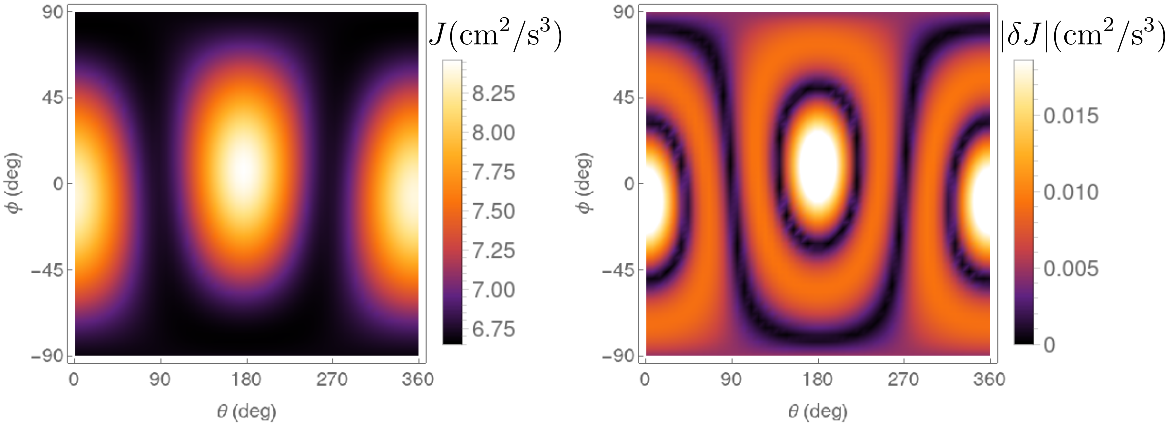

Figure 4.9: The rendezvous control cost approximated by second-order state transition tensor and the error in its approximation versus numerical integration in the ER3BP.

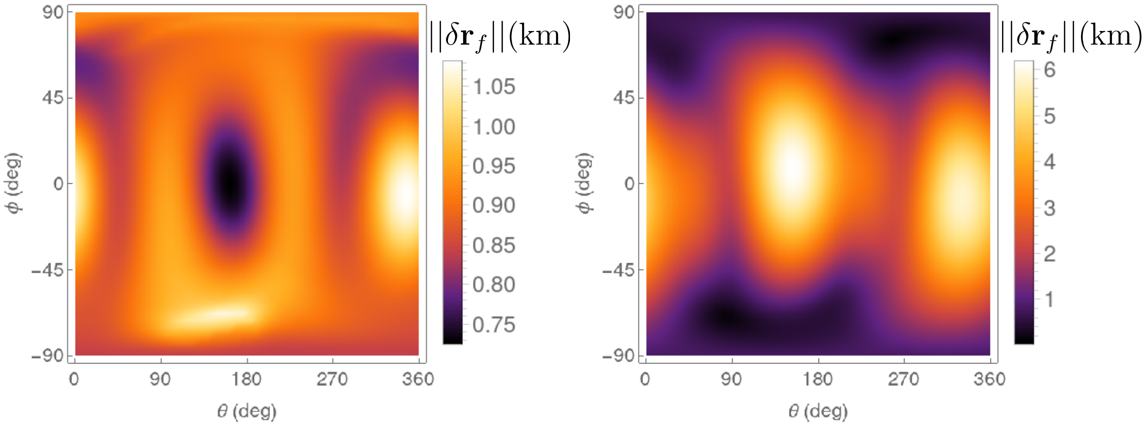

Figure 4.10: The error in final position due to the approximation of the rendezvous optimal control by second-order and first-order methods respectively in the ER3BP.

4.7 Conclusion

We have presented an algorithm for solving any continuous-thrust energy-optimal relative transfer sufficiently close to a given reference trajectory regardless of boundary times or values. Our treatment is agnostic of the specific dynamical system, and the choice of reference orbit; however, 'sufficiently close' amounts to deviations approximately 1 percent of the extent of the reference orbit in the Sun-Earth L2 Halo orbit cases tested. This algorithms consists of a precomputation phase, in which the state transition matrix and second-order state transition tensor associated with energy optimal control of the dynamical system are stored over subintervals of the reference orbit at various levels of discretization size. During the online portions of the algorithm, state transition matrices and state transition tensors are composed using cocycle conditions and are interpolated at the end points of the time interval of interest using a novel interpolation method that exploits the structure of variational equations over short time periods. This leading order interpolation method takes as many operations as linear interpolation but with higher-order accuracy in some terms of the matrices and tensors, depending on the placement of zeros in the Jacobian of the dynamical system. The algorithm requires on the order of megabytes of memory for precomputed variational data in nominal Sun-Earth L2 Halo orbit cases tested, and requires only a small number of matrix/tensor multiplications and solutions of linear systems during the online segment of the algorithm. Importantly, there are no numerical solutions of either ordinary or partial differential equations during the online segment of the algorithm. This leads to fast approximation of solutions which may enable the solution of future problems involving bilevel optimizations. Starshade observation schedule optimization for exoplanet direct imaging missions is one such application in which a bilevel optimization could be necessary. For this application or others, it is important to validate that solutions to the unconstrained optimal control problem do not violate operational constraints on thrust magnitude. Error analysis dependent on the extent of the relative motion in the given system is also important to assure that this algorithm can reasonably be applied in a given situation with either linear or second-order approximations.

A drawback in this method is that only control that is locally optimal about the reference trajectory is considered and the globally optimal control may not be described by the variational equations. Some of this methodology will also fail when the sensitivity of states to costates is singular along a given reference trajectory. Another fundamental limit of this method is its inability to be applied to fuel optimal control problems which lack the requisite smoothness and under which uncontrolled trajectories are singular in some variational sense. Our precomputation method excels when a periodic orbit is known ahead of time, as a finite amount of data can be used to represent the trajectory for all time. However, this methodology can be applied as is to non-periodic orbits over finite horizons. STTs must be recomputed and stored again once that finite time horizon has been passed. While keeping these limitations in mind, the precomputation and interpolation approach taken in this paper is a valuable tool to speed up trajectory optimization and optimal control cost estimation in the vicinity of a known reference orbit.

CHAPTER 5

APPROXIMATE SOLUTION OF THE PASSIVE ANGLES-ONLY ORBIT DETERMINATION PROBLEM

5.1 Introduction

It is a well-known problem that the range between two satellites is unobservable in passive (without maneuvers from the observer or observed satellite), angles-only, relative orbit determination when using a linearization of the dynamics about a single sensor [135]. On the other hand, recent works have determined the scale of relative motion from angles-only measurement by employing nonlinear models of the dynamics. A few works solve polynomial equations arising from second and third-order approximations of the nonlinear dynamics. Some of these methods employ homotopy continuation methods from algebraic geometry or successive approximations to solve the multivariate systems of polynomial equations [85, 132, 133], while another performs approximations to obtain an up to 15th order polynomial in a single variable that can be solved by standard methods for polynomial root finding [98]. Another recent work determines the minimum rate of change of the observation angle over time to determine the scale of certain relative orbits in the 2-body problem, using this technique to perform orbit determination when high frequency arc-second-level accuracy measurements are available [137]. Other methods rely on solving a nonlinear least squares problem. In order for nonlinear least squares algorithms to converge consistently, the initial guess of the scale of the orbit must be close to the true scale. Current algorithms employ bisection methods over the initial scale guess as a means to guarantee convergence at the cost of inefficiency in

---

A previous version of this work was presented at the January 2023 Spaceflight Mechanics Conference in Austin, TX as AAS paper 23-161.

the nested optimization [6, 5]. Other approaches use an iterative method to solve the problem on an observable subspace, while using a sampling method to solve the problem in the orthogonal subspace [64]. Additionally, much work has been performed in solving for the scale of a relative orbit when the camera is offset from the center of mass of a satellite [42, 44, 47, 48], or when multiple cameras are used with a known relative positioning [77].

In this work, we will fuse the approach of solving a nonlinear least squares problem with the use of quadratic models of the relative motion to solve the passive, angles-only, relative orbit determination problem without camera offsets or multiple cameras. Rather than performing nested optimization to make the solution of the nonlinear least squares problem feasible, we provide a fast method for approximating the scale of the relative orbit, which allows a standard, nonlinear least squares solving algorithm such as Gauss-Newton to successfully converge to a solution. Our initial guess generation involves solving an overdetermined eigenvalue problem and relies on state transition tensors as a theoretical underpinning, but can be implemented with only state transition matrix calculations. We will begin by briefly reviewing the theory behind state transition matrices and higher-order state transition tensors. From there, we will present the nonlinear least squares problem associated with passive, angles-only, relative orbit determination as well as the range-ambiguous linear least squares solution for the relative state. Since the direction of the initial relative state vector is known approximately, we will demonstrate that an overdetermined eigenvalue problem naturally arises to determine the unknown scale. The main contributions of this paper lie in developing two algorithms for approximating the scale of the relative of orbit. The first method approximately minimizes a least squares problem associated with the overdetermined eigenvalue problem in a novel manner involving the Moore-

Penrose pseudo-inverse. The second method also gives a novel means of solving the overdetermined eigenvalue problem in a least squares sense, but performs the minimization exactly by constructing an equivalent quadratic eigenvalue problem and solving this by forming the equivalent linear eigenvalue problem in twice as many dimensions. We assess the performance of this method for a Geostationary observer orbit, as well as the proposed NASA Gateway Earth-Moon Near Rectilinear Halo Orbit. Finally, we present an error covariance study of solutions as a function of number of observations, observation window duration, and relative orbit geometry.

5.2 Methodology

5.2.1 Problem Statement

We pose the following nonlinear least squares problem to find the six-dimensional inertial state $\mathbf{x}_0 = [\mathbf{r}_0^T \quad \mathbf{v}_0^T]^T$ consisting of position and velocity for the observed satellite at the initial time t_0:

$$\min_{\mathbf{x}_0} \sum_i \|\mathbf{l}_i \times \delta\mathbf{r}_i\|_2^2 \tag{5.1}$$

where $\mathbf{l}_i$ is the unit vector in the direction of the observation at t_i, and $\delta\mathbf{r}_i$ is the position of the observed satellite relative to the sensor at the time t_i as a function of $\mathbf{x}_0$. The measurement unit vectors $\mathbf{l}_i$ throughout this paper will be modeled with additive measurement error $\mathbf{w}_i$ modeled with the QUEST measurement model:

$$E(\mathbf{w}_i) = \mathbf{0}, \qquad E(\mathbf{w}_i\mathbf{w}_i^T) = \frac{\sigma^2}{2}\left(\mathbf{I}_3 - \mathbf{l}_i\mathbf{l}_i^T\right) = \mathbf{\Sigma}_i \tag{5.2}$$

given a sensor noise standard deviation σ and the 3 by 3 identity matrix denoted as $\mathbf{I}_3$ [110].

5.2.2 Initial Guess Generation

The main novelty of this work lies in the method to generate an approximate solution to the nonlinear least squares problem from Eq. 5.1. We begin by examining the solution to the linearization of Eq. 5.1:

$$\min_{\delta \mathbf{x}_0} \sum_i \|[\mathbf{l}_i]_\times \mathbf{\Phi}^{\mathbf{r}}(\mathbf{x}_0; t_i, t_0)\delta \mathbf{x}_0\|_2^2 \tag{5.3}$$

where $\mathbf{\Phi}^{\mathbf{r}}(\mathbf{x}_0; t_i, t_0)$ is the submatrix consisting of the upper three rows of the STM $\mathbf{\Phi}(\mathbf{x}_0; t_i, t_0)$ associated with the sensor orbit, $\delta \mathbf{x}_0$ is the initial state of the observed satellite relative to the observer satellite, and

$$[\mathbf{l}]_\times = \begin{bmatrix} 0 & -l_3 & l_2 \\ l_3 & 0 & -l_1 \\ -l_2 & l_1 & 0 \end{bmatrix} \tag{5.4}$$

is the skew-symmetric, cross-product equivalent 3 by 3 matrix. Due to well-known linear observability issues, the solution to the linear least squares problem in Eq. 5.3 is not unique [135]. However, by definition of the singular value decomposition and its connection to constrained optimization of a linear function, the unique solution up to a sign with unit norm is given by the right singular vector corresponding to the smallest (sixth largest) singular value of the following $3n$ by 6 matrix:

$$\mathbf{A} = \begin{bmatrix} [\mathbf{l}_1]_\times \mathbf{\Phi}^{\mathbf{r}}(\mathbf{x}_0; t_1, t_0) \\ \vdots \\ [\mathbf{l}_n]_\times \mathbf{\Phi}^{\mathbf{r}}(\mathbf{x}_0; t_n, t_0) \end{bmatrix} \tag{5.5}$$

We denote this range ambiguous (unit-normed) linear solution to the relative orbit determination problem $\bar{\mathbf{x}}_0$. With this linear approximation in hand, we move on to considering a second-order approximation of the nonlinear least squares problem in Eq. 5.1:

$$\min_{\delta \mathbf{x}_0} \sum_i \left\| [\mathbf{l}_i]_\times \left(\mathbf{\Phi}^{\mathbf{r}}(\mathbf{x}_0; t_i, t_0)\delta \mathbf{x}_0 + \frac{1}{2}\mathbf{\Psi}^{\mathbf{r}}(\mathbf{x}_0; t_i, t_0)\delta \mathbf{x}_0^2 \right) \right\|_2^2 \tag{5.6}$$

where we define the 3 by 6 by 6 rank (1,2)-tensor that gives second-order sensitivities of the final position to the initial full state (a block of the full second-order state transition tensor)

$$\mathbf{\Psi}^{\mathbf{r}}(\mathbf{x}_0; t_f, t_0) = \frac{\partial^2 \mathbf{r}_t}{\partial \mathbf{x}_0^2} \tag{5.7}$$

The problem defined in Eq. 5.6 is not a linear least squares problem, and is generally difficult to solve. However, given that $\delta\mathbf{x}_0$ is small relative to the sensor orbit state $\mathbf{x}_0$ in a relative motion context (on the order of 1/100th or less the scale of the reference orbit), the quadratic term should be much smaller than the linear term for any such small $\delta\mathbf{x}_0$. With this information, the solution to the quadratic least squares problem is in approximately the same direction as the solution to the linear least squares problem $\bar{\mathbf{x}}_0$, so

$$\begin{aligned} &\min_{\delta\mathbf{x}_0} \sum_i \left\| [\mathbf{l}_i]_\times \left(\mathbf{\Phi}^{\mathbf{r}}(\mathbf{x}_0; t_i, t_0)\delta\mathbf{x}_0 + \frac{1}{2}\mathbf{\Psi}^{\mathbf{r}}(\mathbf{x}_0; t_i, t_0)\delta\mathbf{x}_0^2 \right) \right\|_2^2 \\ \approx &\min_{\delta\mathbf{x}_0} \sum_i \left\| [\mathbf{l}_i]_\times \left(\mathbf{\Phi}^{\mathbf{r}}(\mathbf{x}_0; t_i, t_0)\delta\mathbf{x}_0 + \frac{\|\delta\mathbf{x}_0\|_2}{2}\mathbf{\Psi}^{\mathbf{r}}(\mathbf{x}_0; t_i, t_0)\bar{\mathbf{x}}_0\delta\mathbf{x}_0 \right) \right\|_2^2 \end{aligned} \tag{5.8}$$

Treating $-\|\delta\mathbf{x}_0\|_2/2$ as an unknown constant λ, we obtain an overdetermined eigenvalue problem in $\delta\mathbf{x}_0$ [30]. To find an approximation for the vector $\delta\mathbf{x}_0$, we solve the overdetermined eigenvalue problem:

$$\min_{\delta\mathbf{x}_0, \lambda} \|\mathbf{A}\delta\mathbf{x}_0 - \lambda\mathbf{B}\delta\mathbf{x}_0\|_2 \tag{5.9}$$

where $\mathbf{B} \in \mathbb{R}^{3n\times 6}$ is given by:

$$\mathbf{B} = \begin{bmatrix} [\mathbf{l}_1]_\times \mathbf{\Psi}^{\mathbf{r}}(\mathbf{x}_0; t_1, t_0)\bar{\mathbf{x}}_0 \\ \vdots \\ [\mathbf{l}_n]_\times \mathbf{\Psi}^{\mathbf{r}}(\mathbf{x}_0; t_n, t_0)\bar{\mathbf{x}}_0 \end{bmatrix} \tag{5.10}$$

given matrices $(\mathbf{\Psi}^{\mathbf{r}}(\mathbf{x}_0; t_f, t_0)\delta\mathbf{x})^i_j = (\mathbf{\Psi}^{\mathbf{r}})^i_{jk}(\mathbf{x}_0; t_f, t_0)\delta x^k$ and $\mathbf{A}$ defined as in Eq. 5.5. We call this linear approximation of the (1,2)-tensor $\mathbf{\Psi}^{\mathbf{r}}$ a quasi-linearization about the vector $\bar{\mathbf{x}}_0$. By performing a single contraction, $\mathbf{\Psi}^{\mathbf{r}}\bar{\mathbf{x}}_0$ yields a matrix that gives an approximation of $\mathbf{\Psi^r}$ as it acts on vectors in the vicinity of $\bar{\mathbf{x}}_0$. In general, when $\mathbf{A}$ and $\mathbf{B}$ have more rows than columns, there are no generalized eigenvectors [30]. Instead, as justified in the section A.1, we approximately solve the problem in a least squares sense by solving the standard eigenvalue problem with a Moore-Penrose pseudo-inverse term $\mathbf{A}^\dagger$. We choose to apply the pseudo-inverse to the $\mathbf{A}$ matrix rather than $\mathbf{B}$, as $\mathbf{B}$ is only a linear approximation of a quadratic term, while $\mathbf{A}$ contains no approximations. Numerical experiments show that the formulation with the pseudo-inverse of $\mathbf{A}$ tends to decrease error over performing the pseudo-inverse on $\mathbf{B}$ in the orbit fit arising from the solution of the eigenvalue problem. In the subsequent examples, inversions of the $\mathbf{B}$ matrix exhibited worse error in the orbit fit in all cases tested and have been omitted. Our approximate reformulation of Eq. 5.9 becomes

$$\mathbf{A}^\dagger \mathbf{B} \delta \mathbf{x}_0 = \lambda^* \delta \mathbf{x}_0 \tag{5.11}$$

where $\lambda^* = 1/\lambda$. The quadratic approximation for $\delta \mathbf{x}_0$ becomes the eigenvector of $\mathbf{A}^\dagger \mathbf{B}$ closest to the original vector $\bar{\mathbf{x}}_0$ (up to a sign), multiplied by $-2/\lambda^*$. Note that care should be taken to ensure the sign of the solution agrees with the direction of the line of sight vector observations and not their opposites. Additionally, there are no guarantees that the computed eigenvectors will be real-valued, since the matrices are not strictly real symmetric or positive definite. As a result, numerical error may manifest itself in the form of complex values. The imaginary components of these solutions should be ignored by considering the real part of vectors denoted by $\mathrm{Re}(\cdot)$ since the orbit fit must be real and these imaginary components are small in practice. Finally, note that $A^\dagger$ can be computed easily from the singular value decomposition of A that was performed in an earlier stage of the algorithm [46]. A summary of the details of the algorithm solving Eq. 5.11 and addressing sign and complex value concerns can be found in Alg. 1. While an approximation is made to go from the overdetermined eigenvalue problem in Eq. 5.9 to the standard eigenvalue problem in Eq. 5.11, we can also solve the original problem exactly. The least squares problem in Eq. 5.9 can be reframed as a generalized eigenvalue problem in twice as many dimensions by the linearization of an associated quadratic eigenvalue problem as outlined in Sec. A.2. Alg. 2 provides details on using the quadratic eigenvalue problem approach to the overdetermined eigenvalue problem to solve Eq. 5.9 directly. Note the multiplication rather than division by the eigenvalue in the final solution as compared to Alg. 1

Note that Eq. 5.9 depends on the second-order state transition tensor. Computation of the second-order state transition tensor is nowhere near as commonly implemented as computation of state transition matrices in astrodynamics software. We demonstrate that the second-order state transition tensor need not be directly computed, and only some information from the tensor is required. Rather than directly computing the second-order state transition tensor and then performing the contraction with $\bar{\mathbf{x}}_0$, we can employ a forward finite difference to compute the directional derivative of the STM:

$$\mathbf{\Psi}^{\mathbf{r}}(\mathbf{x}_0; t_i, t_0)\bar{\mathbf{x}}_0 \approx \frac{\mathbf{\Phi}^{\mathbf{r}}(\mathbf{x}_0 + h\bar{\mathbf{x}}_0; t_i, t_0) - \mathbf{\Phi}^{\mathbf{r}}(\mathbf{x}_0; t_i, t_0)}{h} \tag{5.12}$$

for small h. This can speed up computation and save programming time, since state transition tensor computations are implemented much less commonly than state transition matrix computations. Also, extraneous information in the state transition tensor is not computed when using this approach as the second-order sensitivity is only required along the single direction $\bar{\mathbf{x}}_0$.

Both Alg. 1 and Alg. 2 rely only on standard methods from numerical linear algebra to approximate the relative orbit initial state. Average timing results run on a standard laptop computer for both algorithms applied to data with varying

Algorithm 1: The pseudo-inverse eigenvalue algorithm to obtain an initial guess for the passive angles-only relative orbit determination problem.

```
Input: $\mathbf{l}_i$, $\mathbf{x}_0$
Compute $\mathbf{\Phi}^{\mathbf{r}}(\mathbf{x}_0; t_i, t_0)$
Compute $\mathbf{A}$ from Eq. 5.5
Compute the SVD of $\mathbf{A}$
    $\bar{\mathbf{x}}_0 \leftarrow \mathbf{v}_6(\mathbf{A})$ the sixth right singular vector (unit vector)
    $\bar{\mathbf{x}}_0 \leftarrow \bar{\mathbf{x}}_0 * \mathrm{sign}(\mathbf{l}_1^T \mathbf{\Phi}^{\mathbf{r}}(\mathbf{x}_0; t_1, t_0)\bar{\mathbf{x}}_0)$
Compute $\mathbf{\Psi}^{\mathbf{r}}(\mathbf{x}_0; t_i, t_0)\bar{\mathbf{x}}_0$        ▷ directly, or with Eq. 5.12
Compute $\mathbf{B}$ from Eq. 5.10
Compute $\mathbf{A}^\dagger \mathbf{B}$        ▷ where $\mathbf{A}^\dagger$ can be computed from the known SVD of $\mathbf{A}$
Compute the eigenvectors of $\mathbf{A}^\dagger \mathbf{B}$.
Select the eigenpair $(\hat{\mathbf{x}}_i, \lambda_i^*)$ s.t. $i = \mathrm{argmax}_j |\hat{\mathbf{x}}_j \cdot \bar{\mathbf{x}}_0|$
Let $\delta\mathbf{x}_0 \leftarrow \mathrm{Re}(-2\hat{\mathbf{x}}_i / \lambda_i^*)$
$\delta\mathbf{x}_0 \leftarrow \delta\mathbf{x}_0 * \mathrm{sign}(\mathbf{l}_1^T \mathbf{\Phi}^{\mathbf{r}}(\mathbf{x}_0; t_1, t_0)\delta\mathbf{x}_0)$
Return $\delta\mathbf{x}_0$
```

Algorithm 2: The quadratic eigenvalue algorithm to obtain an initial guess for the passive angles-only relative orbit determination problem.

```
Input: $\mathbf{l}_i$,$\mathbf{x}_0$
Compute $\mathbf{\Phi}^{\mathbf{r}}(\mathbf{x}_0; t_i, t_0)$;
Compute $\mathbf{A}$ from Eq. 5.5;
    Compute the SVD of $\mathbf{A}$;
        $\bar{\mathbf{x}}_0 \leftarrow \mathbf{v}_6(\mathbf{A})$ the sixth right singular vector (unit vector);
        $\bar{\mathbf{x}}_0 \leftarrow \bar{\mathbf{x}}_0 * \mathrm{sign}(\mathbf{l}_1^T \mathbf{\Phi}^{\mathbf{r}}(\mathbf{x}_0; t_1, t_0)\bar{\mathbf{x}}_0)$;
Compute $\mathbf{\Psi}^{\mathbf{r}}(\mathbf{x}_0; t_i, t_0)\bar{\mathbf{x}}_0$        ▷ directly, or with Eq. 5.12
Compute $\mathbf{B}$ from Eq. 5.10;
Compute the eigenvectors and eigenvalues $(\mathbf{y}_i, \lambda_i)$ of the generalized linear
    eigenvalue problem in Eq. A.10;
Calculate the normalized eigenvalues of the quadratic eigenvalue problem
    $(\hat{\mathbf{x}}_i, \lambda_i)$ from Eq. A.11 and A.12;
Select the eigenpair $(\hat{\mathbf{x}}_i, \lambda_i)$ s.t. $i = \mathrm{argmax}_j |\hat{\mathbf{x}}_j \cdot \bar{\mathbf{x}}_0|$;
Let $\delta\mathbf{x}_0 = \mathrm{Re}(-2\lambda_i \hat{\mathbf{x}}_i)$;
$\delta\mathbf{x}_0 \leftarrow \delta\mathbf{x}_0 * \mathrm{sign}(\mathbf{l}_1^T \mathbf{\Phi}^{\mathbf{r}}(\mathbf{x}_0; t_1, t_0)\delta\mathbf{x}_0)$;
Return $\delta\mathbf{x}_0$
```

numbers of observations are presented in Fig. 5.1. Both algorithms take on the order of milliseconds to compute. The two algorithms take roughly the same time to compute, though Alg. 2 based on the quadratic eigenvalue problem approach requires a few more tenths of milliseconds to compute. The time complexity of both algorithms is linear in the number of observations since the singular value decomposition used in both has computational complexity $\mathcal{O}(MN^2 + N^3)$ for a matrix with M rows and N columns, and because $N = 6$ is fixed for the matrix $\mathbf{A}$ regardless of the number of observations [46]. The computational complexity of the eigenvalue computations are independent of the number of observations, since the matrices whose eigenvalues are being found maintain the same dimensions regardless of the number of observations. The constant shift of the two timing curves comes from the fact that Alg. 2 solves an eigenvalue problem that is twice the dimension of the eigenvalue problem solved in Alg. 1.

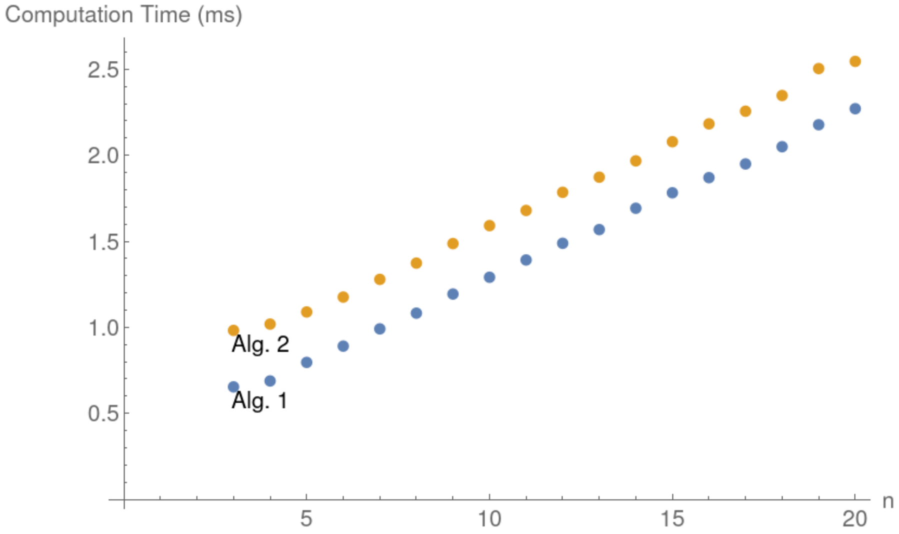

Figure 5.1: Timing results as a function of number of observations.

5.2.3 Solving the Nonlinear Least Squares Problem

With the initial guess for a solution in hand, we employ optimal linear orbit determination (OLOD) to find the final solution [111]. This method can be phrased as Gauss-Newton applied to the problem from Eq. 5.1, and could be extended to a Levenberg-Marquardt algorithm [79, 91], but we make no such attempt here.

5.3 Results

We conducted randomized numerical experiments to test the two scale approximation algorithms presented here. In order to capture a wide variety of relative motion behavior in the vicinity of the chief satellite, we selected initial and terminal points uniformly at random from a cube centered about the chief satellite and solved for the initial velocity to achieve that transfer. This initial state was then propagated forward in time with observations made uniformly spaced in the time interval. The QUEST measurement error model from Eq. 5.2 was then used to perturb the exact observations [110]. Then, two predictions of the scale were made based on Alg. 1 and Alg. 2. We conducted 1000 trials with 10 observations equally spaced over the observation period for each of the following scenarios: no measurement error, $\sigma = 10^{-3}, 10^{-4}$, and 10^{-5} radian level measurement error. Note that $\sigma = 10^{-4}$ rad corresponds to an approximate 1 arc minute 3σ level of error (the capability of a modern commercially available star-tracker) [96].

5.3.1 Geostationary Orbit

In Fig. 5.2, we present test cases with a Geostationary reference orbit propagated with Keplerian dynamics over a 2.3 day time period (chosen to avoid cross-track motion transfer singularities when constructing the test relative orbit). The cube that the deputy satellites end and begin within is centered at the chief satellite with 200km side lengths. The performance of both algorithms is roughly the same for cases with low sensor noise. However, in the $\sigma = 10^{-3}$ rad case, Alg. 2, which solves the true overdetermined eigenvalue problem in a least squares sense, has around half as much scale error as the pseudo-inverse approach, and maintains much lower maximum errors, staying below the actual scale of the relative orbit. With $\sigma < 10^{-4}$ rad, the error in the scale of the predicted orbit is, on average, within about one percent of the true value in all cases tested and always below ten percent.

Further, in the case from Fig. 5.2 with no observation error, optimal linear orbit determination converges in a few iterations to the true solution for all 1000 randomized relative orbits when provided with guesses from either algorithm. In the case where uninformed guesses of the scale were provided to OLOD rather than using either initial guess generating algorithm developed here, guesses below 10 km never converged to the true solution. We examine a stressing case for the relative orbit determination problem with a short observation arc and few measurements. Specifically, test cases are generated in the same manner as Fig. 5.2 but with $\sigma = 10^{-5}$ rad and only three observations over one quarter of an orbit. This corresponds to availability of a sensor with an order of magnitude higher accuracy than modern, commercially available star-trackers, but in a case with minimal observations over a small time window. We use Alg. 1 in red and Alg. 2

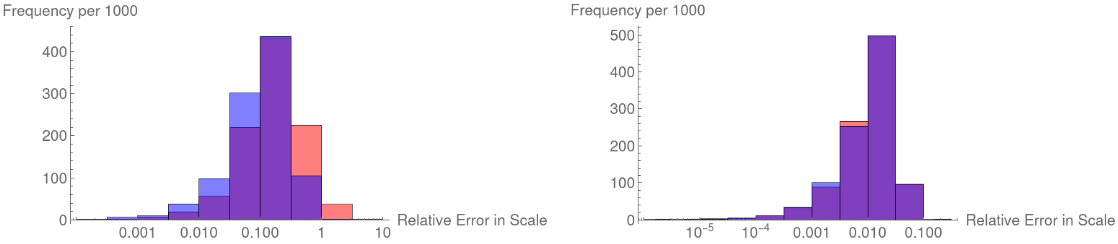

(a) Algorithm 1, 2 estimates $\sigma = 10^{-3}$ rad error.
Geometric mean 0.152, 0.089

(b) Algorithm 1, 2 estimates $\sigma = 10^{-4}$ rad error.
Geometric mean 0.010, 0.011

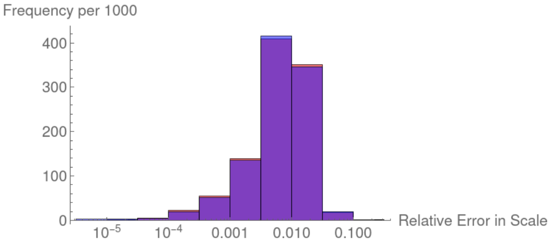

(c) Algorithm 1, 2 estimates $\sigma = 10^{-5}$ rad error.
Geometric mean 0.006, 0.006

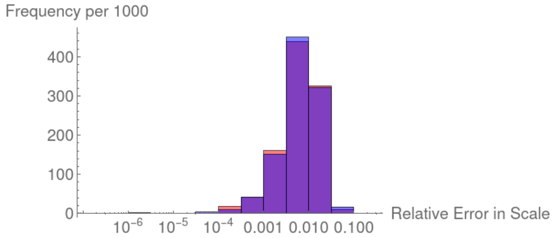

(d) Algorithm 1, 2 estimates no error.
Geometric mean 0.005, 0.005

Figure 5.2: Relative error in scale for 1000 initial relative orbits in a 200km cube centered about the Geostationary reference orbit. Alg. 1 in Red, Alg 2. in Blue.

in blue to provide an initial guess for OLOD. The error in solutions estimated by three iterations of OLOD to convergence under the above circumstances is given in Fig. 5.3. In this case, OLOD improves on the initial estimates from both algorithms below some error threshold, but sends estimates with high error to the trivial or divergent solutions as can be seen from the gap between around 10 percent and 100 percent error. Note that OLOD applied to estimates from Alg. 1 diverged or converged to the trivial solution in around 5 percent of cases tested. The error in solutions converging near the true solution is large in some cases even going above ten percent; however, this likely stems from the observability of the problem and not poor performance of the nonlinear least squares solution procedure as increasing the number of iterations of OLOD does not change the results substantially, indicating convergence to local minima of the nonlinear least squares problem. We will study the covariance of state estimates expected from solving the relative orbit determination problem as a function of observation time and number of observations in Sec. 5.4. However, in the case of OLOD applied to the estimate from Alg. 2, around half of cases tested converged to the trivial solution rather than the true solution. The underperformance of Alg. 2 as compared to Alg. 1 occurs only in cases with very few observations, and the opposite trend is seen in the case of poor quality measurements when many observations are taken as in Fig. 5.2. This seems to point to ill-conditioning of Eq. A.10 in the case where only around three observations are taken. In these cases with low numbers of observations, Alg. 1 is preferable to use. It is also worth noting that without initial guess generation from either algorithm developed here, OLOD will not converge to the true solution in any of the 1000 cases above when an uninformed scale guess of 10 km or lower is provided. This means that the approach of starting OLOD with uninformed guesses of the scale will not ever lead to convergence unless that uninformed guess of the scale is within around an order of magnitude of the true scale. One could perform trials of many magnitudes of the scale guess, and this may be a good fall back in the small number of cases where OLOD converges to the trivial solution given our initial guess algorithms. This approach would fall into a very similar category as an existing method using bisection on scale guesses [6].

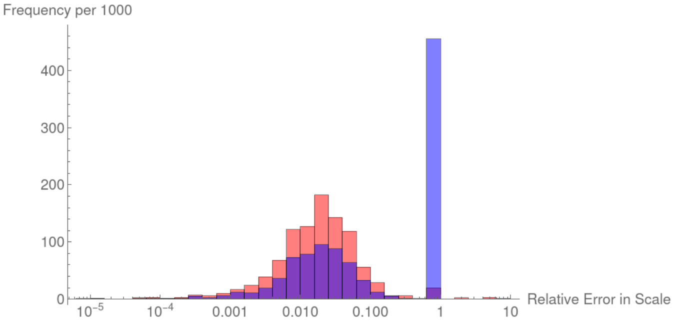

Figure 5.3: Relative error in scale for OLOD applied to relative orbits in the short arc Geostationary case.

5.3.2 Near Rectilinear Halo Orbit

In Fig. 5.4, we present test cases with a Near Rectilinear Halo Orbit (NRHO) reference propagated with Earth-Moon Circular Restricted Three Body Problem dynamics over 0.8 of one orbital period. The cube that the deputy satellites end and begin within is centered at the chief satellite with side lengths that are 2/1000th the scale of the out-of-plane component of the NRHO at apolune (approximately 140 km). The reference orbit used comes from the proposed NASA Gateway orbit [1, 31]. Initial conditions for the orbit are $\mu = 1.0/(81.30059 + 1.0), x_0 = 1.022022, z_0 = -0.182097, \dot{y}_0 = -0.103256$ with other initial coordinates equal to zero. The period of the orbit is 1.511111 nondimensional time units where 2π time units is equivalent to the revolution period of the Earth-Moon system. Again, Alg. 2 demonstrates half the error, on average, in the high sensor noise case, though the two methods are indistinguishable in the lower noise cases. For the $\sigma < 10^{-4}$ rad cases, the scale error is, on average, below two percent and almost always below ten percent. The high sensor noise case ($\sigma = 10^{-3}$ rad) in this NRHO scenario exhibits much higher scale error with either algorithm than for the two-body example presented in Fig. 5.2. This may stem from the sensitivity of dynamics in the three-body system as compared with two-body dynamics.

We examine a stressing case for the NRHO relative orbit determination problem with a short observation arc and few measurements. Again, test cases are generated in the same manner as in Fig. 5.2, but with $\sigma = 10^{-5}$ rad and only three observations over one quarter of an orbit. We use Alg. 1 to provide an initial guess for OLOD. The error in solutions estimated by three iterations of OLOD under the above circumstances is given in Fig. 5.5. Note that OLOD converges to the trivial solution in about 10 percent of cases, and diverges in less than one percent

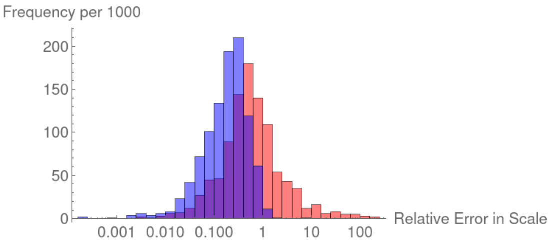

(a) Algorithm 1, 2 estimates $\sigma = 10^{-3}$ rad error.
Geometric mean 0.559, 0.235

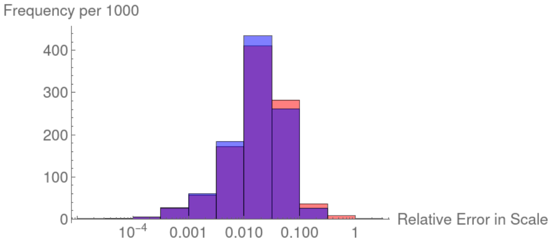

(b) Algorithm 1, 2 estimates $\sigma = 10^{-4}$ rad error.
Geometric mean 0.018, 0.018

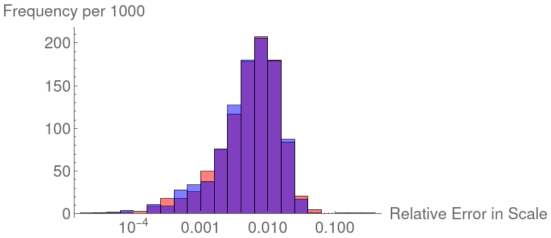

(c) Algorithm 1, 2 estimates $\sigma = 10^{-5}$ rad error.
Geometric mean 0.005, 0.005

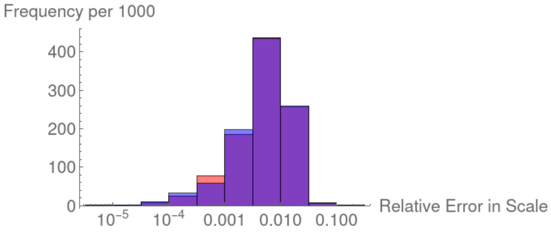

(d) Algorithm 1, 2 estimates no error.
Geometric mean 0.004, 0.004

Figure 5.4: Relative error in scale for 1000 initial relative orbits in a 140 km unit cube centered about the NRHO reference orbit. Alg. 1 in Red, Alg 2. in Blue.

of cases. The cases converging to the trivial solution are represented by the peak at relative error of 1, while divergence is indicated by relative error greater than 1. The performance of OLOD in combination with Alg. 1 for initial guess generation developed here is inferior to that observed in the Geostationary case, but still exhibits convergence to solutions around the true solution in around 90 percent of cases. In general, at shorter distances and with longer observation periods and numbers of observations, convergence around the true solution is more common. The same poor performance of Alg. 2 due to the low number of observations takes place as in the case of Fig. 5.3.

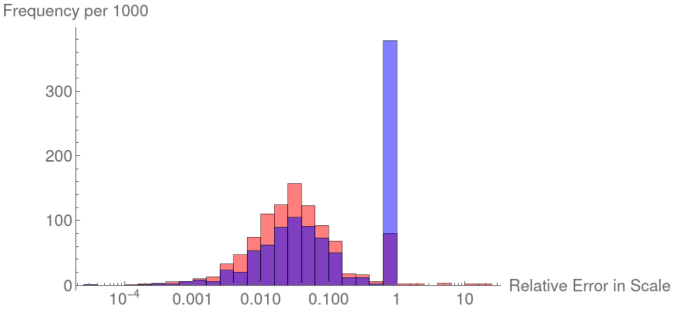

Figure 5.5: Relative error in scale for OLOD applied to relative orbits in the short arc NRHO case.

5.3.3 Choosing an Algorithm

Performance differences in Figs. 5.2, 5.4 indicate that Alg. 2 performs better in terms of error than Alg. 1 in cases where there are many more than three observations and high sensor noise. However, Figs. 5.3, 5.5 indicate that Alg. 2 may be solving an ill-conditioned problem when the number of observations is close to three. This means that for low numbers of observations, Alg. 1 should be preferred. It is also worth noting that for these small numbers of observations, Alg. 1 is about twice as fast to compute as Alg. 2, making it perform overall better in cases with low numbers of observations.

5.4 Covariance Analysis

Covariance studies have been performed before using cylindrical coordinates to assess the error covariance of solutions to relative orbit determination in the two-body problem [43]. To build on this, we offer a formulation in terms of cartesian coordinates, and perform covariance analysis on three-body problem relative orbit determination. Sinclair and Lovell's paper on optimal linear orbit determination provides covariance analysis that applies trivially to our application [111]. To summarize, once OLOD converges to a solution, the solution is unbiased up to first-order, with a covariance described by the position vectors of the observed satellite relative to the observer satellite at the observation times, $\delta\mathbf{r}_i$, as well as the measurement covariance $\boldsymbol{\Sigma}_i$, and the STM blocks $\Phi^{\mathbf{r}}(\mathbf{x}_0 + \delta\mathbf{x}_0; t_i, t_0)$ associated with the solution orbit. Let

$$\mathbf{M} = \sum_i -(\Phi^{\mathbf{r}}(\mathbf{x}_0 + \delta\mathbf{x}_0; t_i, t_0))^T [\mathbf{l}_{t_i}]_\times [\mathbf{l}_{t_i}]_\times \Phi^{\mathbf{r}}(\mathbf{x}_0 + \delta\mathbf{x}_0; t_i, t_0) \tag{5.13}$$

Then, the error covariance for the solution is

$$\mathbf{P} = \mathbf{M}^{-1} \left(\sum_i ||\delta\mathbf{r}_i||^2 (\Phi^{\mathbf{r}}(\mathbf{x}_0 + \delta\mathbf{x}_0; t_i, t_0))^T \boldsymbol{\Sigma}_i \Phi^{\mathbf{r}}(\mathbf{x}_0 + \delta\mathbf{x}_0; t_i, t_0) \right) \mathbf{M}^{-T} \tag{5.14}$$

We can perform studies of the solution covariance of the least squares problem from Eq. 5.1 using Eq. 5.14. By setting up a scenario including the reference orbit for the sensor $\mathbf{x}_0$, the initial relative state of the observed satellite $\delta\mathbf{x}_0$, the number of observations n, and the duration of the observations window Δt, we can evaluate the error covariance in Eq. 5.14. The induced 2-norm of the upper left 3 by 3 block $\mathbf{P}_{\mathbf{r}}$ of the covariance matrix $\mathbf{P}$ provides a good metric for the level of uncertainty in the final solution. In particular, $\|\mathbf{P}_{\mathbf{r}}\|_2$ provides the maximal variance of the solution distribution when marginalized to any one dimensional subspace. Given that the weakly observable part of $\delta\mathbf{x}_0$ is its scale, $\|\mathbf{P}_{\mathbf{r}}\|_2$ is approximately the variance in the estimated initial distance $\|\delta\mathbf{r}_0\|$. We assess the variance in estimated initial distance for various circumstances in a Geostationary orbit and the proposed NASA Gateway Near Rectilinear Halo Orbit.

5.4.1 Geostationary Orbit

The position covariance 2-norm or approximate variance in distance is plotted for a number of different scenarios with a Geostationary observer orbit in Figs. 5.6-5.7, given a $\sigma = 10^{-4}$ rad sensor noise level for all of the following scenarios. In Fig. 5.6, the relationship between number of observations and error covariance is studied with an $e = 0.001$ eccentricity satellite orbit being observed as it circumnavigates the observer orbit over the course of a single period. Observations are equally distributed across the one period observation window. The error variance of the final distance appears to vary inversely with the number of observations, though some nonmonotonicity is observed for small numbers of observations where the times of the uniformly spaced observations change dramatically from each scenario to the next. Also in Fig. 5.6, the number of observations n is fixed at 10, while the observation window is varied from 0 to 3 periods. Large decreases in the error covariance are observed as the observation period increases between 0 and 0.25 periods, as well as around one half of one period. The error covariance varies much less dramatically in the region between 0.25 orbits and 0.4 orbit as well as following 0.6 orbits. In Fig. 5.7 the relative motion geometry is studied. A single period with 10 observations is employed with relative motion geometries of varying size. Each observed satellite is circumnavigating the Geostationary orbit observer (which is assumed to be perfectly circular) with a nonzero eccentricity, but the scale of that eccentricity is varied. The error covariance stays nearly constant though slightly decreases as a function of increasing differences in the eccentricity of the observer and observed satellites. This approximately constant level of range error in the estimated orbit indicates that the range error of a circumnavigating satellite in practically independent of the size of the relative motion geometry. Also in Fig. 5.7, the same number of observations and observing time are used, but with a leader-follower formation geometry with varying offsets in the mean anomaly difference of the two Geostationary satellites. The covariance significantly increases as a function of the spacing of the leader-follower formation. In particular, the increase appears to follow a quadratic curve, indicating that the range error standard deviation increases linearly with the distance from the observer satellite. Between these two trends we can say that the character of the relative motion (being oscillatory as a result of differences in the eccentricity of the two satellites or being static in a leader-follower geometry) has a bearing on the behavior of the error in the estimated range as a function of the true range/size of the relative motion. Non-oscillatory motion leads to linear increases in the range error as the offset between the two satellites increases, while oscillatory motion leads to a largely constant level of error regardless of the actual size of that relative geometry.

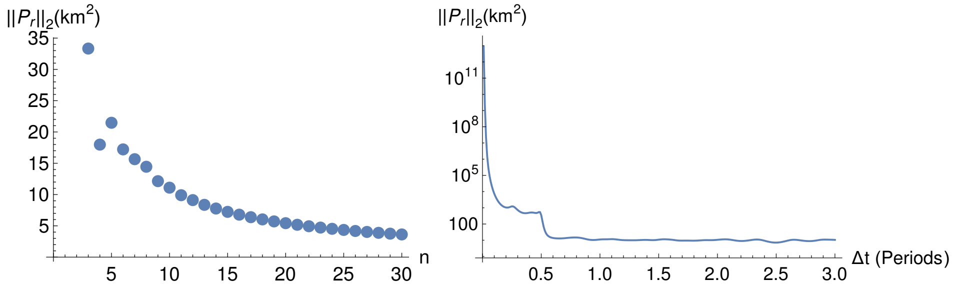

Figure 5.6: The variance in estimated distance as a function of number of observations and observation time in the Geostationary orbit.

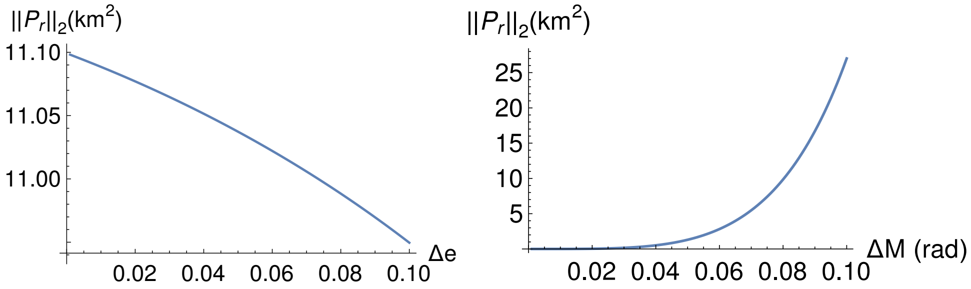

Figure 5.7: The solution covariance norm as a function of the relative eccentricity of the two orbits and the leader-follower mean anomaly difference respectively in the Geostationary orbit.

5.4.2 Near Rectilinear Halo Orbit

We experimented with the error covariance of solutions in the same manner as before with the Geostationary orbit but with the Gateway NRHO as an observer orbit instead. Just as for the Geostationary analysis, sensor noise is set to $\sigma = 10^{-4}$ rad. For the initial conditions of the relative motion, a unit vector given in canonical units as $(-0.361, 0, -0.136, 0, 0.922, 0)$ in the center eigenspace of the monodromy matrix associated with the sensor orbit NRHO is used. We choose a relative orbit approximately in the center manifold of the reference orbit as an example of a meaningful relative motion that ensures boundedness over the observation window. This initial relative state vector is scaled so that the initial relative distance is one kilometer. In Fig. 5.8, a quarter period of the NRHO is used for the observation window, and the number of observations is varied. The resulting trend is a decrease in the error covariance as the number of observations increases. However, this decrease in the error covariance is slower than in the Geostationary case for high values of n. In the study of the observing duration, the same relative orbit geometry is used. Ten observations are employed while the observation window duration is varied. A very similar structure is revealed as in the Geostationary case from Fig. 5.6, where diminishing returns are observed over time, with flat areas between one tenth of an orbit to around a quarter of an orbit, as well as past a little over half an orbit. Finally, Fig. 5.9 takes the same ten observations over a quarter period of observation of the same relative motion geometry scaled between 1 km and 10 km initial distance. Increasing the separation between the observer and the observed satellites increases the error covariance. Similar to the case of a leader-follower orbit in the two-body problem, this scenario also exhibits what appears to be linear growth of the error standard deviation as the range of the orbit increases. To summarize, in the case of the

NRHO and the Geostationary orbit, the variance in scale tends to increase with distance of the relative orbit, decrease steadily but with diminishing returns as the number of observations increases, and decrease very quickly as overall observation time increases within the first half period, but exhibits diminishing returns after that point.

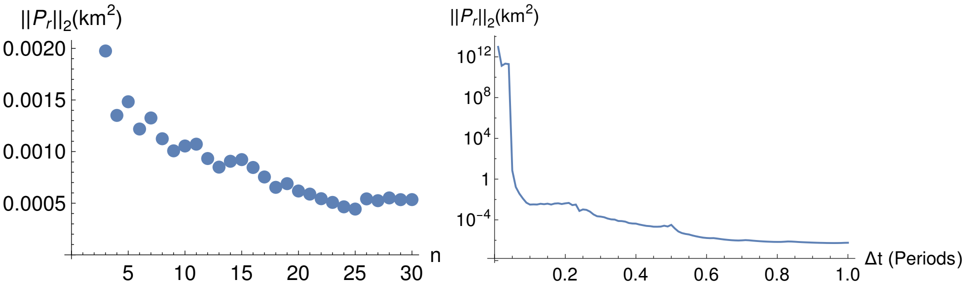

Figure 5.8: The variance in estimated distance as a function of number of observations and observation time in the NRHO.

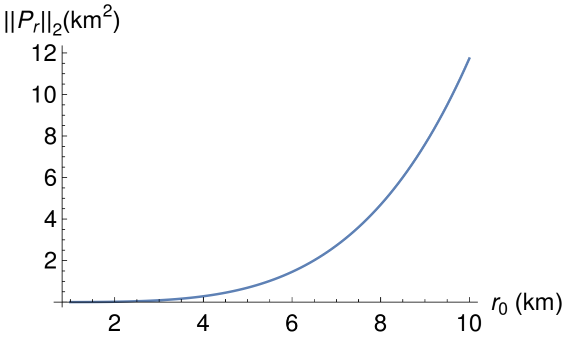

Figure 5.9: The solution covariance norm as a function of the initial relative distance of the two orbits in the NRHO.

5.5 Conclusion

We have presented two algorithms for solving the passive angles-only relative orbit determination problem using an eigenvalue problem approach. Throughout this whole process we have only employed standard linear algebraic operations that are fast and widely implemented. By framing the solution with the state transition tensor model of dynamics, we have abstracted to the point where we may employ any dynamics model as long as we can numerically calculate the state transition tensors associated with those dynamics. In particular, this yields the first algorithm, to our knowledge, for solving the passive angles-only relative orbit determination problem under three-body dynamics without camera offsets or multiple cameras. An open question is how performance is degraded when state transition tensors from a lower fidelity model are used to fit observations coming from an underlying higher fidelity model of the dynamics, or when the state transition tensors of a nearby reference orbit are used due to estimation error of the reference orbit state. Additionally, the use of state transition tensors gives rise to an inherently local approximation of the dynamics, making this method unsuitable for large distance scales between satellites over which the third and higher-order dynamics play a significant role in the relative dynamics. However, we have shown that this methodology is appropriate at least as far out as 200km separation distances for satellites near Geosynchronous orbit for example. Even with these limitations and remaining questions, the algorithms presented here offer promising accuracy, robustness to noise, flexibility in the number of measurements, high computational efficiency, and easy implementation. This methodology may enable future onboard angles-only relative navigation for satellites with limited sensing, maneuvering, and computational capabilities within Earth orbit and additionally opens the door to angles-only relative orbit determination for cislunar applications such as the proposed NASA Gateway program.

CHAPTER 6

ERROR QUANTIFICATION OF LINEAR AND HIGHER-ORDER GUIDANCE, NAVIGATION, AND CONTROL METHODS

6.1 Introduction

Methods relying on linearization are widespread in the fields of control and estimation due to their efficiency as well as ease of implementation and analysis. In particular, resource constrained embedded systems such as those on satellites often necessitate the efficiency of linear algorithms for onboard guidance and navigation tasks. In this work, we focus on two applications: calculating rendezvous or stationkeeping guidance using state transition matrices[24, 93], as well as the measurement update of the extended Kalman filter with an optical measurement [106]. We present a method for approximating the maximum possible error when using some of these linear algorithms when the true function or dynamical system is nonlinear. Error estimates are expressed as a function of the scale of deviations from some nominal or reference values used in the linearization.

In relation to this idea about the error performance of linear algorithms, there has been much interest in the last few decades in quantifying the level of nonlinearity of a function such as the flow of a dynamical system. Measuring the nonlinearity of the flow of a dynamical system makes it possible to compare coordinate systems and choose the coordinate system with the best linear approximation before applying a linear control or estimation algorithm [57, 58, 54]. Similarly, measures of nonlinearity and other related information about directions of maximal nonlinearity can aid development of semi-analytical algorithms that split the domain or employ Gaussian mixtures to improve linearization behavior for each split [84, 124].

We present a number of nonlinearity indices that can be computed in terms of tensor norms, including a scale-free generalization of the original nonlinearity index that is easy to compute using the induced 2-norm of a matrix. Additionally, we develop an easier to implement approach for computing the recently developed nonlinearity index Tensor Eigenpair Measure of Nonlinearity (TEMoN) [54] that requires lower-order tensors as compared with the existing approach and only a very simple power iteration like algorithm. Finally, we develop a novel measure of nonlinearity that we call D-Eigenvalue Measure of Nonlinearity (DEMoN).

We approach the problems described above by extending the formalism of induced or operator norms from matrices to multilinear operators or tensors. This allows us to treat a number of existing algorithms in the literature as well as other possible algorithms in terms of a single unified framework. In particular, this includes the tensor eigenvalue approach [54, 55], the polynomial bounding scheme on a hypercube [84], and the maximum change in the Frobenius norm of the first-order derivative approach [124]. We define an induced tensor norm and present a number of examples in addition to these three. Much of the focus of this paper is on the induced tensor 2-norm, which relies on tensor Z-eigenvalues for computation, as well as the induced tensor $(2, \mathbf{D})$-norm which relies on a generalization known as a tensor D-eigenvalue [100]. We began by summarizing a number of tensors that arise in guidance, navigation, and control in Sec. 1.2. Now, we build up from vector to tensor norms, describing their computation in Sec. 6.2, and finally apply tensor norms to the bounding of error in guidance (Sec. 6.3.1) and estimation (Sec. 6.3.2) contexts, as well as in nonlinearity index computations (Sec. 6.3.3).

6.2 Norms of Tensors

A norm $\|\cdot\|$ on a vector space $\mathcal{X}$ is defined as a function from the vector space to the real numbers that satisfies three properties: the triangle inequality $\|\mathbf{x}+\mathbf{y}\| \leq \|\mathbf{x}\| + \|\mathbf{y}\|$ for all $\mathbf{x}, \mathbf{y} \in \mathcal{X}$, absolute homogeneity with scalars $\|a\mathbf{x}\| = |a|\|\mathbf{x}\|$ for all scalars a and all vectors $\mathbf{x} \in \mathcal{X}$, and finally positive definiteness $\|\mathbf{x}\| = 0$ if and only if $\mathbf{x} = 0$ is the zero element of the vector space $\mathcal{X}$. Note that tensors of a given order and dimension along each index form a vector space. This includes Euclidean vectors, matrices, as well as higher-order tensors. We present a variety of norms of Euclidean vector spaces, as well as on the vector spaces associated with matrices and higher-order tensors, building up from simpler to more complex.

6.2.1 Vector Norms

The norm of a vector quantifies some notion of the size of that vector. We review a number of useful vector norms here. First, the p-norms of a vector $\mathbf{v} \in \mathbb{R}^n$ are defined for $p \geq 1$ as

$$\|\mathbf{v}\|_p = \left(\sum_{i=1}^{n} |v_i|^p\right)^{1/p} \tag{6.1}$$

and the ∞-norm is defined as

$$\|\mathbf{v}\|_\infty = \max_{i=1\ldots n} |v_i| \tag{6.2}$$

The 2-norm is independent of the choice of coordinates for a vector unlike all of the other p-norms. A vector norm can also be induced by a symmetric positive definite matrix $\mathbf{D}$ using a quadratic form:

$$\|\mathbf{v}\|_{\mathbf{D}} = \mathbf{v}^T \mathbf{D} \mathbf{v} \tag{6.3}$$

The 2-norm of a vector is one such norm where $\mathbf{D} = \mathbf{I}_n$.

6.2.2 Frobenius Norm

The Frobenius norm of a tensor is easily computable and is equivalent to any other finite dimensional norm (bounded in both directions by potentially dimension dependent constant multiples of the other norm) [46]. The Frobenius norm of an (l, m)-tensor under the Euclidean metric is the square root of the sum of the squared entries:

$$\|\mathbf{B}\|_F^2 = B^{i_1 \ldots i_l}_{j_1 \ldots j_m} \delta_{i_1, i'_1} \ldots \delta_{i_l, i'_l} \delta^{j_1, j'_1} \ldots \delta^{j_l, j'_l} B^{i'_1 \ldots i'_l}_{j'_1 \ldots j'_m} \tag{6.4}$$

where $\delta^{i,j}$ with superscripts denotes the Euclidean inverse metric tensor given again by the Kronecker delta but expressed as a contravariant instead of covariant tensor. In general, the Frobenius norm of any tensor is the 2-norm of the tensor flattened into a vector in any order.

6.2.3 Induced/Operator Norms

These vector and Frobenius norms, among others, can be used to define other norms. The induced or operator norm subordinate to the a and b norms, or (a, b)-norm of a matrix $\mathbf{A} \in \mathbb{R}^{m,n}$ is defined as

$$\|\mathbf{A}\|_b^a = \max_{\mathbf{x} \neq \mathbf{0}} \frac{\|\mathbf{A}\mathbf{x}\|_a}{\|\mathbf{x}\|_b} = \max_{\|\mathbf{x}\|_b = 1} \|\mathbf{A}\mathbf{x}\|_a \tag{6.5}$$

where the a-norm and b-norm conform to the dimensions of $\mathbf{A}$ and $\mathbf{x} \in \mathbb{R}^n$ [46]. We may extend this definition of an operator norm to tensors. Let $\mathbf{B}$ be a $(1, m)$-tensor such that the tensor is partially symmetric along the covariant indices. Let the a-norm on the output space be defined for a $(1, m_o)$-tensor, and the b-norm be some vector norm on the input space. Then the induced norm of a tensor is:

$$\|\mathbf{B}\|_b^a = \max_{\mathbf{x} \neq \mathbf{0}} \frac{\|\mathbf{B}\mathbf{x}^{m-m_o}\|_a}{\|\mathbf{x}\|_b^{m-m_o}} = \max_{\|\mathbf{x}\|_b = 1} \|\mathbf{B}\mathbf{x}^{m-m_o}\|_a \tag{6.6}$$

where

$$\left(\mathbf{B}\mathbf{x}^{m-m_o}\right)^i_{j_1,\ldots j_{m_o}} = B^i_{j_1\ldots j_m} x^{j_{m_o+1}} \ldots x^{j_m} \tag{6.7}$$

When a, b are both vector norms as is usually the case, $m_o = 0$ and the induced tensor norm is defined:

$$\|\mathbf{B}\|^a_b = \max_{\mathbf{x}\neq\mathbf{0}} \frac{\|\mathbf{B}\mathbf{x}^m\|_a}{\|\mathbf{x}\|^m_b} = \max_{\|\mathbf{x}\|_b=1} \|\mathbf{B}\mathbf{x}^m\|_a \tag{6.8}$$

An example where m_o is not zero is the induced (Frobenius, 2)-norm, where the a norm is the Frobenius norm on a $(1,1)$-tensor. See Sec. 6.2.7 for details.

6.2.4 2-norm

The induced 2-norm of a $(1, m)$-tensor $\mathbf{B}$ is perhaps the most natural to consider given that it relies only on a single basic vector norm for its definition and it is unitarily invariant so the norm is invariant under rotations of the coordinates. We can compute the 2-norm of a tensor by examining the eigenvalues of the "square" of the tensor. Again, given the metric tensor for Euclidean space $g_{i,j} = \delta_{i,j}$ which is the Kronecker delta, we define the $(0, 2m)$-tensor "square," $\tilde{\mathbf{B}}$:

$$\tilde{B}_{i_1,..,i_m,j_1,\ldots,j_m} = B^{\alpha}_{i_1,..,i_m} \delta_{\alpha,\beta} B^{\beta}_{j_1,..,j_m} \tag{6.9}$$

This square of the tensor gives the squared 2-norm of the output of the original tensor when applied to a vector ($2m$ times):

$$\tilde{\mathbf{B}}\mathbf{x}^{2m} = \|\mathbf{B}\mathbf{x}^m\|^2_2 \tag{6.10}$$

For every covariant tensor such as $\tilde{\mathbf{B}}$, there exists a symmetric tensor $\hat{\mathbf{B}}$ with the same output under repeated contraction with a single vector. That is, $\hat{\mathbf{B}}$ exists such that for any $\mathbf{x} \in \mathbf{R}^n$,

$$\hat{\mathbf{B}}\mathbf{x}^{2m} = \tilde{\mathbf{B}}\mathbf{x}^{2m} \tag{6.11}$$

and

$$\hat{B}_{i_1,\ldots,i_m,j_1,\ldots,j_m} = \hat{B}_{\sigma(i_1,\ldots,i_m,j_1,\ldots,j_m)} \tag{6.12}$$

for any permutation σ of the indices. The symmetrization is equal to the mean of the tensor under all permutations:

$$\hat{B}_{i_1,\ldots,i_m,j_1,\ldots,j_m} = \frac{1}{(2m)!} \sum_{\sigma \in S_{2m}} \tilde{B}_{\sigma(i_1,\ldots,i_m,j_1,\ldots,j_m)}. \tag{6.13}$$

where S_{2m} is the permutation group of order $2m$. Another more computationally efficient method for symmetrization appears in the MATLAB Tensor Toolbox [67], though as we will demonstrate, explicit calculation of the symmetrized tensor is rarely necessary or desirable. Finally, having obtained a symmetric positive semi-definite tensor ($\mathbf{B}\mathbf{x}^{2m} \geq 0$ for all $\mathbf{x} \in \mathbb{R}^n$), the maximum of the following constrained optimization problem can be obtained as the largest Z-eigenvalue of the tensor [82]:

$$\lambda_{\max}(\hat{\mathbf{B}}) = \max_{\|\mathbf{x}\|_2 = 1} \hat{\mathbf{B}}\mathbf{x}^{2m} \tag{6.14}$$

where a Z-eigenvalue satisfies the equation

$$\hat{\mathbf{B}}\mathbf{x}^{2m-1} = \lambda \mathbf{x}, \quad \|\mathbf{x}\|_2 = 1 \tag{6.15}$$

More generally, any of the Z-eigenvectors of $\hat{\mathbf{B}}$ satisfy the Karush–Kuhn–Tucker (KKT) conditions and are constrained stationary points for the objective function $\hat{\mathbf{B}}\mathbf{x}^{2m}$ when $\mathbf{x}$ is constrained to the unit sphere [82]. Thus, the induced 2-norm of the tensor $\mathbf{B}$ is defined as the square root of the maximum Z-eigenvalue of the corresponding symmetrized square tensor $\hat{\mathbf{B}}$

$$\|\mathbf{B}\|_2 = \sqrt{\lambda_{\max}(\hat{\mathbf{B}})}. \tag{6.16}$$

This is a generalization of the idea that the induced 2-norm of a matrix is given by the largest singular value (square root of the largest eigenvalue of the square of the matrix). The maximum eigenvalue of an even-order symmetric tensor that is convex over the unit ball can be calculated by a higher-order generalization of power iteration [32, 68, 66].

$$\mathbf{x}_{n+1} = \frac{\hat{\mathbf{B}}\mathbf{x}_n^{2m-1}}{\|\hat{\mathbf{B}}\mathbf{x}_n^{2m-1}\|_2} \tag{6.17}$$

Having obtained the desired eigenvector, the corresponding eigenvalue is given by the magnitude of the numerator of Eq. 6.17, or $\|\mathbf{B}\|_2$ can be computed directly by taking

$$\|\mathbf{B}\|_2 = \|\mathbf{B}(\mathbf{x}^*)^m\|_2 \tag{6.18}$$

where $\mathbf{x}^*$ is the Z-eigenvector that power iteration has converged to. Since $\hat{\mathbf{B}}$ is positive semi-definite, even order, and fully symmetric, the symmetric higher-order power iteration method is globally convergent meaning it is guaranteed to converge to some eigenvector regardless of the starting guess $\mathbf{x}_0$. Typically, the eigenvector that is converged to corresponds to a large eigenvalue [66]. This means that generally, an educated guess must be supplied for the initial iterate (like the dominant right singular vector of the state transition matrix in the case of a higher-order state transition tensor [15]) or multiple random initial guesses should be employed when trying to find the eigenvector associated with the largest eigenvalue. The number of random guesses needed to find the global maximum depends on the gap between the largest and second largest eigenvalue since the size of each basin of convergence varies with the size of the eigenvalue. Thus, when two eigenvalues are close to being the dominant eigenvalue, one might need tens to hundreds instead of a couple initial random guesses to reliably find the dominant eigenvector [68] In other contexts for more general tensors, symmetric higher-order power iteration does not have global convergence guarantees, and shifted symmetric higher-order power iteration must be employed [68]. While symmetric higher-order power iteration requires a fully symmetric tensor such as $\hat{\mathbf{B}}$ to converge properly to an eigenvector, the partially symmetric structure of $\mathbf{B}$ and $\tilde{\mathbf{B}}$ enable us to perform symmetric higher-order power iteration on $\hat{\mathbf{B}}$ in Eq. 6.17 without ever needing to perform the symmetrization to form $\hat{\mathbf{B}}$. Further performance optimizations are also possible by directly using the $\mathbf{B}$ tensor directly in calculations rather than its square. We refer to Appendix B.1 for further details.

6.2.5 $(2, \mathbf{D})$-norm

The notion of a D-eigenvalue was introduced as a generalization to the normalization in the definition of Z-eigenvalues for use in higher-order statistics [100]. A D-eigenvalue of the tensor $\hat{\mathbf{B}}$ satisfies the equation

$$\hat{\mathbf{B}}\mathbf{x}^{2m-1} = \lambda \mathbf{D}\mathbf{x}, \quad \|\mathbf{x}\|_{\mathbf{D}} = 1 \tag{6.19}$$

where $\mathbf{D}$ is a symmetric positive definite matrix and the constraint enforces that eigenvectors lie on the ellipsoid given by the quadratic form induced by $\mathbf{D}$ rather than on the unit sphere as is the case with a Z-eigenvalue. All D-eigenvectors of $\hat{\mathbf{B}}$ satisfy the Karush–Kuhn–Tucker (KKT) conditions for the objective function $\hat{\mathbf{B}}\mathbf{x}^{2m}$ when $\mathbf{x}$ is constrained to the $\mathbf{D}$-ellipsoid of points satisfying the constraint in Eq. 6.19. Generalized eigenproblem adaptive power method (GEAP) may be used to solve D-eigenvalue problems [69]. However, since we are only interested in the largest eigenpair, we propose another simple and fast extension of symmetric higher-order power iteration which is usable because the tensors involved are convex multilinear operators over the unit ball. We are interested in the largest D-eigenpair in order to solve the problem

$$\max_{\mathbf{x}^T\mathbf{D}\mathbf{x}=1} \hat{\mathbf{B}}\mathbf{x}^{2m} \tag{6.20}$$

This problem can be changed into a Z-eigenvalue problem with the change of variables

$$\mathbf{y} = \mathbf{D}^{1/2}\mathbf{x} \tag{6.21}$$

where $\mathbf{D}^{1/2}$ is a matrix square root of the matrix $\mathbf{D}$ such as the Cholesky factor. That is

$$\mathbf{D} = \left(\mathbf{D}^{1/2}\right)^T \mathbf{D}^{1/2} \tag{6.22}$$

Making this substitution, the optimization problem becomes

$$\max_{\mathbf{y}^T\mathbf{y}=1} \hat{\mathbf{B}}(\mathbf{D}^{-1/2}\mathbf{y})^{2m} \tag{6.23}$$

where $\mathbf{D}^{-1/2}$ denotes the inverse of the matrix square root of $\mathbf{D}$. This constrained optimization leads to the Z-eigenvalue problem associated with the tensor

$$\left(\hat{B}_{\mathbf{D}}\right)_{i_1 \ldots i_{2m}} = \hat{B}_{j_1 \ldots j_{2m}} \left(\mathbf{D}^{-1/2}\right)^{j_1}_{i_1} \ldots \left(\mathbf{D}^{-1/2}\right)^{j_{2m}}_{i_{2m}} \tag{6.24}$$

If $(\mathbf{v}_{\mathbf{D}}, \lambda_{\mathbf{D}})$ is a Z-eigenpair of $\hat{\mathbf{B}}_{\mathbf{D}}$, then the D-eigenpair associated with $(\hat{\mathbf{B}}, \mathbf{D})$ from Eq. 6.19 is given by the inverse coordinate change

$$(\mathbf{v}, \lambda) = \left(\mathbf{D}^{-1/2}\mathbf{v}_{\mathbf{D}}, \lambda_{\mathbf{D}}\right) \tag{6.25}$$

since

$$\lambda = \lambda_{\mathbf{D}} = \frac{\hat{\mathbf{B}}\mathbf{v}^{2m}}{\|\mathbf{v}\|^2_{\mathbf{D}}} = \hat{\mathbf{B}}\mathbf{v}^{2m} \tag{6.26}$$

Note that this correspondence implies that the largest Z-eigenvalue corresponds to the largest D-eienvalue, and to find the largest D-eigenvalue, one can find the largest Z-eigenvalue of the associated problem. The $(2, \mathbf{D})$-norm of $\mathbf{B}$ is given in terms of the D-eigenvalue of the square of the tensor $\mathbf{B}$ as

$$\|\mathbf{B}\|_{\mathbf{D}}^{[2]} = \sqrt{\lambda_{\max}(\hat{\mathbf{B}}, \mathbf{D})} = \sqrt{\lambda_{\max}(\hat{\mathbf{B}}_{\mathbf{D}})} \tag{6.27}$$

where the superscript "[2]" in the above expression is not a square of the norm, but indicates the type of norm (a $(2, \mathbf{D})$-norm). Rather than explicitly forming the tensor $\hat{\mathbf{B}}_{\mathbf{D}}$ and finding the Z-eigenpairs using symmetric higher-order power iteration, a similar procedure to that proposed in Sec. B.1 can be used after precomputing the Cholesky decomposition of $\mathbf{D}$ a single time prior to iteration. This algorithm takes only a few more operations than solving for the tensor 2-norm, with one computation of the Cholesky decomposition of a matrix prior to iteration (an $\mathcal{O}(n^3)$ operation), and one additional forward substitution and another backwards substitution to solve a lower and upper triangular linear system at each iteration (each taking only $\mathcal{O}(n^2)$ operations where n is the dimension of the vector $\mathbf{x}$). To put this in perspective, one iteration of higher order power iteration on a covariant order $(2m)$-tensor naively takes $\mathcal{O}(n^{2m})$ or $\mathcal{O}(n^{m+1})$ when the tensor arises as the square of some partially symmetric $(1, m)$-tensor and the calculation is performed according to Appendix B.1. This implies that computing a D-eigenvalue is negligibly slower than computing a Z-eigenvalue. Details can be found in Appendix Sec. B.2.

6.2.6 $(\infty, 2)$-norm

In addition to the 2-norm, the induced $(\infty, 2)$-norms of both the matrix $\mathbf{A}$ and the (1, 2)-tensor $\mathbf{B}$ have analytical forms that are readily computable with standard linear algebra tools. The intuition for this development comes from viewing a tensor that is partially symmetric in the covariant indices (such as the second-order state transition tensor) as a vector of symmetric bilinear forms. The (∞, 2)-norm of a matrix is well-known.

$$\begin{aligned} \|\mathbf{A}\|_2^\infty &= \max_{\|\mathbf{x}\|_2=1} \|\mathbf{A}\mathbf{x}\|_\infty \\ &= \max_i \max_{\|\mathbf{x}\|_2=1} A^i_j \mathbf{x}^j \qquad (6.28) \\ &= \max_i \|\mathbf{A}^i\|_2 \end{aligned}$$

To our knowledge, the computation of the (∞, 2)-norm for a $(1, 2)$-tensor that is symmetric along the covariant indices is a novel presentation:

$$\begin{aligned} \|\mathbf{B}\|_2^\infty &= \max_{\|\mathbf{x}\|_2=1} \|\mathbf{B}\mathbf{x}^2\|_\infty \\ &= \max_i \max_{\|\mathbf{x}\|_2=1} \left| B^i_{j,k} \mathbf{x}^j \mathbf{x}^k \right| \qquad (6.29) \\ &= \max_i \sigma_1(\mathbf{B}^i) \qquad (6.30) \end{aligned}$$

where $\mathbf{A}^i$ denotes the ith row vector of the matrix $\mathbf{A}$, and $\sigma_1(\mathbf{B}^i)$ denotes the largest singular value of the covariant matrix $\mathbf{B}^i$ with entries such that $(\mathbf{B}^i)_{j,k} = B^i_{j,k}$. This appears as a result of the well-known identity that the maximum value of a symmetric bilinear form on the 2-norm unit ball is the largest absolute eigenvalue (also the largest singular value) of the matrix defining the bilinear form [46]. When computing the $(\infty, 2)$-norm, a solver should be used that is specifically designed to take advantage of the structure of the symmetric eigenvalue problem. We note that the $(\infty, 2)$-norm, along with other popular induced norms for a matrix, can be found throughout the linear algebra literature [34, 80].

6.2.7 (Frobenius, 2)-norm

The induced (Frobenius, 2)-norm comes from interpreting the $(1, 2)$-tensor as operating on a vector to produce matrices. As we discuss in following sections about nonlinearity indices, this norm can be employed to quantify the change in the Jacobian as the reference point it is evaluated at changes. For example, this norm applied to the second-order state transition tensor quantifies the changes to the state transition matrix as the initial reference state varies. The (Frobenius, 2)-norm is defined

$$\|\mathbf{B}\|_2^F = \max_{\|\mathbf{x}\|_2=1} \|\mathbf{Bx}\|_F \tag{6.31}$$

This norm may be computed by flattening the tensor to the n^2 by n matrix

$$\overline{B}_k^{ni+j} = B^i_{j,k} \tag{6.32}$$

Then the desired norm is given by the induced 2-norm of the matrix resulting from this unfolding:

$$\|\mathbf{B}\|_2^F = \|\overline{\mathbf{B}}\|_2 \tag{6.33}$$

This norm is also unitarily invariant like the 2-norm. Another equivalent method to compute the (Frobenius, 2)-norm is through an eigendecomposition in the following manner derived in the context of Gaussian mixture splitting [124]. Note that

$$\begin{aligned} \|\mathbf{Bx}\|_F^2 &= B^{i_1}_{j_1,k_1} x^{k_1} \delta_{i_1,i_2} \delta^{j_1,j_2} B^{i_2}_{j_2,k_2} x^{k_2} && (6.34) \\ &= B'_{k_1,k_2} x^{k_1} x^{k_2} && (6.35) \end{aligned}$$

where we define

$$B'_{k_1,k_2} = B^{i_1}_{j_1,k_1} \delta_{i_1,i_2} \delta^{j_1,j_2} B^{i_2}_{j_2,k_2} \tag{6.36}$$

Ignoring covariance and contravariance of the indices of the matrix $\mathbf{B}'$ we obtain an expression more similar to that derived in [124] without the tensor formalism

$$\mathbf{B}' = \sum_i (\mathbf{B}^i)^T \mathbf{B}^i \tag{6.37}$$

where $\mathbf{B}^i$ is the matrix given by fixing the contravariant index i and leaving the two covariant indices free. Then we can express the (Frobenius, 2)-norm as the maximum eigenvalue associated with $\mathbf{B}'$:

$$\|\mathbf{B}\|_2^F = \lambda_{\max}(\mathbf{B}') \tag{6.38}$$

The eigenvectors associated with $\mathbf{B}'$ and equivalently the right singular vectors associated with $\bar{\mathbf{B}}$ are all orthogonal with respect to one another. These offer directions along which the Frobenius norm is at a constrained stationary point. The (Frobenius, $\mathbf{D}$)-norm generalizes the (Frobenius, 2)-norm along the same lines in which the $(2, \mathbf{D})$-norm generalizes the 2-norm, though we do not present details here for space.

6.2.8 Upper Bound on the 2-norm

By unfolding the tensor along another axis to preserve the first dimension instead of the last dimension, we can arrive at an upper bound on the induced 2-norm of a tensor [81]. This bound on the induced 2-norm may be computed by flattening the tensor to an n by n^{m-1} matrix. For a $(1, 2)$-tensor, for example, the flattened tensor becomes

$$\underline{B}^i_{nj+k} = B^i_{j,k} \tag{6.39}$$

And tensor contraction becomes equivalent to multiplication with a flattened n^2 dimensional vector coming from the outer product of $\mathbf{x}$ with itself

$$\underline{B}\mathrm{vec}(\mathbf{x}\mathbf{x}^T) = B\mathbf{x}^2 \tag{6.40}$$

where

$$(\mathrm{vec}(\mathbf{x}\mathbf{x}^T))^{(nj+k)} = (\mathbf{x}\mathbf{x}^T)^{j,k} = x^j x^k \tag{6.41}$$

With this relationship, we can show that if the true unit vector satsifying the constrained optimization for the induced 2-norm of a $(1, 2)$-tensor is denoted

$$\mathbf{x}^* = \arg\max_{\|\mathbf{x}\|_2=1} \|\mathbf{B}\mathbf{x}^2\|_2 \tag{6.42}$$

then, the inequality

$$\|\underline{\mathbf{B}}\|_2 \geq \|\underline{\mathbf{B}}\mathrm{vec}(\mathbf{x}^*(\mathbf{x}^*)^T)\|_2 = \|\mathbf{B}(\mathbf{x}^*)^2\|_2 \tag{6.43}$$

follows from the definition of the induced 2-norm of a matrix (the norm of the matrix is at least as large as the norm of the matrix operating on any single unit vector) and the fact that the vector being operated on in the above inequality is a unit vector

$$\|\mathbf{x}\|_2 = 1 \implies \|\mathrm{vec}(\mathbf{x}\mathbf{x}^T)\|_2 = 1 \tag{6.44}$$

The implication in Eq. 6.44 can be proved from the following observation

$$\|\mathbf{x}\mathbf{x}^T\|_F^2 = \|\mathrm{vec}(\mathbf{x}\mathbf{x}^T)\|_2^2 = \sum_{i=1}^{n}\sum_{j=1}^{n}(x^i)^2(x^j)^2 = \left(\sum_{i=1}^{n}(x^i)^2\right)\left(\sum_{j=1}^{n}(x^j)^2\right) = \|\mathbf{x}\|_2^4 \tag{6.45}$$

These arguments boil down to the observation that the unit ball/sphere for vectors in n dimensions mapped into n^2 dimensions by $\mathbf{x} \rightarrow \mathrm{vec}(\mathbf{x}\mathbf{x}^T)$ is a subset of the unit ball/sphere in n^2 dimensions. This upper bound on the 2-norm is also a norm itself. Each necessary property in the definition of a norm follows from the related property of the matrix 2-norm of the flattened tensor.

6.2.9 Upper Bound on the (Frobenius, ∞)-norm

Another induced norm that comes from interpreting a $(1, 2)$-tensor as operating on a vector to produce matrices is the (Frobenius, ∞)-norm.

$$\|\mathbf{B}\|_{\infty}^{F} = \max_{\|\mathbf{x}\|_{\infty}=1} \|\mathbf{B}\mathbf{x}\|_{F} \tag{6.46}$$

$$\tag{6.47}$$

While a convenient method to calculate this norm is not immediately apparent, an upper bound can be obtained very efficiently. A nonlinearity index using this bound on the (Frobenius, ∞)-norm of the second-order state transition tensor was introduced for automatic domain splitting using differential algebra [84]. Given a $(1, 2)$-tensor $\mathbf{B}$, define the matrix $\mathbf{B}^{\infty}$

$$(\mathbf{B}^{\infty})^{i}_{j} = \sum_{k} |B^{i}_{j,k}| \tag{6.48}$$

Then the induced (Frobenius, ∞)-norm of $\mathbf{B}$ is bounded above by the Frobenius norm of the resulting matrix

$$\left(\sum_{i} \sum_{j} \left(\sum_{k} |B^{i}_{j,k}| \right)^{2} \right)^{1/2} = \|\mathbf{B}^{\infty}\|_{F} \geq \|\mathbf{B}\|_{\infty}^{F} \tag{6.49}$$

Note that the original reference uses the subscript 2 on a norm of a matrix to indicate the Frobenius norm and not the induced 2-norm of the matrix [84]. While this is an upper bound for the induced (Frobenius, ∞)-norm, it also satisfies all the properties to be a norm in its own right, though not an induced norm in terms of any commonly used norms. The ease of calculating this norm makes it attractive. However, neither norm discussed in this section is unitarily invariant, making them dependent on the specific choice of coordinates. This coordinate dependence is attractive in the context of automatic domain splitting along basis vectors, but can be less attractive in other contexts where the physics or engineering applications are less tied to a specific coordinate frame.

6.3 Applications

6.3.1 Approximate Error Bounds for State Transition Tensor Guidance and Control

Rendezvous and proximity operations as well as formation flight of satellites often relies on linear or higher-order approximations of the dynamics in the vicinity of some chief satellite or reference orbit to facilitate computations regarding guidance and control. The state transition matrix and higher-order state transition tensors can be used to approximately propagate the relative motion of some secondary deputy satellite relative to the chief satellite or other reference orbit. In addition to being useful for forward propagation of dynamics, state transition tensors can be used to solve inverse problems. Calculating the initial velocity required to transfer to some position relative to the original orbit or relative to another satellite is one such boundary value problem that can be solved in the linear case by inversion of some block of the state transition matrix, and in the higher-order case by using series reversion methods. Calculating the initial velocity for a rendezvous with the chief satellite falls into this class of inverse problems.

These linear and higher-order series reversions are attractive for onboard implementation of autonomous guidance, navigation, and control systems due to the efficiency of these methods. One drawback to solving linear or higher-order approximations of boundary value problems for guidance is that there is a loss of accuracy as compared with solving the full nonlinear problem. For systems engineering purposes, it is important to understand and bound the error in guidance calculations that can be encountered under expected mission circumstances. We show here that the norm of tensors related to the order $m+1$ state transition tensor can be used to approximately bound the error associated with using an order m state transition tensor model to perform one of the basic guidance and control tasks described above. Though not outlined here, state transition tensors may be used to describe evolution of the states and costates associated with the optimal control of a satellite in the vicinity of some orbit [73]. Approximation error for the thrust, control costs, and terminal states under that policy can be computed in a very similar manner to the impulsive controls presented here. The use of a differential algebra system such as DACE to compute the coefficients of forward and inverse series associated with the flow of a dynamical system makes complex operations to arbitrary order possible while eliminating the need to hand code the complicated tensor expressions described above [101]. Restructuring these coefficients of the polynomials into a tensor form would then allow one to perform tensor norm/eigenvalue analysis though we do not implement these calculations here.

Error Bounds for Propagation of Relative Motion

The m-th order Taylor series approximation of relative motion of a satellite around some reference orbit is given by

$$\delta \mathbf{x}_f \approx \sum_{l=1}^{m} \frac{1}{l!} \mathbf{\Psi}^{(l)}(t_f, t_0) \delta \mathbf{x}_0^l \tag{6.50}$$

This m-th order approximation of relative motion has error

$$\|\delta \mathbf{x}_f - \delta \mathbf{x}_f^{(m)}\|_2 \leq \frac{1}{(m+1)!} \|\mathbf{\Psi}^{(m+1)}\|_2 \|\delta \mathbf{x}_0\|_2^{m+1} + \mathcal{O}(\|\delta \mathbf{x}_0\|_2^{m+2}) \tag{6.51}$$

where the notation $\cdot^{(m)}$ denotes the mth order Taylor approximation of the vector in question. The expression above makes sense to consider when the position and velocity are non-dimensionalized, allowing for them to be similarly scaled.

In the case where position and velocity are not on similar scales, we can also consider errors in position and velocity separately by slicing the relevant tensors. For example, a first-order model position error based on some initial velocity alone can be described:

$$\|\delta\mathbf{r}_f - \delta\mathbf{r}_f^{(1)}\|_2 \leq \frac{1}{2}\|\mathbf{\Psi}^{\mathbf{r}}_{\mathbf{vv}}\|_2\|\delta\mathbf{v}_0\|_2^2 + \mathcal{O}(\|\delta\mathbf{v}_0\|_2^3) \tag{6.52}$$

where $\mathbf{\Psi}^{\mathbf{r}}_{\mathbf{vv}}(t_f, t_0)$ denotes a block of the second-order state transition tensor–the second-order partial derivative tensor for the final position with respect to the initial velocity:

$$\mathbf{\Psi}^{\mathbf{r}}_{\mathbf{vv}}(t_f, t_0) = \frac{\partial^2\mathbf{r}_f}{\partial\mathbf{v}_0^2} \tag{6.53}$$

The inequality in Eq. 6.52 can be employed to approximately bound the error between the linearly propagated and nonlinearly propagated position as depicted in Fig. 6.1. To clarify the phrase "approximately bound," we mean that this is a true upper bound on the second-order contribution to the error, which is dominant for small $\delta\mathbf{v}_0$ making this a good approximation of the true upper bound on the full nonlinear error when $\delta\mathbf{v}_0$ is sufficiently small. One potential heuristic to check whether $\delta\mathbf{v}_0$ is sufficiently small for the second-order term to well-approximate the full nonlinear error is to find the norm of the third-order term and check that this is small relative to the second-order term at the $\delta\mathbf{v}_0$ scale of interest. The second-order term is also likely to be a good approximation of the overall error when the second-order error bound is much smaller than the linear quantity under study at the $\delta\mathbf{v}_0$ scale of interest. We present two examples utilizing the above error bound formulation. In both, we find the maximum error between nonlinear and linear models of the position $\|\delta\mathbf{r}_f - \delta\mathbf{r}_f^{(1)}\|_2$ given initial position at the reference orbit, and initial velocity perturbed within some ball of radius R from the reference orbit initial velocity. This situation where the initial position is at the reference orbit, but the initial velocity perturbation is nonzero models the effects of an impulsive

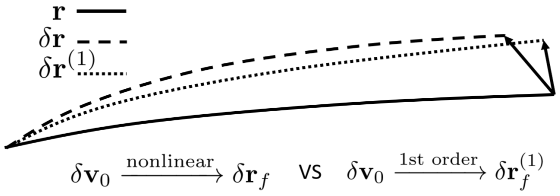

Figure 6.1: Notional depiction of a reference orbit, nonlinear propagation of relative position, and linear propagation of relative position.

burn on a single satellite or the velocity imparted by an explosion on pieces of debris from a satellite. We wish to answer the question: how well does a linear model of the dynamics capture these behaviors for different scales of the velocity perturbation? To do so, analysis is conducted as the maximum scale R of the velocity perturbation $\delta\mathbf{v}_0$ is varied from 0 to 200 meters per second. In the first case, two-body dynamics are employed with an International Space Station-like reference orbit having classical orbital elements semi-major axis, eccentricity, right-ascension of the ascending node, argument of perigee, and initial mean anomaly respectively are $(a, e, i, \Omega, \omega, M_0) = (6738\text{km}, 0.000514, 51.6434^{\circ}, 0^{\circ}, 0^{\circ}, 0^{\circ})$. In the second case, we study the restricted three-body dynamics with the initial conditions of the near-rectilinear halo orbit (NRHO) proposed for NASA's Gateway. We propagate each satellite one tenth of it's respective period in the below error approximations.

In order to validate the approximation in Eq. 6.52, we compare the results from that tensor norm bound with three other methods of characterizing the linearization error. First, to demonstrate a simple method to improve the estimate from Eq. 6.52, we make an educated guess of the perturbation to cause the maximum error between the linear and full nonlinear models. During the calculation of the tensor 2-norm, we find the maximal eigenvector arising in the calculation of the tensor 2-norm. This eigenvector is the unit-normed initial velocity perturbation that produces the largest error between the linear and quadratic models of the dynamics. We then take this unit-normed initial velocity perturbation, scale it by R, and propagate it under the full nonlinear dynamics and linear dynamics to find the final position error. We perform this calculation for the eigenvector calculated as well as the eigenvector in the opposite direction which also produces the same maximum error between linear and quadratic dynamics. The maximum of these two evaluations is taken. This tends to improve the approximation of the maximum error between the linear and full nonlinear models, with only two more evaluations of the nonlinear dynamics propagation.

Next, to determine the true maximum error between linear and nonlinear models, we employ a local numerical optimization using the sequential least squares programming (SLSQP) method in SciPy [128] on the negative of the objective function for maximization. Our objective function in this maximization is the comparison of the propagated true and linear dynamics as a function of the perturbation $\delta \mathbf{v}_0$. The constraint of this maximization is that the velocity perturbation must lie on the sphere defined by the radius R. The initial guess is the eigenvector with the sign that leads to the maximum error between linear and nonlinear evaluations. This method is the best approximation of the true upper bound of the full nonlinear error on the surface of the sphere under the assumption that the local optimization is finding the global maximum.

Finally, a sampling method is used to assure that a global maximum in the error is being approximated in the locally optimized "true" maximum error above. We sample an initial velocity perturbation uniformly at random from the sphere of radius R. This perturbation is then propagated under the full nonlinear dynamics and linear dynamics to find the final position error between the two models. We repeat this sampling 5,000 times, reporting the norm of the largest error. This estimate will not be very precise, but has a good chance of finding a point near the global maximum rather than a local maximum. This process gives the maximum error via sampling, and we check that our maximum error from sampling is always below the "true" maximum error we calculate above using local optimization to validate that we did not locally optimize to a point other than the global maximum.

In Fig. 6.2, we present the maximum errors for propagation of relative motion through the SLSQP method in SciPy. Results are presented in both the two- and restricted three-body cases as discussed above. In the two-body case, we see the magnitude of the maximum error reaches on the order of hundreds of meters with a quadratic relationship between position error and the perturbation magnitude. In the restricted three-body case, we see the magnitude of the maximum error is on the order of tens of kilometers, again with a quadratic relationship. We expect a larger error in the three-body case because this dynamical system is more sensitive to variations in initial conditions. In Fig. 6.3, we present the percentage error between numerical optimization and the three other approaches for estimating the error: sampling, tensor norm (Eq. 6.52), and nonlinear evaluation of the tensor

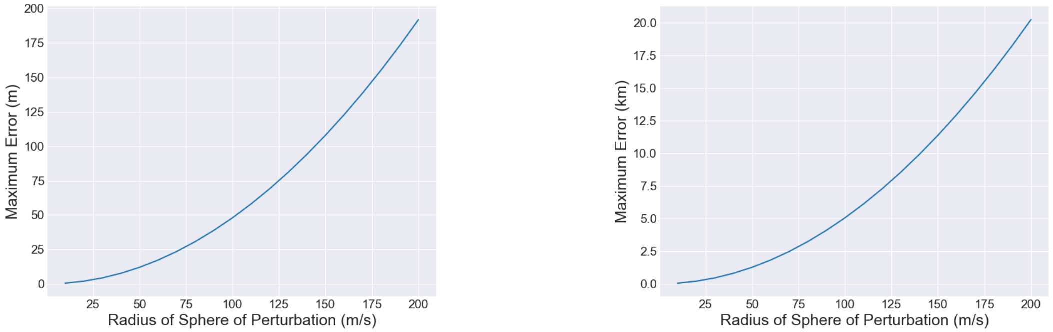

(a) Perturbation vs. Maximum error in ISS example.

(b) Perturbation vs. Maximum error in NRHO example.

Figure 6.2: Maximum error for propagation of relative motion in two-body and restricted three-body dynamics through SciPy optimization.

eigenvector. Results are presented in both the two- and restricted three-body cases discussed above. We see the error found by sampling to be on the scale of 1%, which implies that our local SLSQP optimization is, in fact, finding the global maximum. To answer our proposed question regarding the accuracy of a linear model, in the two-body case, the difference between the tensor norm linear model and true upper error bound increases from 0.1% to 10% over the range of velocity perturbations. In the three body case, this error increases from 3% to 10%. Further, we find the error in our eigenvector evaluation to be on the scale of one one thousandth of one percent. This implies that the direction that maximizes the nonlinear error is very close to the direction which maximizes the quadratic error even though the quadratic and nonlinear errors may deviate by up to one tenth of the true nonlinear error. In Fig. 6.4, we examine the tensor norm defined in Eq. (6.52). Using the same ISS and Gateway NRHO examples, we instead propagate each satellite up to a single period. The tensor 2-norm associated with this flight is plotted against the time of flight, note that the NRHO example has a logarithmic y-scale. We see the tensor norm in the ISS example exhibits sub-exponential growth, while the

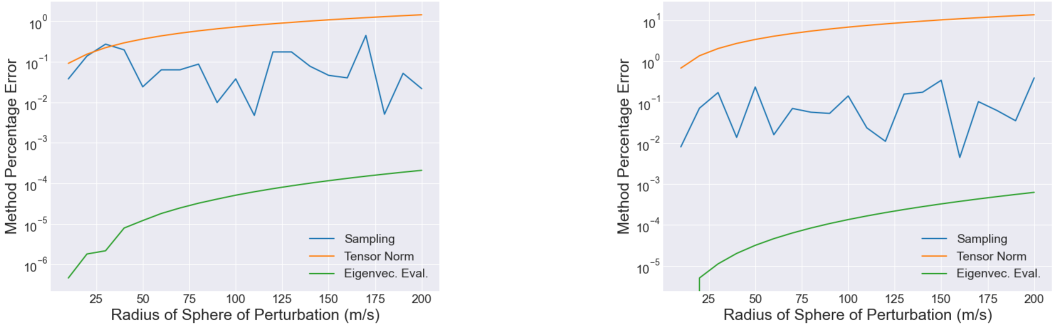

(a) Percent error between methods in ISS example.

(b) Percent error between methods in NRHO example.

Figure 6.3: Relative inaccuracy between methods of calculating maximum error and true upper bound for propagation of relative motion in two-body and restricted three-body dynamics.

tensor norm in the NRHO example exhibits exponential growth. The differences in growth can be attributed to each system's sensitivity to initial conditions and level of nonlinearity. We also can see a spikes in the growth of the tensor norm associated with the NRHO example at around half a period. This spike corresponds to the perilune of the NRHO orbit where the final position is particularly sensitive to initial conditions. The value of the tensor norm is not approaching infinity at this time, but reaching a high finite value.

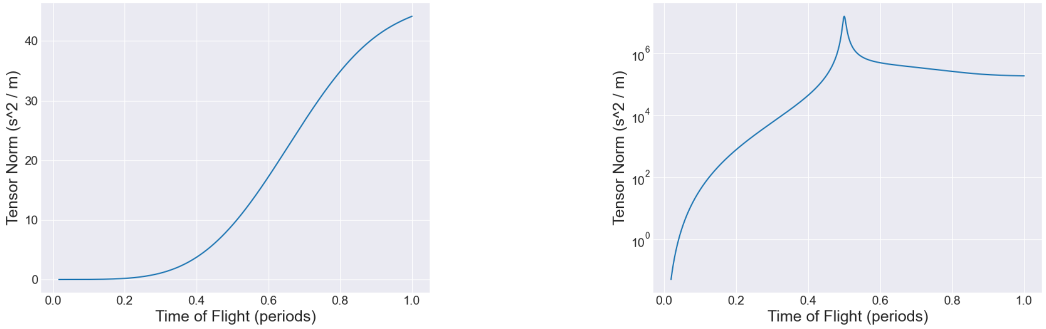

(a) Propagation tensor norm vs. Time of flight in ISS example.

(b) Propagation tensor norm vs. Time of flight in NRHO example (log).

Figure 6.4: Plots of velocity to position propagation tensor norm as time-of-flight varies.

Final Position Error from an Impulsive Transfer

The impulsive relative transfer problem is a basic building block for station-keeping as well as rendezvous. In its simplest form, a satellite at the reference orbit incurs some $\Delta \mathbf{v}$ at the time t_0 in order to reach a desired final relative position $\delta \mathbf{r}_f^*$ with respect to the reference orbit at some time t_f. A linear approximation is often used to solve for the required initial relative velocity [53]

$$\delta \mathbf{v}_0^{(1)} = (\mathbf{\Phi}_{\mathbf{v}}^{\mathbf{r}}(t_f, t_0))^{-1} \delta \mathbf{r}_f^* \tag{6.54}$$

where $\mathbf{\Phi}^{\mathbf{r}}_{\mathbf{v}}$ is the upper right three by three block of Φ, and the superscript (1) indicates that the solution for the initial velocity is a first-order approximation. We might want to understand the accuracy of the linear approximation of the initial velocity $\delta \mathbf{v}_0^{(1)}$. A natural question is what level of error does implementing the linear guidance solution lead to in the final relative position achieved by the $\delta \mathbf{v}_0^{(1)}$ versus the desired $\delta \mathbf{r}_f^*$ when propagated by the true nonlinear dynamics? We are trying to find the maximum miss distance when implementing a linear guidance solution in a truly nonlinear dynamical system. To answer this question, we begin by substituting the linear solution for the initial impulse into a Taylor expansion for the final position

$$\delta \mathbf{r}_f = \mathbf{\Phi}^{\mathbf{r}}_{\mathbf{v}}(t_f, t_0)\delta \mathbf{v}_0^{(1)} + \frac{1}{2}\mathbf{\Psi}^{\mathbf{r}}_{\mathbf{vv}}(t_f, t_0)\left(\delta \mathbf{v}_0^{(1)}\right)^2 + \mathcal{O}\left(\left(\delta \mathbf{v}_0^{(1)}\right)^3\right) \tag{6.55}$$

If we define the position error tensor associated with the second-order order term from the above Taylor expansion

$$(\mathbf{E}^{(1)})^i_{j,k} = \frac{1}{2}\left(\mathbf{\Psi}^{\mathbf{r}}_{\mathbf{vv}}(t_f, t_0)(\mathbf{\Phi}^{\mathbf{r}}_{\mathbf{v}}(t_f, t_0))^{-2}\right)^i_{j,k} = \frac{1}{2}\frac{\partial^2 r^i_f}{\partial v^l_0 \partial v^p_0}\left(\left(\frac{\partial \mathbf{r}_f}{\partial \mathbf{v}_0}\right)^{-1}\right)^l_j \left(\left(\frac{\partial \mathbf{r}_f}{\partial \mathbf{v}_0}\right)^{-1}\right)^p_k \tag{6.56}$$

then, when a linear approximation is used to determine the initial $\Delta \mathbf{v}$ for a transfer, the error in the final position is

$$\|\delta \mathbf{r}_f^* - \delta \mathbf{r}_f\|_2 \leq \left\|\mathbf{E}^{(1)}\right\|_2 \|\delta \mathbf{r}_f^*\|_2^2 + \mathcal{O}\left(\|\delta \mathbf{r}_f^*\|_2^3\right) \tag{6.57}$$

where the 2-norm of the (1-2) tensor above can be calculated by the Z-eigenvector approach as described in Sec. 6.2.4.

Multivariate series reversion methods can be used to find higher-order approximations to inverse problems such as relative motion impulsive transfers and rendezvous [49, 125, 59]. For example, the second-order approximation of the initial

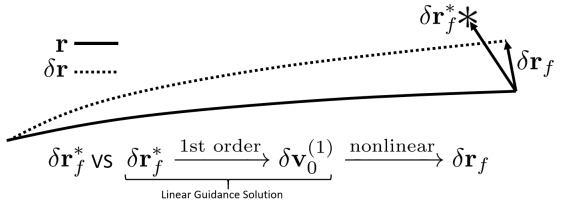

Figure 6.5: Notional depiction of transfer miss distance for linearized initial velocity calculation to reach $\delta\mathbf{r}_f^*$.

relative velocity for the simple case of a transfer is

$$\delta\mathbf{v}_0^{(2)} = (\mathbf{\Phi}_{\mathbf{v}}^{\mathbf{r}}(t_f,t_0))^{-1}\delta\mathbf{r}_f^* - \frac{1}{2}(\mathbf{\Phi}_{\mathbf{v}}^{\mathbf{r}}(t_f,t_0))^{-1}\mathbf{\Psi}_{\mathbf{vv}}^{\mathbf{r}}(t_f,t_0)(\mathbf{\Phi}_{\mathbf{v}}^{\mathbf{r}}(t_f,t_0))^{-2}\left(\delta\mathbf{r}_f^*\right)^2 \quad (6.58)$$

The tensor associated with the position error from the second-order initial velocity solution is

$$(\mathbf{E}^{(2)})^i_{j,k,l} = \left(-\left(\mathbf{\Psi}_{\mathbf{vv}}^{\mathbf{r}}\right)^i_{p_1,p_3}\left((\mathbf{\Phi}_{\mathbf{v}}^{\mathbf{r}})^{-1}\right)^{p_1}_{p_2}\left(\mathbf{\Psi}_{\mathbf{vv}}^{\mathbf{r}}\right)^{p_2}_{p_4,p_5} + \frac{1}{6}\left(\mathbf{\Psi}_{\mathbf{vvv}}^{\mathbf{r}}\right)^{p_1}_{p_3,p_4,p_5}\right)((\mathbf{\Phi}_{\mathbf{v}}^{\mathbf{r}})^{-1})^{p_3}_j((\mathbf{\Phi}_{\mathbf{v}}^{\mathbf{r}})^{-1})^{p_4}_k((\mathbf{\Phi}_{\mathbf{v}}^{\mathbf{r}})^{-1})_l \quad (6.59)$$

and the error in final position from a second-order approximation of the initial velocity is

$$\|\delta\mathbf{r}_f^* - \delta\mathbf{r}_f\|_2 \leq \left\|\mathbf{E}^{(2)}\right\|_2 \|\delta\mathbf{r}_f^*\|_2^3 + \mathcal{O}\left(\|\delta\mathbf{r}_f^*\|_2^4\right) \quad (6.60)$$

This process can be generalized to find the position error from using an mth-order approximation of the correct initial $\Delta\mathbf{v}$, but we only specify the exact form of the error tensor up to second-order due to the complexity of higher-order terms.

$$\|\delta\mathbf{r}_f^* - \delta\mathbf{r}_f\|_2 \leq \left\|\mathbf{E}^{(m)}\right\|_2 \|\delta\mathbf{r}_f^*\|_2^{m+1} + \mathcal{O}\left(\|\delta\mathbf{r}_f^*\|_2^{m+2}\right) \quad (6.61)$$

A notional depiction comparing the linearized guidance trajectory and showing the miss distance from the desired final is presented in Fig. 6.5. We again present two examples utilizing the above error bound formulation. In both, we find the maximum error between nonlinear and linear models of the position $\|\delta\mathbf{r}_f^* - \delta\mathbf{r}_f\|_2$ given an initial position at the reference orbit, and some desired final position sampled from within a ball of radius R from the reference orbit final position.

We use a linear approximation to find the impulsive burn at t_0 that results in the satellite reaching this desired final position $\delta\mathbf{r}_f^*$. To find the maximum miss distance associated with implementing the linear guidance solution, analysis is conducted as the maximum scale R of the final position $\delta\mathbf{r}_f^*$ is varied from 0 to 200 kilometers in the two-body orbit case and between 0 and 2,000 kilometers in the NRHO example. We use the same example cases as in the previous application. Further, we use the same methods of calculating the maximum error, with the adjustment of sampling R as the magnitude of the final desired position deviation.

In Fig. 6.6 we present the maximum errors for propagation of an impulsive transfer through the SLSQP method in SciPy. Similarly to the previous application, the results are presented in both the two- and restricted three-body cases. In the two-body case, we see the magnitude of the maximum error reaches on the order of hundreds of meters. For the order of magnitude larger distance traveled in the NRHO case, the magnitude of error is still on the order of hundreds of meters. This difference in error can be attributed to the restricted three-body system's sensitivity to initial conditions. In the opposite manner of propagation, this results in reduced error, as a given final position corresponds to a smaller initial velocity to reach the desired final position. Thus, a linear approximation performs better in terms of error for solving a transfer in the NRHO case when compared to the two-body case. In Fig. 6.7, we present the percentage error between numerical optimization and the three other approaches for estimating error. Although more erratic, we again find the sampling method-based error on the scale of tenths of a percent to just under ten percent of the true maximum nonlinear error. This again implies that our local SLSQP optimization is finding the global minimum. To answer our proposed question regarding the accuracy of this first-order linear model, we find the difference between the tensor norm linear model and true upper

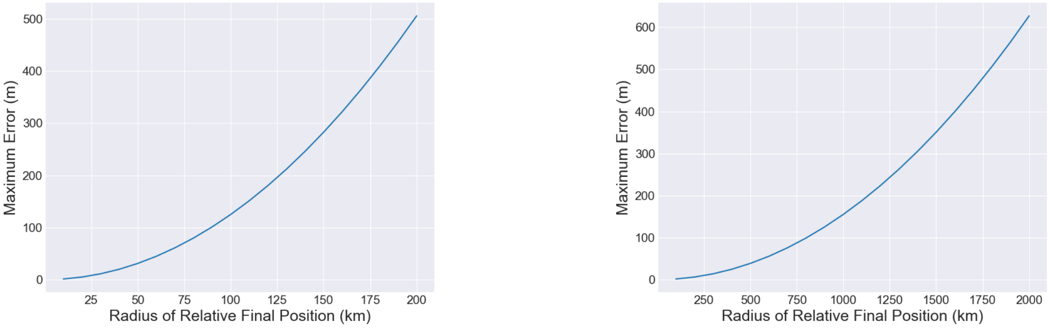

(a) Final position vs. Maximum error in ISS example.

(b) Final position vs. Maximum error in NRHO example.

Figure 6.6: Maximum error for propagation of an impulsive transfer in two-body and restricted three-body dynamics through SciPy optimization.

error bound increases from 0.1% to 10% over the range of final positions. In the three body case, this error increases from 0.1% to 1%. The sampling method giving around 0.1% error relative to the optimized linearization error indicates that the global maximum is being found correctly by the local optimization method in this guidance problem as well. Further, we find the absolute relative error in our eigenvector evaluation (not shown) to be on the scale of less than 10^{-7} in both cases indicating very high accuracy in the agreement of the direction of maximal second-order error and nonlinear error.

In Fig. 6.8, we examine the norm of the tensor defined in Eq. 6.56. We perform the same analysis as the previous application, propagating each satellite one period. In this case, both the ISS and NRHO examples are plotted using a logarithmic y-scale. The norm of the tensor spikes at around half and full periods. These represent relative transfer singularities and are times when the block of the STM $\mathbf{\Phi}^{\mathbf{r}}_{\mathbf{v}}$ becomes singular [76, 93, 37]. At these points the tensor norm is approaching infinity unlike in the earlier previous propagation example where a high, but finite value is achieved. The same approach to infinity is true of spikes in subsequent

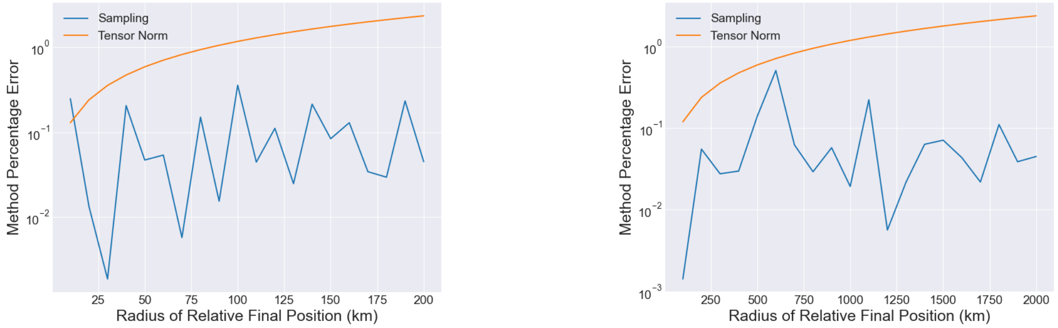

(a) Percent error between methods in ISS example.

(b) Percent error between methods in NRHO example.

Figure 6.7: Relative inaccuracy between methods of calculating maximum error and true upper bound for miss distance in an impulsive transfer in two-body and restricted three-body dynamics.

guidance-related examples.

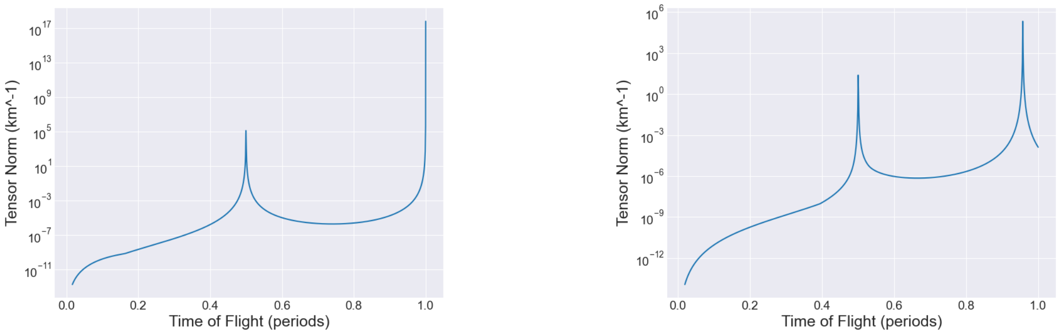

(a) Miss distance tensor norm vs. Time of flight in ISS example.

(b) Miss distance tensor norm vs. Time of flight in NRHO example.

Figure 6.8: Plots of norm associated with miss distance calculation for linearized guidance over varying transfer durations.

Initial Velocity Error from an Impulsive Transfer

In Sec. 6.3.1, we calculated bounds for the miss distance of a linear or higher-order series reversion-based transfer as a function of the desired distance of the transfer.

Here we calculate bounds on the inaccuracy of the initial velocity calculated to reach the final target. The correction term to improve the approximation of the initial velocity of a transfer to one order higher is given in terms of the error tensor from the previous section, so that the $(m+1)$-th order solution is

$$\delta\mathbf{v}_0^{(m+1)} = \delta\mathbf{v}_0^{(m)} - (\mathbf{\Phi}_{\mathbf{v}}^{\mathbf{r}})^{-1}\mathbf{E}^{(m)}(\delta\mathbf{r}_f^*)^{m+1} \tag{6.62}$$

where

$$\left((\mathbf{\Phi}_{\mathbf{v}}^{\mathbf{r}})^{-1}\mathbf{E}^{(m)}\right)^i_{j_1\cdots j_m} = \left((\mathbf{\Phi}_{\mathbf{v}}^{\mathbf{r}})^{-1}\right)^i_l \left(\mathbf{E}^{(m)}\right)^l_{j_1\cdots j_m} \tag{6.63}$$

Eq. 6.62 can be viewed as Newton's method applied to gain one more order of accuracy in the series reversion per iteration [49, 83, 139]. The resulting final term in the inverse series for initial velocity in terms of final position affords the following observation about the error in the m-th order solution to the relative transfer problem:

$$\|\delta\mathbf{v}_0^* - \delta\mathbf{v}_0^{(m)}\|_2 \leq \|(\mathbf{\Phi}_{\mathbf{v}}^{\mathbf{r}})^{-1}\mathbf{E}^{(m)}\|_2\|\delta\mathbf{r}_f^*\|^{m+1} + \mathcal{O}(\|\delta\mathbf{r}_f^*\|^{m+2}) \tag{6.64}$$

Thus, we can approximately bound the error in the order m series reversion solution for the initial velocity to achieve some desired transfer. In particular, this yields an approximate error bound for the initial velocity computed by linear guidance methods versus the true initial velocity that solves the full nonlinear boundary value problem. A notional depiction of the transfer trajectory is presented in Fig. 6.9. The boundary conditions are the same for both the linear and nonlinear versions of the guidance problem, and in each self-consistent model of the dynamics, the solution leads to the final desired position, though the two initial velocity solutions are clearly different (and the linearized solution does not reach the desired position under the nonlinear dynamics as discussed above).

We present a set of examples under the same circumstances as in the miss-distance scenario for a linearized transfer. The true maximum errors for one tenth

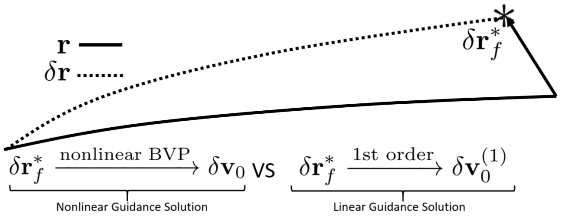

Figure 6.9: Notional depiction of error in linearized initial velocity calculation to reach $\delta\mathbf{r}_f^*$.

of a period transfer can be found in Fig. 6.10. In the two-body case, hundred kilometer transfers calculated with linearized guidance can lead to nearly meter per second errors in the initial velocity, while thousand kilometer transfers in the three-body problem lead to errors on the order of centimeters per second. In some sense, this combined with the previous evidence on miss distance shows that while linear propagation has its limits, linear guidance can actually be quite accurate in the three-body problem. While this might be surprising from the perspective that the three-body problem is a chaotic dynamical system and control would seem more difficult, the large distance scales in this system come into play as well to make thousands of kilometers a relatively small distance as compared with the scale of the NRHO. The error of the tensor norm, sampling, and eigenvector evaluation based methods as compared relative to the numerical optimization around the eigenvector are on the same scale and exhibit the same trends as Fig. 6.7 and are omitted. In Fig. 6.11, we examine the norm of the tensor defined in Eq. 6.63 over the course of an orbital period. Similar spikes can be seen at relative transfer singularity times. Using this tensor norm from this plot and Eq. 6.64, the initial velocity error from linearized guidance calculations can be bounded for small transfer distances.

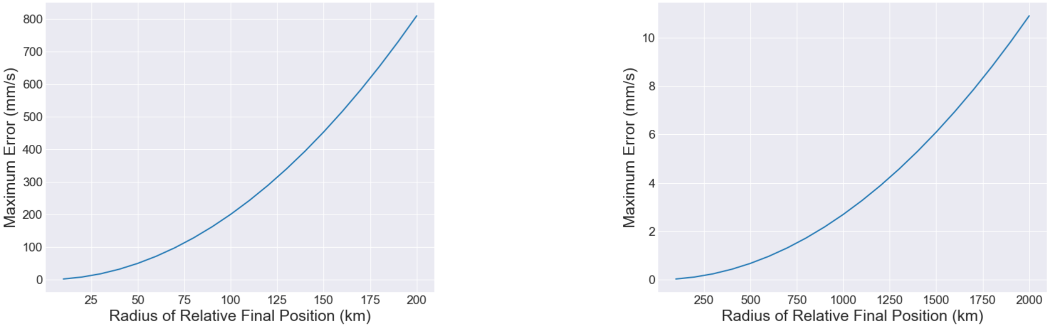

(a) Final position vs. Maximum initial velocity error in ISS example.

(b) Final position vs. Maximum initial velocity error in NRHO example.

Figure 6.10: Maximum error for linear guidance calculation of initial velocity as a function of transfer distance.

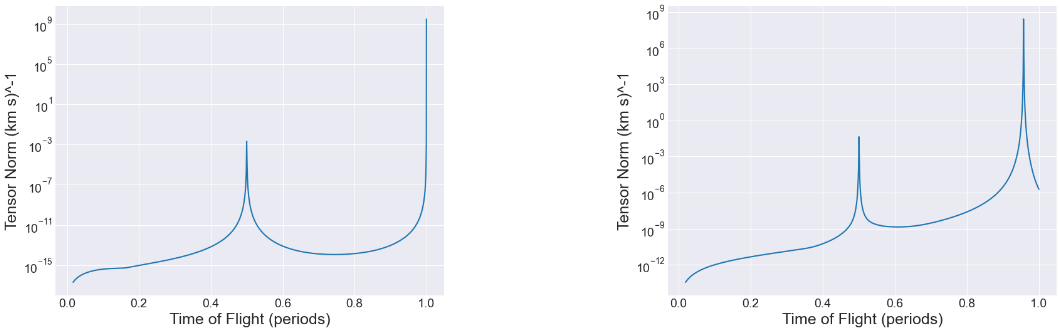

(a) Tensor norm associated with velocity error vs. Time of flight in ISS example.

(b) Tensor norm associated with velocity error vs. Time of flight in NRHO example.

Figure 6.11: Plots of the norm of the tensor that describes initial velocity error as a function of the desired transfer distance while varying time of flight.

Final Position Error During Rendezvous

Before, we were considering the simplified transfer problem, where a satellite begins at the reference orbit and attempts to transfer to another position at a later time. Another related problem is the impulsive rendezvous problem. A satellite begins at some position $\delta \mathbf{r}_0$ relative to the reference orbit and attempts to reach the origin

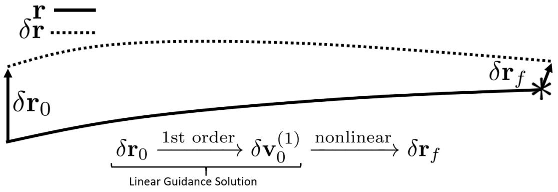

Figure 6.12: Notional depiction of miss distance in a rendezvous calculated with linearized dynamics.

(reference orbit) at some time later. The linear solution to this problem is given:

$$\delta\mathbf{v}_0^{(1)} = -(\boldsymbol{\Phi}^{\mathbf{r}}_{\mathbf{v}})^{-1}\boldsymbol{\Phi}^{\mathbf{r}}_{\mathbf{r}}\delta\mathbf{r}_0 \tag{6.65}$$

The final position error when the first-order solution for the initial velocity is used is

$$\|\delta\mathbf{r}_f\|_2 \leq \|\mathbf{F}^{(1)}\|_2\|\delta\mathbf{r}_0\|_2^2 + \mathcal{O}(\|\delta\mathbf{r}_0\|_2^3) \tag{6.66}$$

where the tensor comes from substituting the first-order transformation from $\delta\mathbf{r}_0$ to $\delta\mathbf{v}_0$ (Eq. 6.65) into any part of the second-order Taylor expansion that takes initial velocity as input

$$(\mathbf{F}^{(1)})^i_{j,k} = \frac{1}{2}\big((\boldsymbol{\Psi}^{\mathbf{r}}_{\mathbf{rr}})^i_{j,k} - (\boldsymbol{\Psi}^{\mathbf{r}}_{\mathbf{rv}})^i_{j,l}((\boldsymbol{\Phi}^{\mathbf{r}}_{\mathbf{v}})^{-1}\boldsymbol{\Phi}^{\mathbf{r}}_{\mathbf{r}})^l_k - (\boldsymbol{\Psi}^{\mathbf{r}}_{\mathbf{vr}})^i_{l,k}((\boldsymbol{\Phi}^{\mathbf{r}}_{\mathbf{v}})^{-1}\boldsymbol{\Phi}^{\mathbf{r}}_{\mathbf{r}})^l_j + (\boldsymbol{\Psi}^{\mathbf{r}}_{\mathbf{vv}})^i_{l,p}((\boldsymbol{\Phi}^{\mathbf{r}}_{\mathbf{v}})^{-1}\boldsymbol{\Phi}^{\mathbf{r}}_{\mathbf{r}})^l_j((\boldsymbol{\Phi}^{\mathbf{r}}_{\mathbf{v}})^{-} \tag{6.67}$$

What we have in this case is an approximate bound for the error in the final position during a rendezvous as a function of the initial distance from the chief satellite being targeted for rendezvous. A notional depiction of miss distance in a rendezvous using linear guidance is presented in Fig. 6.12. Examples of the miss distance from using a linearized guidance solution for rendezvous under the same circumstances as previously described are presented in Fig. 6.13 with the modification that the distance being varied is the initial distance from the reference orbit rather than the final distance. The miss distance is on the order of two to three times that of the transfer that begins at the reference orbit (between one and two kilometers in this particular case). This is because there are more coupled second-order terms coming into play in this scenario than there are in the simple transfer guidance miss distance scenario presented earlier. Again, the error performance of the three methods for approximating the maximum error exhibit the same trends and scales as in the previous two examples and are omitted. In Fig. 6.14, we examine the norm of the tensor defined in Eq. 6.67, which can be used to bound the error of rendezvous miss distance using Eq. 6.66. Unsurprisingly, relative transfer singularities manifest as spikes at certain transfer times in this example as well since each tensor examined in the guidance problems described here has relied on the invertibility of the relevant block of the state transition matrix which is known to become singular at these times. Interestingly, even between these spikes, the tensor norm is not a smooth function of time. Just as is the case with matrix eigenvalues, tensor eigenvalues, upon which this tensor norm is based, do not always vary in a differentiable fashion as a parameter is varied and the eigenvalues pass by one another.

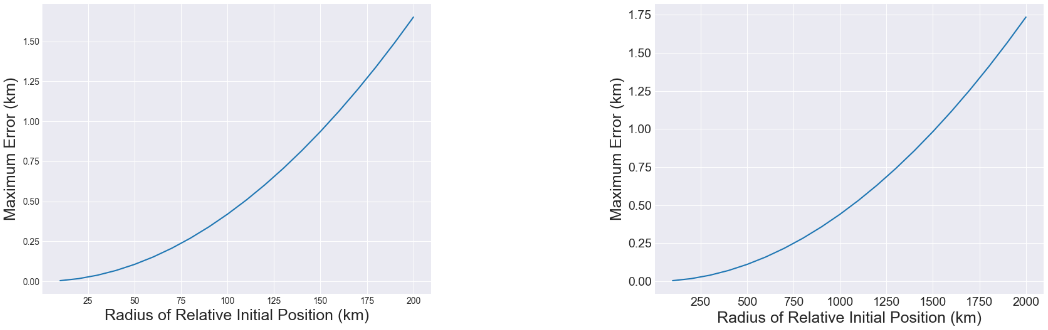

(a) Initial position vs. Max miss distance in ISS example.

(b) Initial position vs. Max miss distance in NRHO example.

Figure 6.13: Maximum miss distance of an impulsive rendezvous implemented using linear guidance.

We have demonstrated that the error associated with linear propagation of motion around some reference orbit as well as linear guidance in the vicinity of

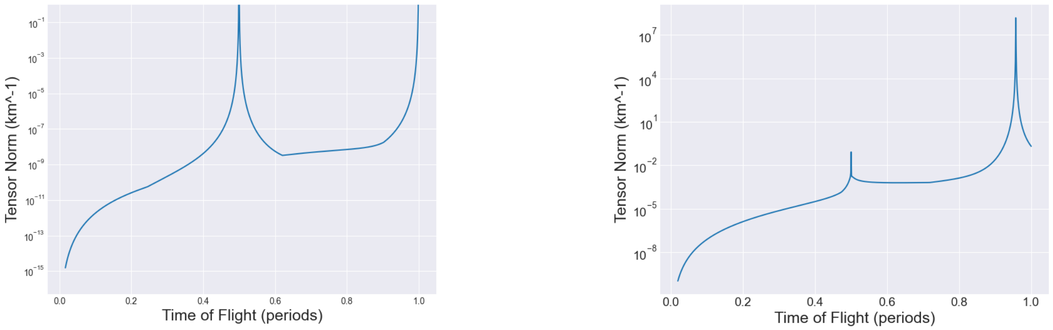

(a) Rendezvous tensor norm vs. Time of flight in ISS example.

(b) Rendezvous tensor norm vs. Time of flight in NRHO example.

Figure 6.14: Plots of tensor norm associated with rendezvous miss distance as transfer duration is varied.

that orbit can be quantified using a tensor norm approach. In the cases examined, the tensor norm approach for bounding error was very accurate at small distances (off by fractions of a percent of the actual error), but degrades as the distances from the reference orbit increase. The advantage of the tensor norm approach is that it can be used to predict the error as a function of the distance scale using a polynomial expression, and does not need to be recomputed for difference scale values. Additionally, the calculation is dominated by calculation of the second-order state transition tensor which requires on the order of 36 times as many equations to be integrated as a single integration of the original dynamical system. Compare this cost with sampling methods which rely on propagating thousands of trajectories to yield similar levels of accuracy and it is evident that the tensor norm method is one to two orders of magnitude faster than sampling, and even faster if the second-order state-transition tensor is already being calculated for another purpose.

6.3.2 Measurement Nonlinearity

To quantify the nonlinearity of a measurement function, it is possible to directly study the norm of a coefficient tensor from the Taylor series approximation. However, another related metric can offer more insight into the error introduced by employing linearization of the measurement function in estimation problems. Suppose we have an initial estimate $\mathbf{x}^-$ for some state vector $\mathbf{x}^*$, and we want to update that estimate given a single measurement $\mathbf{h}(\mathbf{x}^*) = \mathbf{z}$ that is completely certain (i.e. no sensor noise) but potentially underdetermined so that the dimension of $\mathbf{z}$ may be less than the dimension of the state $\mathbf{x}$). Under an additional assumption on the homoscedasticity of the prior state covariance, the extended Kalman update reduces to the estimate

$$\mathbf{x}^+ = \mathbf{x}^- + \left(\frac{\partial \mathbf{h}}{\partial \mathbf{x}}\right)^\dagger_{\mathbf{x}=\mathbf{x}^-} \big(\mathbf{z} - \mathbf{h}(\mathbf{x}^-)\big) \tag{6.68}$$

where $(\cdot)^\dagger$ is the Moore-Penrose pseudoinverse. Expanding $\mathbf{h}(\mathbf{x}^*) = \mathbf{z}$ about $\mathbf{x}^-$ up to second order where we define $\delta\mathbf{x} = \mathbf{x}^* - \mathbf{x}^-$, we obtain

$$\mathbf{x}^+ = \mathbf{x}^- + \left(\frac{\partial \mathbf{h}}{\partial \mathbf{x}}\right)^\dagger_{\mathbf{x}=\mathbf{x}^-} \left(\mathbf{h}(\mathbf{x}^-) + \left(\frac{\partial \mathbf{h}}{\partial \mathbf{x}}\right)_{\mathbf{x}=\mathbf{x}^-} \delta\mathbf{x} + \frac{1}{2}\left(\frac{\partial^2 \mathbf{h}}{\partial \mathbf{x}^2}\right)_{\mathbf{x}=\mathbf{x}^-} \delta\mathbf{x}^2 - \mathbf{h}(\mathbf{x}^-)\right) + \mathcal{O}(\delta\mathbf{x}^3) \tag{6.69}$$

$$= \mathbf{x}^- + \mathbf{\Pi_H}\delta\mathbf{x} + \frac{1}{2}\left(\frac{\partial \mathbf{h}}{\partial \mathbf{x}}\right)^\dagger_{\mathbf{x}=\mathbf{x}^-} \left(\frac{\partial^2 \mathbf{h}}{\partial \mathbf{x}^2}\right)_{\mathbf{x}=\mathbf{x}^-} \delta\mathbf{x}^2 + \mathcal{O}(\delta\mathbf{x}^3) \tag{6.70}$$

$$= \mathbf{x}^* - \mathbf{\Pi_H^\perp}\delta\mathbf{x} + \frac{1}{2}\left(\frac{\partial \mathbf{h}}{\partial \mathbf{x}}\right)^\dagger_{\mathbf{x}=\mathbf{x}^-} \left(\frac{\partial^2 \mathbf{h}}{\partial \mathbf{x}^2}\right)_{\mathbf{x}=\mathbf{x}^-} \delta\mathbf{x}^2 + \mathcal{O}(\delta\mathbf{x}^3) \tag{6.71}$$

where $\mathbf{\Pi_H}$ is the projection of the state into the linearly observable subspace under $\mathbf{h}$—a projection into the row space of the Jacobian of the measurement function

$$\mathbf{H} = \frac{\partial \mathbf{h}}{\partial \mathbf{x}} \tag{6.72}$$

and $\mathbf{\Pi_H^\perp}$ is the projection onto the unobservable subspace of the state given by the right null space of $\mathbf{H}$. Thus, the error in the observable subspace of the state using the linearization for the update is determined up to second-order by the tensor

$$\bar{\mathbf{H}} = \left(\frac{\partial \mathbf{h}}{\partial \mathbf{x}}\right)^{\dagger} \frac{\partial^2 \mathbf{h}}{\partial \mathbf{x}^2} \tag{6.73}$$

with components

$$\bar{H}^i_{jk} = \left(\left(\frac{\partial \mathbf{h}}{\partial \mathbf{x}}\right)^{\dagger}\right)^i_l \left(\frac{\partial^2 \mathbf{h}}{\partial \mathbf{x}^2}\right)^l_{jk} \tag{6.74}$$

It is possible to compute another tensor generalizing Eq. 6.74 that depends specifically on some prior state covariance and sensor noise, but the approach we take above allows us to compare measurement functions without getting into specifics of the sensor noise covariance or prior covariance. Under the homoscedasticity and noise-free sensor assumption above, the 2-norm of $\bar{\mathbf{h}}$ evaluated at some estimate of the state gives the maximum level of error in the observable subspace of the state when using the linear update as a function of how far off that estimate is from the truth

$$\|\mathbf{\Pi_H}(\mathbf{x}^* - \mathbf{x}^+)\|_2 \leq \frac{1}{2}\|\bar{\mathbf{H}}\|_2 \|\delta \mathbf{x}\|_2^2 + \mathcal{O}(\delta \mathbf{x}^3) \tag{6.75}$$

Using the norm of $\bar{\mathbf{H}}$, we can examine how well differing measurement models perform in terms of linearization error in the context of a linear estimation algorithm such as an extended Kalman filter. Note that the error in the unobservable subspace is the same no matter the choice of coordinates for an observation, because the unobservable subspace is the same regardless of the particular coordinate choice for the measurement model.

For example, two common models of an optical measurement are given by

$$\mathbf{h}_a(\mathbf{r}) = [\theta, \phi]^T = \left[\tan^{-1}\left(\frac{y}{x}\right), \sin^{-1}\left(\frac{z}{\|\mathbf{r}\|_2}\right)\right]^T \tag{6.76}$$

$$\mathbf{h}_u(\mathbf{r}) = \frac{\mathbf{r}}{\|\mathbf{r}\|_2} = \frac{1}{\sqrt{x^2 + y^2 + z^2}}[x, y, z]^T \tag{6.77}$$

where $\mathbf{r} = [x, y, z]^T$, θ is the azimuthal angle, and ϕ is the elevation angle. We can evaluate the angle and unit vector models for their error performance in a linear

Figure 6.15: $\|\bar{\mathbf{H}}_a\|_2$ associated with angle measurements as a function of the estimate latitude ϕ

estimation algorithm by evaluating $\|\bar{\mathbf{H}}\|_2$ at various estimates for $\mathbf{r}$. We use position vectors confined to the unit sphere for comparison. The angle measurement function should exhibit the same error behavior at any point with the same value of ϕ due to symmetry. In Fig. 6.15, we plot the value of $\|\bar{\mathbf{H}}\|_2$ associated with the measurement function $\mathbf{h}_a$ as a function of ϕ for an estimate on the unit sphere with that given latitude angle. The value of $\|\bar{\mathbf{H}}_a\|_2$ varies from 1 to ∞, with a minimum at $\phi = 0$ and singularity at $\phi = \pm 90\,\text{deg}$. On the other hand, the unit vector measurement model possesses spherical symmetry, and so it can be expected that the value of $\|\bar{\mathbf{H}}_u\|_2$ is constant when evaluated at estimates anywhere along the unit sphere. For an estimate at $\mathbf{r} = [1,0,0]^T$, the value of the norm of $\bar{\mathbf{H}}_u \delta\mathbf{r}^2$ is plotted in Fig. 6.16 for $\mathbf{r} = [\cos\theta\cos\phi, \sin\theta\cos\phi, \sin\phi]^T$. One can show that the value is given by the expression

$$\|\bar{\mathbf{H}}_u \delta\mathbf{r}^2\|_2 = 4\cos^2(\theta)\cos^2(\phi)\left(\sin^2(\theta)\cos^2(\phi) + \sin^2(\phi)\right) \tag{6.78}$$

which has a maximum of 1 along a 1-dimensional subspace including the point $\delta\mathbf{r} = \sqrt{2}/2[1,1,0]^T$. Thus, $\|\bar{\mathbf{H}}_u\|_2$ is 1 everywhere on the unit ball. At zero degree latitudes, both models perform equally well in terms of linearization error. However, at latitudes greater than around 80 deg, the effects of linearization error on an extended Kalman update are around an order of magnitude greater for the angle measurement model as compared to the unit vector model which has uniformly superior linearization error performance. This, of course, comes at the cost of an increase in the dimension of the measurement model for the unit vector model and a minor additional computational burden when dealing with larger matrices. When minor increases in computational cost are not important, the unit vector approach provides superior linearization error performance for linear estimation algorithms. While, in practice no measurement is perfectly certain, this stylized problem bears a close resemblance to the stressing situation of an extended Kalman filter in which the measurement noise covariance is very low when compared with the state error covariance and a filter can become smug. In fact, a principled method for underweighting measurements in an extended Kalman filter makes use of the bounds on the two norm (as presented in Sec. 6.2.8) of the second-order measurement partial derivative tensor [138]. While this bound could likely be made tighter using the 2-norm of the measurement partial derivatives, it is unlikely that the actual 2-norm would be as easy and quick to compute in closed form for general measurement models as the bound on the 2-norm tends to be. As such, this approach is not pursued further here, and this method is highlighted mostly as a means to compare the efficacy of different measurement models for an

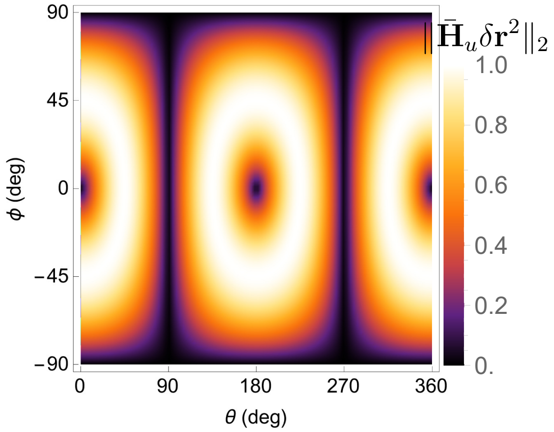

Figure 6.16: The value of $\|\bar{\mathbf{H}}_u \delta \mathbf{r}^2\|_2$ from Eq. 6.78 is plotted for initial estimate errors on the unit sphere.

estimation problem in much the same way the nonlinearity index is employed to compare different state representations for a given dynamical system.

6.3.3 Nonlinearity Index

The nonlinearity index was initially introduced to quantify the level of nonlinearity of a dynamical system as described in various coordinates [57, 58]. It has also been employed in the study of distribution propagation under nonlinear dynamics [95]. Additionally, it has been used to justify the use of calibration and decalibration processes to improve accuracy in settings that employ linearized dynamics [112]. To name a few other applications, the nonlinearity index has been calculated to compare coordinate system choices for optimal control [61], relative motion [4], and aerodynamics [2, 121]. Originally, the nonlinearity index was defined in a manner that depends on the scale of the perturbation to the reference trajectory, and also relies on numerical integration of a large number of randomly sampled perturbed trajectories.

The nonlinearity index $\nu(t_f, t_0)$ associated with a trajectory was originally presented in terms of the Frobenius norm ($\|\cdot\|_F$) of the difference between the STM about some reference orbit and the STM about N other nearby orbits each with an initial deviation of their state vector $\delta\mathbf{x}(t_0)_i$ from the reference initial state $\mathbf{x}(t_0)$ [57, 58]. That is, it was defined as

$$\nu(t_f, t_0) = \sup_{i=1..N} \left(\frac{\|\mathbf{\Phi}(\mathbf{x}(t_0) + \delta\mathbf{x}(t_0)_i; t_f, t_0) - \mathbf{\Phi}(\mathbf{x}(t_0); t_f, t_0)\|_F}{\|\mathbf{\Phi}(\mathbf{x}(t_0); t_f, t_0)\|_F} \right) \tag{6.79}$$

Typically, the chosen initial deviations lie uniformly at random on a sphere centered at zero, but the choice of size for the sphere and the sampling are ad hoc. We present a similar alternative formulation that is scale-free and does not rely on sampling trajectories with initial deviations from the reference. First, we introduce new notation to clarify the dependence of the nonlinearity index on the scale of perturbation r and the choice of output norm a and input norm b. We define

$$\nu_{b,r}^{a}(t_f, t_0) = \sup_{\|\delta\mathbf{x}(t_0)\|_b = r} \left(\frac{\|\mathbf{\Phi}(\mathbf{x}(t_0) + \delta\mathbf{x}(t_0); t_f, t_0) - \mathbf{\Phi}(\mathbf{x}(t_0); t_f, t_0)\|_b^a}{\|\mathbf{\Phi}(\mathbf{x}(t_0); t_f, t_0)\|_b^a \, \|\delta\mathbf{x}(t_0)\|_b} \right) \tag{6.80}$$

To excise the scale parameter r from equation (6.80), we can take the limit as r approaches zero. Then

$$\nu_b^a(t_f, t_0) = \lim_{r \to 0} \nu_{b,r}^a(t_f, t_0) = \frac{\|\mathbf{\Psi}(\mathbf{x}(t_0); t_f, t_0)\|_b^a}{\|\mathbf{\Phi}(\mathbf{x}(t_0); t_f, t_0)\|_b^a} \tag{6.81}$$

A scale-free version of the original nonlinearity index due to Junkins[57] does not match this form where the two norms in the quotient are the same as one another, but takes the similar form

$$\nu^*(t_f, t_0) = \frac{\|\mathbf{\Psi}(\mathbf{x}(t_0); t_f, t_0)\|_2^F}{\|\mathbf{\Phi}(\mathbf{x}(t_0); t_f, t_0)\|_F} \tag{6.82}$$

As was discussed in Sec. 6.2.9, a similar nonlinearity index was presented in terms of an easily computed upper bound on the (Frobenius, ∞)-norm of the second-order state transition tensor [84]

$$\nu^{\square}(t_f, t_0) = \frac{\|\mathbf{\Psi}^{\infty}(\mathbf{x}(t_0); t_f, t_0)\|_F}{\|\mathbf{\Phi}(\mathbf{x}(t_0); t_f, t_0)\|_F} \geq \frac{\|\mathbf{\Psi}(\mathbf{x}(t_0); t_f, t_0)\|_{\infty}^F}{\|\mathbf{\Phi}(\mathbf{x}(t_0); t_f, t_0)\|_F} \tag{6.83}$$

where the matrix $(.)^{\infty}$ was defined in Eq. 6.48. This nonlinearity index is not unitarily invariant and varies based on rotations of the coordinate system. We denote this index with a superscript box because of its relation to the infinity norm and the need to disambiguate from a norm/index induced by the infinity norm. Note that while the expression above is identical to that presented in [84], the language of differential algebra was used and the connection to the induced norm bound, while implied in the original work, is our own formalized observation.

In any of the above cases, by taking a quotient of a tensor norm and a matrix norm, we have split up two quantities that are each obtained as the solutions to constrained optimization problems. Alternatively, Jenson and Scheeres presented a formulation of the nonlinearity index called Tensor Eigenpair Measure of Nonlinearity (TEMoN) in which the nonlinearity index is framed in terms of a single constrained optimization problem, rather than two independent optimizations [54]. This innovative work was the first to introduce the study of tensor eigenvalues to the astrodynamics as well as guidance, navigation, and control communities. In their paper, two optimization problems appear. One nonlinearity measure of interest is given by the optimization

$$\aleph_{m,R} = \max_{\delta\mathbf{x}(t_0)\in\mathcal{B}_R} \left| \frac{\mathbf{C}^{(3)}\delta\mathbf{x}^3(t_0) + ... + \mathbf{C}^{(m)}\delta\mathbf{x}^m(t_0)}{\mathbf{C}^{(2)}\delta\mathbf{x}^2(t_0)} \right| \tag{6.84}$$

On the other hand, TEMoN is given by the optimization

$$\tau_{m,R} = \max_{\delta\mathbf{x}(t_0)\in\mathcal{B}_R} \left| \frac{\mathbf{C}^{(m)}\delta\mathbf{x}^m(t_0)}{\mathbf{C}^{(2)}\delta\mathbf{x}^2(t_0)} \right| \tag{6.85}$$

and the previous measure of nonlinearity from Eq. 6.84 is upper bounded by the sum of individual TEMoN optimizations for each order up to m

$$\aleph_{m,R} \leq \sum_{l=3}^{m} \tau_{m,R} \tag{6.86}$$

Jenson and Scheeres proposed a method to calculate TEMoN involving finding Z-eigenvalues of an $m+2$ order tensor derived from the method of Lagrange multipliers. However, this method requires finding more than just the eigenvector associated with the largest eigenvalue. Instead, the algorithm relies on methods other than symmetric higher-order power iteration to find as many eigenvectors as possible, checking each to find which yields the largest TEMoN. In general, finding all eigenvectors, especially those that are not associated with the largest eigenvalues, is a difficult task that has no guarantees of finding all eigenpairs and can be computationally intensive [9]. We propose another nonlinearity index in a similar spirit called the D-Eigenvalue Measure of Nonlinearity (DEMoN). The development of this index also motivates a simpler method for computing TEMoN using the largest eigenvalue of some tensor computable by shifted symmetric higher order power iteration. DEMoN-m is given as

$$\mu^{(m)}(t_f, t_0) = \sup_{\|\delta \mathbf{x}(t_0)\|_2 = 1} \left(\frac{\left\| \mathbf{\Psi}^{(m)}(\mathbf{x}(t_0); t_f, t_0) \delta \mathbf{x}^m(t_0) \right\|_2}{\left\| \mathbf{\Phi}(\mathbf{x}(t_0); t_f, t_0) \delta \mathbf{x}(t_0) \right\|_2} \right) \tag{6.87}$$

If the optimization were conducted over a ball of radius R rather than the unit ball, the result would be scaled by a factor of R^{m-1} given the homogeneity of multilinear operators. This makes the index scale-free in a sense unlike any index that involves a nonhomogeneous polynomial or full nonlinear function.

All of the indices presented so far besides the original sampling-based index are scale-free in a similar fashion. The most significant order to calculate is the $m = 2$ case since this accounts for the deviations from linearity of dynamics closest to the reference orbit. The index $\mu^{(2)}$ quantifies how large the norm of the quadratic term in the Taylor series can become relative to the norm of the linear term given the same input vector. In order to calculate DEMoN, a D-eigenvalue problem, and a rescaling of the resulting eigenvector can be substituted back into Eq. 6.87. This nonlinearity index can be calculated using only the largest D-eigenpair, avoiding the difficult task of computing all eigenpairs encountered by the original implementation of TEMoN. The vector $\delta \mathbf{x}(t_0)$ that maximizes the expression in Eq. 6.87 is parallel to the maximizer of the related optimization

$$\sup_{\delta \mathbf{x}_0^T \mathbf{\Phi}^T \mathbf{\Phi} \delta \mathbf{x}_0 = 1} \left\| \mathbf{\Psi}^{(m)}(\mathbf{x}(t_0); t_f, t_0) \delta \mathbf{x}^m(t_0) \right\|_2^2 \tag{6.88}$$

where the arguments of the shorthand $\mathbf{\Phi}$ and $\delta \mathbf{x}_0$ are understood to match the arguments in the rest of the expression. Refer to Sec. 6.2.5 to compute the vector $\delta \mathbf{x}_0^*$ maximizing the above expression using the theory of D-eigenvalues where $\mathbf{D} = \mathbf{\Phi}^T \mathbf{\Phi}$ and the square root of $\mathbf{D}$ need not be calculated using the Cholesky factorization, but instead is given by $\mathbf{\Phi}$. With this vector $\delta \mathbf{x}_0^*$ computed, DEMoN is the expression in Eq. 6.87 evaluated at a normalized (to the unit ball) $\delta\mathbf{x}_0^*$. A disadvantage of this approach is that the sum of the squares of DEMoN for various orders plus unity (to account for the second-order CGT term) gives a more relaxed bound on the nonlinearity index $\aleph_{m,R}$ than the sum of TEMoN terms. On the other hand, a sum of DEMoN terms provides a bound on the nonlinearity index

$$\beth_{m,R} = \max_{\delta\mathbf{x}(t_0)\in\mathcal{B}_R} \frac{\left\| \frac{1}{2!}\mathbf{\Psi}^{(2)}\delta\mathbf{x}^2(t_0) + ... + \frac{1}{m!}\mathbf{\Psi}^{(m)}\delta\mathbf{x}^m(t_0) \right\|_2}{\left\|\mathbf{C}^{(2)}\delta\mathbf{x}^2(t_0)\right\|_2} \tag{6.89}$$

$$\beth_{m,R} \leq \sum_{l=2}^{m} \frac{R^{m-1}}{m!}\mu^{(m)} \tag{6.90}$$

While $\aleph_{m,R}$ gives the **error of the norm** of the m-th order approximation of the final deviation vector relative to the norm of the linear approximation, this index denoted $\beth_{m,R}$ (Beth from the Hebrew alphabet) gives the **norm of the error** of the m-th order approximation of the final deviation vector relative to the norm of the linear approximation. Both TEMoN and DEMoN as well as $\aleph$ and $\beth$ are valid indices to compute with differing meanings: an error of a norm or a norm of an error. The nature of TEMoN and the index $\aleph$ implies that they may miss/understate strong nonlinearities with contributions in different directions than the linear contribution. Orthogonal contributions like these do not change the norm of the final deviation vector up to a linear approximation. For concreteness, we present the following extreme stylized example. Consider two dynamical systems in $\mathbb{R}^2$ and reference trajectories (one is the primed dynamical system and the other is the unprimed dynamical system) such that the state transition matrix and second-order state transition tensor for either system have all zero entries except for

$$\Phi_1^1 = 1, \quad \Psi_{1,1}^2 = 1 \tag{6.91}$$

$$(\Phi')_1^1 = 1, \quad (\Psi')_{1,1}^1 = 1 \tag{6.92}$$

$$\tag{6.93}$$

In this situation, the values of DEMoN and $\beth$ are identical for the two systems (DEMoN has a value of 1). On the other hand, $\tau_{3,R} = 0$ and $\tau'_{3,R} = \frac{1}{2}R$, while $\tau_{4,R} = \frac{1}{4}R^2 = \tau'_{4,R}$, so that $\aleph_{m,R} = \frac{1}{4}R^2$ and $\aleph'_{m,R} = \frac{1}{2}R + \frac{1}{4}R^2$ for any m higher than 4. While these two systems seem equally nonlinear, TEMoN and $\aleph$ index one of these systems as being substantially more nonlinear than the other. The fact that TEMoN characterizes an error of a norm rather than a norm of an error and can underestimate the nonlinearity of some functions gives a potential advantage for considering $\beth$ over $\aleph$ and DEMoN over TEMoN. However, the error in the norm interpretation of TEMoN may be of interest still. Having derived DEMoN, we see that a slight modification of this D-eigenvalue methodology allows for computation of TEMoN. The main issue is that the higher-order CGT tensors are not necessarily even order or convex on the unit ball, so symmetric higher-order power iteration may not be convergent as is the case in calculating DEMoN which deals only in squares of tensors and not products of different tensors. As a result, TEMoN must be calculated using a shifted symmetric higher-order power iteration. For details, see Sec. B.3.

Since each of the nonlinearity indices above results from some constrained optimization problem, each of them has some corresponding argument or input vector that leads to the nonlinearity index. These vectors which solve the constrained optimization problem can be used to identify possible direction for splitting of a Gaussian mixture model. $\nu^{\Box}$ was used for just this purpose in the context of splitting Gaussian mixtures in a coordinate axis aligned fashion [84]. Using vectors associated with other nonlinearity indices such as ν_2^2 or $\mu^{(2)}$ can give a single optimal non-axis-aligned splitting direction. The former focuses on reducing absolute error from second-order nonlinearities, while the latter focuses on reducing percentage error from second-order nonlinearities. Similar constrained optimizations associated with D-eigenvalues can be posed where $\mathbf{D} = \mathbf{P}^{-1}$ is the inverse of the covariance matrix for the Gaussian distribution being split. These problems can be interpreted as finding the direction in which nonlinearity is greatest given inputs that are equally likely. Though not phrased in the tensor norm formalism we have presented, the vector that solves the constrained maximization problem associated with the (Frobenius, $\mathbf{P}^{-1}$)-norm of the second-order partial derivative tensor of a flow or measurement function has been employed for choosing a maximally nonlinear Gaussian mixture splitting direction [124].

With the nonlinearity indices derived and presented above, we show two examples with a selection of the nonlinearity indices. First, we present the nonlinearity index associated with nondimensional circular two-body motion. Two-body dynamics were defined in Eq. 1.1. To further simplify the problem and make interpretation of the nonlinearity index simpler, we nondimensionalize the two-body problem using a reference circular orbit with semimajor axis a to form the nondimensional state vector $\mathbf{x}' = [\mathbf{r}'^T, \mathbf{v}'^T]^T$.

$$\frac{d}{d\tau}\mathbf{x}' = \begin{bmatrix} \mathbf{v}' \\ \dfrac{-\mathbf{r}'}{\|\mathbf{r}'\|_2^3} \end{bmatrix} \tag{6.94}$$

where $\|\mathbf{r}'\|_2^3$ denotes the cube of the 2-norm. The states and times are related by the following coordinate changes

$$\mathbf{r}' = \mathbf{r}/a \tag{6.95}$$

$$\tau = \omega t \tag{6.96}$$

$$\mathbf{v}' = \mathbf{v}/(a\omega) \tag{6.97}$$

where ω is the mean motion of the circular orbit with semimajor axis a. The initial conditions we employ for the generic planar nondimensional circular orbit are $\mathbf{x}_0 = [1, 0, 0, 0, 1, 0]^T$. A number of nonlinearity indices are presented on the left in Fig. 6.17. These include DEMoN-2 on its own due to scale considerations, TEMoN-3, and the nonlinearity indices associated with the 2-, (Frobenius, 2)-, and (∞, 2)-norms as well as the flattening based 2-norm bound of the second-order state transition tensor. For the 2-norm bound based nonlinearity index, we take the quotient of the 2-norm bound in Sec. 6.2.8 applied to the second-order state transition tensor with the 2-norm of the state transition matrix. Since the values of the 2-norm, (Frobenius, 2)-norm, and 2-norm bound are very similar, we break out the difference between the 2-norm nonlinearity index and these two other indices on their own. In addition to the two-body example, we also use the Gateway NRHO beginning at apolune to demonstrate how these nonlinearity indices grow in the circular restricted three body problem on the right hand side of Fig. 6.17. The sensitivity to initial conditions exhibited by the three-body problem manifests itself in a much higher growth rate of the nonlinearity indices than in the two-body case. We also see a peak in nonlinearity near perilune which is consistent with previous analysis with TEMoN [54]. Note that the 2-norm bound does in-fact give an upper bound on the 2-norm based nonlinearity index in both cases for all times, and quite a tight one at that. One of the main takeaways is that in the case of two- and three-body motion, these nonlinearity indices exhibit very similar patterns of growth over time and may be quite interchangeable-especially in the case of the 2-norm, (Frobenius, 2)-norm, and 2-norm upper bound based nonlinearity indices. The main exception is that the overall magnitudes differ between TEMoN, DEMoN, and the nonlinearity indices associated with various norms of the second-order state transition tensor. This implies that the simpler to compute nonlinearity indices such as the (Frobenius, 2)-norm or the $(\infty, 2)$-norm might be the best to use, though the $(\infty, 2)$-norm may be advised against due to its non-smoothness.

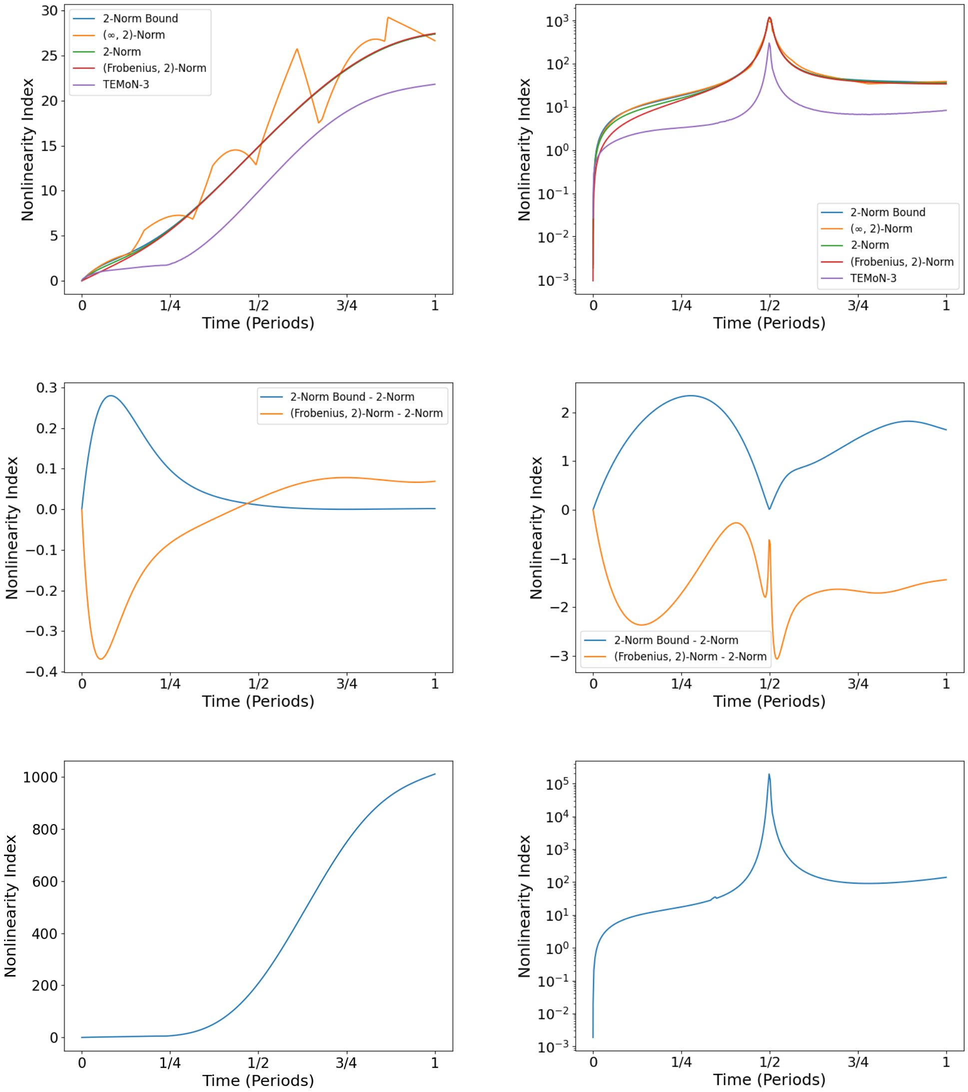

Figure 6.17: The nonlinearity indices associated with nondimensional circular two-body motion on the left and the Earth-Moon circular restricted three-body problem Gateway NRHO on the right.

6.4 Conclusion

In this paper, we have developed and synthesized a number of existing approaches to quantifying nonlinearity of a function or flow of a dynamical system into a single framework based on tensor operator norms. This led to an easy-to-compute and easy-to-interpret scale-free nonlinearity index that most closely parallels the original nonlinearity index presented over two decades ago, as well as two easier-to-compute versions of the modern tensor-eigenvalue-based nonlinearity index (TEMoN and DEMoN). One of these tensor eigenvalue based measures of nonlinearity (DEMoN) quantifies the norm of a deviation from linearity rather than a deviation of norm predicted by linear and nonlinear models as has been done previously. In addition to presenting nonlinearity indices as a means to quantify nonlinearity of a dynamical system and compare different formulations of a system, we have shown that the same tools for defining a nonlinearity index can be employed to estimate the error resulting from commonly used linear algorithms applied to a nonlinear system. In particular, we demonstrated the use of tensor norms to approximately bound the error in linearized guidance methods for stationkeeping or rendezvous. Additionally, we presented a method for analyzing the maximum error in the extended Kalman filter update step when a measurement is much more precise than the current state estimate. This error approximation methodology can be applied with some modifications to many linear algorithms in guidance, navigation, and control. The methodology is more efficient than sampling-based methods for quantifying error and gives an analytical grasp on error performance for varying distance scales from the point at which linearization was applied. Though we do not pursue it here, future work could involve using this same methodology in a statistical context for quantifying non-Gaussianity by examining norms of tensors related to higher-order moments of a distribution.

CHAPTER 7

CONCLUSION

This thesis began by summarizing the calculation of coefficients tensors arising from the Taylor series expansion of the flow of a dynamical system along with series reversion methods for inverting these series. We proceeded with two chapters that presented contributions involving linear analysis of dynamical systems. The first provided linear analysis for the stationkeeping of a starshade satellite relative to a space telescope during formation flying operations to observe an exoplanet. The second chapter explored the relationship between guidance methods for rendezvous and proximity operations, the debris pinch point phenomena, and bifurcations in parameterized boundary value problems. The contributions of this thesis that employ multilinear methods and higher-order tensors are twofold. In the following two chapters, we solved an optimal control problem and an optimal estimation problem that both required second-order terms to resolve an inherently second-order energy quantity as well as a linear observability issue. These are algorithms that don't simply use higher-order terms to increase accuracy of a linear algorithm, but instead rely necessarily on the nonlinear aspects of a guidance, navigation, and control problem to render it tractable. In the final chapter, we used higher-order terms in a Taylor series as well as the notion of a tensor operator norm to quantify the degree of nonlinearity of a system along with the accuracy of guidance, navigation, and control algorithms relying on linearization. With these metrics for accuracy of an algorithm, systems engineers or algorithm designers can rigorously and efficiently assess the error performance of a guidance, navigation, and control algorithm under proscribed operating conditions.

APPENDIX A

ANGLES-ONLY ORBIT DETERMINATION AND THE OVERDETERMINED EIGENVALUE PROBLEM

A.1 Pseudo-Inverse Approximation for Overdetermined Eigenvalue Problem

The generalized eigenvalue problem with m by n matrices $\mathbf{A}, \mathbf{B}$ with $m > n$ is not guaranteed to have any solutions:

$$\mathbf{Ax} = \lambda \mathbf{Bx} \tag{A.1}$$

In order to address this, the problem can be reformulated in a least squares sense [30]:

$$\arg \min_{\mathbf{x},\lambda} \|\mathbf{Ax} - \lambda \mathbf{Bx}\|_2 \tag{A.2}$$

We present a new approximation of the solution to this problem in the form of the following standard eigevalue problem:

$$\mathbf{B}^\dagger \mathbf{Ax} = \lambda \mathbf{x} \tag{A.3}$$

To demonstrate the accuracy of this method, consider expanding the square of the 2-norm from Eq. A.2 and setting the derivative to 0:

$$0 = \left(\lambda^2 \mathbf{B}^\top \mathbf{B} - \lambda \mathbf{A}^\top \mathbf{B} - \lambda \mathbf{B}^\top \mathbf{A} + \mathbf{A}^\top \mathbf{A}\right) \mathbf{x} \tag{A.4}$$

$$0 = \left(\lambda^2 \mathbf{I} - \lambda (\mathbf{B}^\top \mathbf{B})^{-1} \mathbf{A}^\top \mathbf{B} - \lambda (\mathbf{B}^\top \mathbf{B})^{-1} \mathbf{B}^\top \mathbf{A} + (\mathbf{B}^\top \mathbf{B})^{-1} \mathbf{A}^\top \mathbf{A}\right) \mathbf{x} \tag{A.5}$$

$$0 = \left(\lambda^2 \mathbf{I} - \lambda (\mathbf{B}^\top \mathbf{B})^{-1} \mathbf{A}^\top \mathbf{B} - \lambda \mathbf{B}^\dagger \mathbf{A} + (\mathbf{B}^\top \mathbf{B})^{-1} \mathbf{A}^\top \mathbf{A}\right) \mathbf{x} \tag{A.6}$$

$$0 = \left(\lambda^2 \mathbf{I} - \lambda \mathbf{B}^\dagger \mathbf{A}\right) \mathbf{x} + \left((\mathbf{B}^\top \mathbf{B})^{-1} \mathbf{A}^\top \mathbf{A} - \lambda (\mathbf{B}^\top \mathbf{B})^{-1} \mathbf{A}^\top \mathbf{B}\right) \mathbf{x} \tag{A.7}$$

$$0 = \left(\lambda^2 \mathbf{I} - \lambda \mathbf{B}^\dagger \mathbf{A}\right) \mathbf{x} + \underbrace{(\mathbf{B}^\top \mathbf{B})^{-1} \mathbf{A}^\top (\mathbf{A} - \lambda \mathbf{B}) \mathbf{x}}_{\approx 0} \tag{A.8}$$

Where we get A.5 from multiplying through on the left by $(\mathbf{B}^\top\mathbf{B})^{-1}$ and A.8 by the fact that $(\mathbf{B}^\top\mathbf{B})^{-1}\mathbf{A}^\top(\mathbf{A} - \lambda\mathbf{B})\mathbf{x} \approx 0$ as $(\mathbf{A} - \lambda\mathbf{B})\mathbf{x}$ is being minimized. From Eq. A.8 we obtain justification for using the pseudo-inverse approximate solution given in Eq. A.3.

A.2 Quadratic Eigenvalue for Overdetermined Eigenvalue Problem

We note that Eq. A.4 is a quadratic eigenvalue problem. While solution methods based on the generalized Schur decomposition for the overdetermined eigenvalue problem have been presented [30], to our knowledge the formulation of an overdetermined eigenvalue problem as a quadratic eigenvalue problem has not been given before in the numerical linear algebra literature. This reformulation makes it easy to apply a standard generalized eigenvalue problem solver to the overdetermined eigenvalue problem. The quadratic eigenvalue problem is well-studied, and admits reformulation as a linear eigenvalue problem in twice as many dimensions by a process called linearization [122]. Unlike linearization in the context of the first-order truncation of a Taylor series, the linearization of a quadratic eigenvalue problem is not an approximation, and solutions of the linearized problem are exact (up to errors in the numerical calculation) solutions of the original quadratic problem and thus the overdetermined eigenvalue problem. However, even though the quadratic eigenvalue problem in Eq. A.4 has symmetric matrices in each of the matrix coefficients of the constant, linear, and quadratic terms in λ, and a symmetric linearization exists, the generalized eigenvalue problem with symmetric matrices for both terms does not necessarily have the same properties of the symmetric standard eigenvalue problem with all real eigenvalues. In fact, the eigenvalues arising from solving the overdetermined eigenvalue problem in this way are often complex even though the original matrices have real entries and the intermediate quadratic and linearized problems deal strictly in symmetric matrices.

Letting $\mathbf{Q} = \mathbf{B}^T\mathbf{B}, \quad \mathbf{L} = -\mathbf{B}^T\mathbf{A} - \mathbf{A}^T\mathbf{B}, \quad \mathbf{C} = \mathbf{A}^T\mathbf{A}$, Eq. A.4 becomes the quadratic eigenvalue problem

$$\lambda^2\mathbf{Q} + \lambda\mathbf{L} + \mathbf{C} = 0 \tag{A.9}$$

The symmetric linearization of the quadratic eigenvalue problem is

$$\begin{bmatrix} \mathbf{0} & \mathbf{C} \\ \mathbf{C} & \mathbf{L} \end{bmatrix} \mathbf{y} = \lambda \begin{bmatrix} \mathbf{C} & \mathbf{0} \\ \mathbf{0} & -\mathbf{Q} \end{bmatrix} \mathbf{y} \tag{A.10}$$

Then eigenpairs $(\mathbf{y}_i, \lambda_i)$ of the generalized eigenvector problem in Eq. A.10 take the form

$$\mathbf{y}_i = \begin{bmatrix} \mathbf{z}_i \\ \lambda_i\mathbf{z}_i \end{bmatrix} \tag{A.11}$$

The unit eigenvectors are given by

$$\hat{\mathbf{x}}_i = \frac{\mathbf{z}_i}{\|\mathbf{z}_i\|} \tag{A.12}$$

This yields eigenvector and eigenvalue pairs $(\hat{\mathbf{x}}_i, \lambda_i)$ to the original quadratic eigenvalue problem in Eq. A.9 and thus the overdetermined eigenvalue problem from Eq. A.2.

APPENDIX B

TENSOR NORM AND NONLINEARITY INDEX CALCULATION DETAILS

B.1 Sufficiency of Partial Symmetry for Higher-Order Power Iteration

We begin by showing an alternative expression for Eq. 6.17 that references $\tilde{\mathbf{B}}$ rather than $\hat{\mathbf{B}}$. The contraction of the symmetrized tensor $\hat{\mathbf{B}}$ with $2m-1$ copies of the vector $\mathbf{x}$ can be computed instead as the average of all $2m$ different ways we could perform the $2m-1$ contractions with the non-symmetric tensor $\tilde{\mathbf{B}}$. Each of the $2m$ ways of performing the contraction can be described by which dimension is not contracted with:

$$\left(\hat{\mathbf{B}}\mathbf{x}^{2m-1}\right)_l = \frac{1}{2m}\sum_{j=1}^{2m} \tilde{\mathbf{B}}_{i_1,\ldots,i_{2m}} \delta_l^{i_j} \prod_{k\neq j} x^{i_k} \tag{B.1}$$

where $\delta_l^{i_j}$ is the Kronecker delta given by contracting an index from then Euclidean metric tensor with the Euclidean inverse metric tensor. The expression in Eq. B.1 is true regardless of any partial symmetry of $\tilde{\mathbf{B}}$. However, we note a few special properties of the tensors under consideration: $\mathbf{B}$ is partially symmetric under any permutation of the m covariant indices, leading $\tilde{\mathbf{B}}$ to be symmetric under permutations of $i_1..i_m$ amongst themselves and $i_{m+1}..i_{2m}$ amongst themselves. Additionally, $\tilde{\mathbf{B}}$ is also symmetric under the permutation $(i_1...i_m, i_{m+1}..i_{2m}) \rightarrow (i_{m+1}...i_{2m}, i_1...i_m)$ as well as any permutations generated by the two mentioned above. As a result, for all $k \in \{1...2m\}$, there exists a permutation σ such that the first element of $\sigma((i_1...i_m, i_{m+1}..i_{2m}))$ is i_k.

An example with a 4-dimensional tensor $\tilde{\mathbf{B}}$ is most instructive:

$$\tilde{\mathbf{B}}_{i_1,i_2,i_3,i_4} = \tilde{\mathbf{B}}_{i_2,i_1,i_3,i_4} = \tilde{\mathbf{B}}_{i_3,i_4,i_1,i_2} = \tilde{\mathbf{B}}_{i_4,i_3,i_1,i_2} \tag{B.2}$$

The first equality comes from partial symmetry of the covariant indices of $\mathbf{B}$, the second equality comes from the partial symmetry of the square of a tensor, and the fourth equality is generated by both types of permutations. As a result, for all j, the vectors below are equal:

$$\tilde{\mathbf{B}}_{i_1,\ldots,i_{2m}} \prod_{k \neq j} x^{i_k} \tag{B.3}$$

and thus

$$\hat{\mathbf{B}}\mathbf{x}^{2m-1} = \tilde{\mathbf{B}}\mathbf{x}^{2m-1} \tag{B.4}$$

This means we could perform symmetric higher-order power iteration successfully, only using our partially symmetric $\tilde{\mathbf{B}}$ rather than the fully symmetric $\hat{\mathbf{B}}$ and yield the exact same steps at each iteration. In fact, this opens up the avenue to an even simpler and more efficient version of power iteration that directly relies on $\mathbf{B}$:

$$(\hat{\mathbf{B}}\mathbf{x}^{2m-1})_j = (\tilde{\mathbf{B}}\mathbf{x}^{2m-1})_j = (\mathbf{B}\mathbf{x}^{m-1})_j^{i_1} \boldsymbol{\delta}_{i_1,i_2} (\mathbf{B}\mathbf{x}^{m})^{i_2} \tag{B.5}$$

The rightmost expression can be obtained by first calculating the matrix $\mathbf{B}\mathbf{x}^{m-1}$, then calculating the vector $\mathbf{B}\mathbf{x}^{m} = (\mathbf{B}\mathbf{x}^{m-1})\mathbf{x}$ by a single matrix vector product. Then, a final matrix vector product between the two gives the result from Eq. B.5.

B.2 Implementation of the $(2, \mathbf{D})$-Norm Computation

The tensor $\hat{\mathbf{B}}_{\mathbf{D}}$ is a supersymmetric tensor since $\hat{\mathbf{B}}$ is a supersymmetric tensor. Thus, symmetric higher-order power iteration could be applied directly to calculate the Z-eigenpair of $\hat{\mathbf{B}}_{\mathbf{D}}$. In order to save on operations, if the Cholesky decomposition is performed to compute a lower triangular $\mathbf{D}^{1/2}$, then one iteration of symmetric higher-order power iteration can be taken more efficiently with the following steps. First, given the current iterate $\mathbf{x}$, compute

$$\mathbf{z} = \mathbf{D}^{-1/2}\mathbf{x} \tag{B.6}$$

by forward substitution. Next, compute the vector

$$\hat{\mathbf{B}}(\mathbf{D}^{-1/2}\mathbf{x})^{2m-1} = \hat{\mathbf{B}}\mathbf{z}^{2m-1} \tag{B.7}$$

This can be performed efficiently as in Eq. B.5. Finally, the new iterate is given by back substitution to solve an upper triangular linear system to find

$$\hat{\mathbf{B}}_{\mathbf{D}}\mathbf{x}^{2m-1} = (\mathbf{D}^{1/2})^{-T}(\hat{\mathbf{B}}\mathbf{z}^{2m-1}) \tag{B.8}$$

which is the numerator of the next iterate of symmetric higher-order power iteration. Above, $\hat{\mathbf{B}}\mathbf{z}^{2m-1}$ is reinterpreted as a column vector to make the linear algebra operations to be performed more clear. The above sequence of operations can be derived in index notation:

$$\begin{aligned}
(\hat{\mathbf{B}}_{\mathbf{D}}\mathbf{x}^{2m-1})_k &= \hat{B}_{j_1\ldots j_{2m}}(\mathbf{D}^{-1/2})^{j_1}_{i_1}\ldots(\mathbf{D}^{-1/2})^{j_{2m-1}}_{i_{2m-1}}(\mathbf{D}^{-1/2})^{j_{2m}}_{k}x^{i_1}\ldots x^{i_{2m-1}} \qquad &(\text{B.9})\\
&= (\hat{\mathbf{B}}\mathbf{z}^{2m-1})_{j_{2m}}(\mathbf{D}^{-1/2})^{j_{2m}}_{k} \qquad &(\text{B.10})
\end{aligned}$$

In this argument, the result is a row vector (covariant vector) while the input $\mathbf{x}$ is assumed to be a column vector (contravariant vector).

B.3 Calculating TEMoN Using Shifted Symmetric Higher-Order Power Iteration

In order to find TEMoN, we solve two optimization problems over the unit ball, one for a positive case and one for a negative case:

$$\tau_m^{\pm} = \max_{\delta \mathbf{x}(t_0) \in \mathcal{B}_1} \frac{\pm \mathbf{C}^{(m)} \delta \mathbf{x}^m(t_0)}{\mathbf{C}^{(2)} \delta \mathbf{x}^2(t_0)} \tag{B.11}$$

$$\tau_{m,R} = R^{m-2} \max(\tau_m^+, \tau_m^-) \tag{B.12}$$

In either case, we reformulate the problem with a change of coordinates

$$\mathbf{y} = \mathbf{\Phi x} \tag{B.13}$$

and calculate the maximum Z-eigenpair of each of the two tensors given by

$$\pm \left(\mathbf{C}_{\mathbf{\Phi}}^{(m)} \right)_{i_1 \ldots i_m} = \pm \mathbf{C}^{(m)}_{j_1 \ldots j_m} \left(\mathbf{\Phi}^{-1} \right)^{j_1}_{i_1} \ldots \left(\mathbf{\Phi}^{-1} \right)^{j_m}_{i_m} \tag{B.14}$$

We can do so by performing shifted symmetric higher-order power iteration on the symmetrized tensor [68]. Let $\hat{\mathbf{C}}_{\mathbf{\Phi}}^{(m)}$ be the symmetrization of $\mathbf{C}_{\mathbf{\Phi}}^{(m)}$, and define

$$\alpha = (m-1) \sum_{i_1, \ldots, i_m} \left| \left(\hat{\mathbf{C}}_{\mathbf{\Phi}}^{(m)} \right)_{i_1 \ldots i_m} \right| \tag{B.15}$$

Then, symmetric shifted higher-order power iteration is guaranteed to converge to (a typically large) eigenvector of $\mathbf{C}_{\mathbf{\Phi}}^{(m)}$. The iteration is given:

$$\mathbf{y}_{n+1}^{\pm} = \frac{\pm \hat{\mathbf{C}}_{\mathbf{\Phi}}^{(m)} (\mathbf{y}_n^{\pm})^{m-1} + \alpha \mathbf{y}_n^{\pm}}{\left\| \pm \hat{\mathbf{C}}_{\mathbf{\Phi}}^{(m)} (\mathbf{y}_n^{\pm})^{m-1} + \alpha \mathbf{y}_n^{\pm} \right\|_2} \tag{B.16}$$

Using the inverse coordinate change on the converged to Z-eigenvector $\mathbf{y}^*$ we arrive at

$$\mathbf{x}_*^{\pm} = \mathbf{\Phi}^{-1} \mathbf{y}_*^{\pm} \tag{B.17}$$

Finally, our optimization is given by

$$\tau_m^{\pm} = \frac{\pm \mathbf{C}^{(m)}(\mathbf{x}_*^{\pm})^m}{\mathbf{C}^{(2)}(\mathbf{x}_*^{\pm})^2} \tag{B.18}$$

The CGTs have fewer symmetries than the STTs and their squares. As a result, we do not present a method leveraging partial symmetry for computing TEMoN without performing symmetrization as we do in the case of DEMoN.

BIBLIOGRAPHY

[1] National aeronautics and space administration (nasa) white paper: Gateway destination orbit model: A continuous 15 year nrho reference trajectory. 2019.

[2] Ayman M Abdallah, Brett A Newman, and Ashraf M Omran. Measuring aircraft nonlinearity across aerodynamic attitude flight envelope. In *AIAA Atmospheric Flight Mechanics (AFM) Conference*, page 4985, 2013.

[3] Alain Albouy and Antonio J Urena. Some simple results about the lambert problem. *The European Physical Journal Special Topics*, 229:1405–1417, 2020.

[4] KT Alfriend and H Yan. Evaluation and comparison of relative motion theories. *Journal of Guidance, Control, and Dynamics*, 28(2):254–261, 2005.

[5] J-S Ardaens, Gabriella Gaias, et al. Fast angles-only initial relative orbit determination for onboard application. In *10th International Workshop on Satellite Constellations and Formation Flying IWSCFF 19-38*, pages 1–8, 2019.

[6] Jean-Sébastien Ardaens and Gabriella Gaias. A numerical approach to the problem of angles-only initial relative orbit determination in low earth orbit. *Advances in Space Research*, 63(12):3884–3899, 2019.

[7] Roberto Armellin and Pierluigi Di Lizia. Probabilistic optical and radar initial orbit determination. *Journal of Guidance, Control, and Dynamics*, 41(1):101–118, 2018.

[8] Ahmad Bani Younes. Exact computation of high-order state transition tensors for perturbed orbital motion. *Journal of Guidance, Control, and Dynamics*, 42(6):1365–1371, 2019.

[9] Austin R Benson and David F Gleich. Computing tensor z-eigenvectors with dynamical systems. *SIAM Journal on Matrix Analysis and Applications*, 40(4):1311–1324, 2019.

[10] Oliver Boodram, Spencer Boone, and Jay McMahon. Efficient nonlinear spacecraft navigation using directional state transition tensors. 2022.

[11] Spencer Boone and Jay Mcmahon. Rapid local trajectory optimization using higher-order state transition tensors and differential dynamic programming. In *2020 AAS/AIAA Astrodynamics Specialist Conference*, 08 2020.

[12] Spencer Boone and Jay McMahon. Orbital guidance using higher-order state transition tensors. *Journal of Guidance, Control, and Dynamics*, 44(3):493–504, 2021.

[13] Spencer Boone and Jay McMahon. Variable time-of-flight spacecraft maneuver targeting using state transition tensors. *Journal of Guidance, Control, and Dynamics*, 44(11):2072–2080, 2021.

[14] Spencer Boone and Jay McMahon. Directional state transition tensors for capturing dominant nonlinear effects in orbital dynamics. *Journal of Guidance, Control, and Dynamics*, pages 1–12, 2022.

[15] Spencer Boone and Jay McMahon. Directional state transition tensors for capturing dominant nonlinear effects in orbital dynamics. *Journal of Guidance, Control, and Dynamics*, 46(3):431–442, 2023.

[16] Arthur E Bryson and Yu-Chi Ho. *Applied optimal control: optimization, estimation, and control.* Routledge, 2018.

[17] TE Carter and J Brient. Optimal bounded-thrust space trajectories based on linear equations. *Journal of Optimization Theory and Applications*, 70(2):299–317, 1991.

[18] Thomas Carter and John Brient. Fuel-optimal rendezvous for linearized equations of motion. *Journal of Guidance, Control, and Dynamics*, 15(6):1411–1416, 1992.

[19] Thomas Carter and Mayer Humi. Fuel-optimal rendezvous near a point in general keplerian orbit. *Journal of Guidance, Control, and Dynamics*, 10(6):567–573, 1987.

[20] Thomas E Carter. New form for the optimal rendezvous equations near a keplerian orbit. *Journal of Guidance, Control, and Dynamics*, 13(1):183–186, 1990.

[21] Thomas E Carter and Cyrus J Pardis. Optimal power-limited rendezvous with upper and lower bounds on thrust. *Journal of Guidance, Control, and Dynamics*, 19(5):1124–1133, 1996.

[22] Huan Chen, Chao Han, Yinrui Rao, Jianfeng Yin, and Xiucong Sun. Algorithm of relative lambert transfer based on relative orbital elements. *Journal of Guidance, Control, and Dynamics*, 42(6):1413–1422, 2019.

[23] Michelle Chernick and Simone D'Amico. Closed-form optimal impulsive control of spacecraft relative motion using reachable set theory. *arXiv preprint arXiv:2002.07832*, 2020.

[24] WH Clohessy and RS Wiltshire. Terminal guidance system for satellite rendezvous. *Journal of the Aerospace Sciences*, 27(9):653–658, 1960.

[25] John L Crassidis. What is navigation? *Journal of Guidance, Control, and Dynamics*, 45(5):792–794, 2022.

[26] David Cunningham and Ryan P Russell. An interpolated second-order relative motion model for gateway. *The Journal of the Astronautical Sciences*, 70(4):26, 2023.

[27] Simone D'Amico and Oliver Montenbruck. Proximity operations of formation-flying spacecraft using an eccentricity/inclination vector separation. *Journal of Guidance, Control, and Dynamics*, 29(3):554–563, 2006.

[28] Zhaohui Dang. New state transition matrix for relative motion on an arbitrary keplerian orbit. *Journal of Guidance, Control, and Dynamics*, 40(11):2917–2927, 2017.

[29] Zhaohui Dang. Solutions of tschauner–hempel equations. *Journal of Guidance, Control, and Dynamics*, 40(11):2956–2960, 2017.

[30] Saptarshi Das and Arnold Neumaier. Solving overdetermined eigenvalue problems. *SIAM Journal on Scientific Computing*, 35(2):A541–A560, jan 2013.

[31] Ryan P. Russell David A. Cunningham. A second order relative motion model for gateway. In *45th Rocky Mountain AAS GNC Conference*, 2022.

[32] Lieven De Lathauwer, Bart De Moor, and Joos Vandewalle. On the best rank-1 and rank-(r 1, r 2,..., rn) approximation of higher-order tensors. *SIAM journal on Matrix Analysis and Applications*, 21(4):1324–1342, 2000.

[33] PIERLUIGI Di Lizia, ROBERTO Armellin, FRANCO Bernelli-Zazzera, and

M Berz. High order optimal control of space trajectories with uncertain boundary conditions. *Acta Astronautica*, 93:217–229, 2014.

[34] Konstantinos Drakakis and Barak A Pearlmutter. On the calculation of the l2→ l1 induced matrix norm. *International Journal of Algebra*, 3(5):231–240, 2009.

[35] Theodore N Edelbaum. Optimum low-thrust rendezvous and station keeping. *AIAA Journal*, 2(7):1196–1201, 1964.

[36] Ian Elliott and Natasha Bosanac. Impulsive control of formations near invariant tori via local toroidal coordinates. In *AAS/AIAA Astrodynamics Specialist Conference*, 2021.

[37] Robert J Fitzgerald. Pinch points of debris from a satellite breakup. *Journal of guidance, control, and dynamics*, 21(5):813–815, 1998.

[38] Thibault LB Flinois, Daniel P Scharf, Carl R Seubert, Michael Bottom, and Stefan R Martin. Starshade formation flying ii: formation control. *Journal of Astronomical Telescopes, Instruments, and Systems*, 6(2):029001, 2020. [doi:10.1117/1.JATIS.6.2.029001].

[39] Giovanni Franzini, Mario Innocenti, and Massimo Casasco. An adjoint-based method for continuous-thrust relative maneuver computation in the restricted three-body problem. In *2021 American Control Conference (ACC)*, pages 4276–4281. IEEE, 2021.

[40] Pierre Gaspard. *Chaos, scattering and statistical mechanics*, chapter Liouvillian Dynamics. Number 9. Cambridge University Press, 2005.

[41] B Scott Gaudi, Sara Seager, Bertrand Mennesson, Alina Kiessling, Keith Warfield, Kerri Cahoy, John T Clarke, Shawn Domagal-Goldman, Lee Feinberg, Olivier Guyon, et al. The habitable exoplanet observatory (habex) mission concept study final report. *arXiv*, 2020.

[42] David K Geller and Itzik Klein. Angles-only navigation state observability during orbital proximity operations. *Journal of Guidance, Control, and Dynamics*, 37(6):1976–1983, 2014.

[43] David K Geller and T Alan Lovell. Angles-only initial relative orbit determination performance analysis using cylindrical coordinates. *The Journal of the Astronautical Sciences*, 64(1):72–96, 2017.

[44] David K Geller and Alex Perez. Initial relative orbit determination for close-in proximity operations. *Journal of Guidance, Control, and Dynamics*, 38(9):1833–1842, 2015.

[45] Eberhard Gill, Simone D'Amico, and Oliver Montenbruck. Autonomous formation flying for the prisma mission. *Journal of Spacecraft and Rockets*, 44(3):671–681, 2007.

[46] Gene H Golub and Charles F Van Loan. *Matrix computations*, chapter 8.6.4. JHU press, 4 edition, 2013.

[47] Baichun Gong, David K Geller, and Jianjun Luo. Initial relative orbit determination analytical covariance and performance analysis for proximity operations. *Journal of Spacecraft and Rockets*, 53(5):822–835, 2016.

[48] Baichun Gong, Wendan Li, Shuang Li, Weihua Ma, and Lili Zheng. Angles-only initial relative orbit determination algorithm for non-cooperative spacecraft proximity operations. *Astrodynamics*, 2:217–231, 2018.

[49] Daniel Griffith, James Turner, Srinivas Vadali, and John Junkins. Higher order sensitivities for solving nonlinear two-point boundary-value problems. In *AIAA/AAS Astrodynamics Specialist Conference and Exhibit*, page 5404, 2004.

[50] John D Hadjidemetriou. Some properties of the solution of the first-order variational equations of the restricted three-body problem. *The Astronomical Journal*, 72:865, 1967.

[51] George William Hill. Researches in the lunar theory. *American journal of Mathematics*, 1(1):5–26, 1878.

[52] Kathleen C Howell and Brian T Barden. Trajectory design and stationkeeping for multiple spacecraft in formation near the sun-earth l1 point. In *IAF 50th International Astronautical Congress*, pages 4–8, 1999.

[53] Kathleen C Howell and Belinda G Marchand. Natural and non-natural spacecraft formations near the l1 and l2 libration points in the sun–earth/moon ephemeris system. *Dynamical Systems*, 20(1):149–173, 2005.

[54] Erica L Jenson and Daniel J Scheeres. Semianalytical measures of nonlinearity based on tensor eigenpairs. *Journal of Guidance, Control, and Dynamics*, pages 1–16, 2022.

[55] Erica L Jenson and Daniel J Scheeres. Bounding nonlinear stretching about spacecraft trajectories using tensor eigenpairs. *Acta Astronautica*, 214:159–166, 2024.

[56] Fanghua Jiang, Junfeng Li, Hexi Baoyin, and Yunfeng Gao. Two-point boundary value problem solutions to spacecraft formation flying. *Journal of guidance, control, and dynamics*, 32(6):1827–1837, 2009.

[57] John L Junkins. von karman lecture: Adventures on the interface of dynamics and control. *Journal of Guidance, Control, and Dynamics*, 20(6):1058–1071, 1997.

[58] John L Junkins and Puneet Singla. How nonlinear is it? a tutorial on nonlinearity of orbit and attitude dynamics. *The Journal of the Astronautical Sciences*, 52(1):7–60, 2004.

[59] John L Junkins, James D Turner, and Manoranjan Majji. Generalizations and applications of the lagrange implicit function theorem. *The Journal of the Astronautical Sciences*, 57(1-2):313–345, 2009.

[60] Dean R Keithly, Dmitry Savransky, Daniel Garrett, Christian Delacroix, and Gabriel Soto. Optimal scheduling of exoplanet direct imaging single-visit observations of a blind search survey. *Journal of Astronomical Telescopes, Instruments, and Systems*, 6(2):027001, 2020. [doi:10.1117/1.JATIS.6.2.027001].

[61] Patrick Kelly, Vishala Arya, Junkins L. John, and Manoranjan Majji. Nonlinearity index for state-costate dynamics of optimal control problems. 2022.

[62] Patrick Kelly, Andrew J Sinclair, and Manoranjan Majji. Higher order state transition tensors for keplerian motion using universal parameters. 2020.

[63] Craig A Kluever. What is control?, 2023.

[64] Adam W Koenig and Simone D'Amico. Observability-aware numerical algorithm for angles-only initial relative orbit determination. In *2020 AAS/AIAA Astrodynamics Specialist Conference*, 2020.

[65] Adam W Koenig, Simone D'Amico, Bruce Macintosh, and Charles J Titus. Optimal formation design of a miniaturized distributed occulter/telescope in earth orbit. In *Proceedings of the AIAA/AAS Astrodynamics Specialist Conference*, 2015.

[66] Eleftherios Kofidis and Phillip A Regalia. On the best rank-1 approximation of higher-order supersymmetric tensors. *SIAM Journal on Matrix Analysis and Applications*, 23(3):863–884, 2002.

[67] Tamara G Kolda and Brett W Bader. Matlab tensor toolbox. Technical report, Sandia National Laboratories (SNL), Albuquerque, NM, and Livermore, CA . . . , 2006.

[68] Tamara G Kolda and Jackson R Mayo. Shifted power method for computing tensor eigenpairs. *SIAM Journal on Matrix Analysis and Applications*, 32(4):1095–1124, 2011.

[69] Tamara G Kolda and Jackson R Mayo. An adaptive shifted power method for computing generalized tensor eigenpairs. *SIAM Journal on Matrix Analysis and Applications*, 35(4):1563–1581, 2014.

[70] Egemen Kolemen and N Jeremy Kasdin. Optimization of an occulter-based extrasolar-planet-imaging mission. *Journal of Guidance, Control, and Dynamics*, 35(1):172–185, 2012.

[71] Wang Sang Koon, Martin W Lo, Jerrold E Marsden, and Shane D Ross. Dynamical systems, the three-body problem and space mission design. In *Equadiff 99: (In 2 Volumes)*, chapter 2, pages 1167–1181. World Scientific, 2000.

[72] Jackson Kulik. An in-plane j2-invariance condition and control algorithm for highly elliptical satellite formations. *Celestial Mechanics and Dynamical Astronomy*, 133(2):1–25, 2021.

[73] Jackson Kulik, William Clark, and Dmitry Savransky. State transition tensors for continuous-thrust control of three-body relative motion. *Journal of Guidance, Control, and Dynamics*, pages 1–10, 2023.

[74] Jackson Kulik, Owen Oertell, and Dmitry Savransky. Overdetermined eigenvector approach to passive angles-only relative orbit determination. *Journal of Guidance, Control, and Dynamics*, pages 1–9, 2024.

[75] Jackson Kulik and Dmitry Savransky. Precomputation and interpolation of the matrizant for starshade slewing. In *Space Telescopes and Instrumentation 2022: Optical, Infrared, and Millimeter Wave*. SPIE, 2022.

[76] Jackson Kulik and Dmitry Savransky. Relative transfer singularities and

multi-revolution lambert uniqueness. In *AIAA SCITECH 2022 Forum*, page 0958, 2022.

[77] Keith A LeGrand, Kyle J DeMars, and Henry J Pernicka. Bearings-only initial relative orbit determination. *Journal of Guidance, Control, and Dynamics*, 38(9):1699–1713, 2015.

[78] Catherine A Lembeck and John E Prussing. Optimal impulsive intercept with low-thrust rendezvous return. *Journal of Guidance, Control, and Dynamics*, 16(3):426–433, 1993.

[79] Kenneth Levenberg. A method for the solution of certain non-linear problems in least squares. *Quarterly of applied mathematics*, 2(2):164–168, 1944.

[80] Andrew D Lewis. A top nine list: Most popular induced matrix norms. *Queen's University, Kingston, Ontario, Tech. Rep*, pages 1–13, 2010.

[81] Shigui Li, Zhen Chen, Chaoqian Li, and Jianxing Zhao. Eigenvalue bounds of third-order tensors via the minimax eigenvalue of symmetric matrices. *Computational and Applied Mathematics*, 39:1–14, 2020.

[82] Lek-Heng Lim. Singular values and eigenvalues of tensors: a variational approach. In *1st IEEE International Workshop on Computational Advances in Multi-Sensor Adaptive Processing, 2005.*, pages 129–132. IEEE, 2005.

[83] P Di Lizia, Roberto Armellin, and Michèle Lavagna. Application of high order expansions of two-point boundary value problems to astrodynamics. *Celestial Mechanics and Dynamical Astronomy*, 102:355–375, 2008.

[84] Matteo Losacco, Alberto Fossà, and Roberto Armellin. Low-order automatic domain splitting approach for nonlinear uncertainty mapping. *Journal of Guidance, Control, and Dynamics*, 47(2):291–310, 2024.

[85] T Alan Lovell, Andrew J Sinclair, and Brett Newman. Angles only initial orbit determination: Comparison of relative dynamics and inertial dynamics approaches with error analysis. In *2018 Space Flight Mechanics Meeting*, page 0475, 2018.

[86] Thomas A Lovell and David A Spencer. Relative orbital elements formulation based upon the clohessy-wiltshire equations. *The Journal of the Astronautical Sciences*, 61(4):341–366, 2014.

[87] Ping Lu. Introducing computational guidance and control, 2017.

[88] Ping Lu. What is guidance?, 2021.

[89] Manoranjan Majji, John Junkins, and James Turner. Jth moment extended kalman filtering for estimation of nonlinear dynamic systems. In *AIAA Guidance, Navigation and Control Conference and Exhibit*, page 7386, 2008.

[90] Manoranjan Majji, John L Junkins, and James D Turner. A high order method for estimation of dynamic systems. *The Journal of the Astronautical Sciences*, 56(3):401–440, 2008.

[91] Donald W Marquardt. An algorithm for least-squares estimation of nonlinear parameters. *Journal of the society for Industrial and Applied Mathematics*, 11(2):431–441, 1963.

[92] Oliver Montenbruck, Eberhard Gill, and Fh Lutze. Satellite orbits: models, methods, and applications. *Appl. Mech. Rev.*, 55(2):B27–B28, 2002.

[93] Larry D Mullins. Initial value and two point boundary value solutions to the clohessy-wiltshire equations. *Journal of the Astronautical Sciences*, 40(4):487–501, 1992.

[94] Chandeok Park, Vincent Guibout, and Daniel J Scheeres. Solving optimal continuous thrust rendezvous problems with generating functions. *Journal of Guidance, Control, and Dynamics*, 29(2):321–331, 2006.

[95] Ryan S Park and Daniel J Scheeres. Nonlinear mapping of gaussian statistics: theory and applications to spacecraft trajectory design. *Journal of guidance, Control, and Dynamics*, 29(6):1367–1375, 2006.

[96] Samuel Pedrotty, Ronney Lovelace, John Christian, Devin Renshaw, and Grace Quintero. Design and performance of an open-source star tracker algorithm on commercial off-the-shelf cameras and computers. In *Annual AAS Guidance, Navigation and Control Conference*, number JSC-E-DAA-TN77360, 2020.

[97] Etienne Pellegrini and Ryan P Russell. On the computation and accuracy of trajectory state transition matrices. *Journal of Guidance, Control, and Dynamics*, 39(11):2485–2499, 2016.

[98] AC Perez, DK Geller, and TA Lovell. Non-iterative angles-only initial relative

orbit determination with j2 perturbations. *Acta Astronautica*, 151:146–159, 2018.

[99] Henry J Pernicka, Brian A Carlson, and SN Balakrishnan. Spacecraft formation flight about libration points using impulsive maneuvering. *Journal of Guidance, Control, and Dynamics*, 29(5):1122–1130, 2006.

[100] Liqun Qi, Yiju Wang, and Ed X Wu. D-eigenvalues of diffusion kurtosis tensors. *Journal of Computational and Applied Mathematics*, 221(1):150–157, 2008.

[101] Mirco Rasotto, Alessandro Morselli, Alexander Wittig, Mauro Massari, Pierluigi Di Lizia, Roberto Armellin, Celia Valles, and Guillermo Ortega. Differential algebra space toolbox for nonlinear uncertainty propagation in space dynamics. 2016.

[102] Hanno Rein and Daniel Tamayo. Second-order variational equations for n-body simulations. *Monthly Notices of the Royal Astronomical Society*, 459(3):2275–2285, 2016.

[103] Christopher WT Roscoe, Srinivas R Vadali, Kyle T Alfriend, and Uri P Desai. Optimal formation design for magnetospheric multiscale mission using differential orbital elements. *Journal of Guidance, Control, and Dynamics*, 34(4):1070–1080, 2011.

[104] William David Sanchez. *Towards fuel-efficient formation flying of an observatory and external occulter at Sun-Earth L2.* PhD thesis, Massachusetts Institute of Technology, 2020.

[105] Hanspeter Schaub and Kyle T Alfriend. Impulsive feedback control to establish specific mean orbit elements of spacecraft formations. *Journal of Guidance, Control, and Dynamics*, 24(4):739–745, 2001.

[106] S. F. Schmidt. The kalman filter-its recognition and development for aerospace applications. *Journal of Guidance and Control*, 4(1):4–7, 1 1981.

[107] Sara Seager, Margaret Turnbull, William Sparks, Mark Thomson, Stuart B Shaklan, Aki Roberge, Marc Kuchner, N Jeremy Kasdin, Shawn Domagal-Goldman, Webster Cash, et al. The exo-s probe class starshade mission. In *Techniques and Instrumentation for Detection of Exoplanets VII*, volume 9605, page 96050W. International Society for Optics and Photonics, 2015. [doi:10.1117/12.2190378].

[108] Simone Servadio, Renato Zanetti, and Roberto Armellin. Maximum a posteriori estimation of hamiltonian systems with high order taylor polynomials. *The Journal of the Astronautical Sciences*, 69(2):511–536, 2022.

[109] Rüdiger Seydel. Numerical computation of branch points in ordinary differential equations. *Numerische Mathematik*, 32(1):51–68, 1979.

[110] Malcolm David Shuster and S D_ Oh. Three-axis attitude determination from vector observations. *Journal of guidance and Control*, 4(1):70–77, 1981.

[111] Andrew J Sinclair and T Alan Lovell. Optimal linear orbit determination. *Journal of Guidance, Control, and Dynamics*, 43(3):628–632, 2020.

[112] Andrew J Sinclair, Ryan E Sherrill, and T Alan Lovell. Calibration of linearized solutions for satellite relative motion. *Journal of Guidance, Control, and Dynamics*, 37(4):1362–1367, 2014.

[113] Dan Sirbu, Christian Vad Karsten, and N Jeremy Kasdin. Dynamical performance for science-mode stationkeeping with an external occulter. In *Space Telescopes and Instrumentation 2010: Optical, Infrared, and Millimeter Wave*, volume 7731, page 773152. International Society for Optics and Photonics, 2010. [doi:10.1117/12.856361].

[114] William Marshall Smart, WM Smart, and RM Green. *Textbook on spherical astronomy*. Cambridge University Press, 1977.

[115] Gabriel Soto, Dean Keithly, Daniel Garrett, Christian Delacroix, and Dmitry Savransky. Optimal starshade observation scheduling. In *Space Telescopes and Instrumentation 2018: Optical, Infrared, and Millimeter Wave*, volume 10698, page 106984M. International Society for Optics and Photonics, 2018. [doi:10.1117/12.2311771].

[116] Gabriel J Soto, Dmitry Savransky, Daniel Garrett, and Christian Delacroix. Parameterizing the search space of starshade fuel costs for optimal observation schedules. *Journal of Guidance, Control, and Dynamics*, 42(12):2671–2676, 2019.

[117] Gabriel J Soto, Dmitry Savransky, and Rhonda Morgan. Analytical model for starshade formation flying with applications to exoplanet direct imaging observation scheduling. *Journal of Astronomical Telescopes, Instruments, and Systems*, 7(2):021209, 2021. [doi:10.1117/1.JATIS.7.2.021209].

[118] Robert Stern. Singularities in the analytic solution of the linearized variationalequations of elliptical motion. In *1st AIAA Annual Meeting*, page 398, 1964.

[119] F-T Sun. On the minimum time trajectory and multiple solutions of lambert's problem. In *American Institute of Aeronautics and Astronautics Conference*, 1979.

[120] Victory Szebehely. *Theory of orbit: The restricted problem of three Bodies.* Elsevier, 2012.

[121] Daniel P Tapolcai, Ashraf Omran, and Brett Newman. Aircraft stall phenomenon analysis using nonlinearity index theory. *Aerospace Science and Technology*, 68:288–298, 2017.

[122] Françoise Tisseur and Karl Meerbergen. The quadratic eigenvalue problem. *SIAM review*, 43(2):235–286, 2001.

[123] J Tschauner and P Hempel. Rendezvous zu einem in elliptischer bahn umlaufenden ziel. *Astronautica Acta*, 11(2):104–+, 1965.

[124] Kirsten Elizabeth Tuggle. *Model selection for Gaussian mixture model filtering and sensor scheduling.* PhD thesis, 2020.

[125] James D Turner, Manoranjan Majji, and JL Junkins. Aas 09-441 arbitrary order vector reversion of series and implicit function theorem.

[126] David A Vallado. *Fundamentals of astrodynamics and applications*, volume 4, chapter 1. Springer Science & Business Media, 2001.

[127] Monica Valli, Roberto Armellin, Pierluigi Di Lizia, and MR Lavagna. Nonlinear mapping of uncertainties in celestial mechanics. *Journal of Guidance, Control, and Dynamics*, 36(1):48–63, 2013.

[128] Pauli Virtanen, Ralf Gommers, Travis E. Oliphant, Matt Haberland, Tyler Reddy, David Cournapeau, Evgeni Burovski, Pearu Peterson, Warren Weckesser, Jonathan Bright, Stéfan J. van der Walt, Matthew Brett, Joshua Wilson, K. Jarrod Millman, Nikolay Mayorov, Andrew R. J. Nelson, Eric Jones, Robert Kern, Eric Larson, C J Carey, İlhan Polat, Yu Feng, Eric W. Moore, Jake VanderPlas, Denis Laxalde, Josef Perktold, Robert Cimrman, Ian Henriksen, E. A. Quintero, Charles R. Harris, Anne M. Archibald, Antônio H. Ribeiro, Fabian Pedregosa, Paul van Mulbregt, and SciPy 1.0

Contributors. SciPy 1.0: Fundamental Algorithms for Scientific Computing in Python. *Nature Methods*, 17:261–272, 3 2020.

[129] Changxuan Wen and Pini Gurfil. Relative reachable domain for spacecraft with initial state uncertainties. *Journal of Guidance, Control, and Dynamics*, 39(3):462–473, 2016.

[130] Changxuan Wen, Yushan Zhao, Baojun Li, and Peng Shi. Solving the relative lambert's problem and accounting for its singularities. *Acta Astronautica*, 97:122–129, 2014.

[131] Changxuan Wen, Yushan Zhao, and Peng Shi. Precise determination of reachable domain for spacecraft with single impulse. *Journal of Guidance, Control, and Dynamics*, 37(6):1767–1779, 2014.

[132] Matthew Willis and Simone D'Amico. Applications and limitations of angles-only relative navigation using polynomial solutions. In *AAS/AIAA Astrodynamics Specialist Conference, South Lake Tahoe, CA*, 2020.

[133] Matthew Willis and Simone D'Amico. Fast angles-only relative navigation using polynomial dynamics. *Advances in Space Research*, 2023.

[134] Alexander Wittig, Pierluigi Di Lizia, Roberto Armellin, Kyoko Makino, Franco Bernelli-Zazzera, and Martin Berz. Propagation of large uncertainty sets in orbital dynamics by automatic domain splitting. *Celestial Mechanics and Dynamical Astronomy*, 122:239–261, 2015.

[135] David C Woffinden and David K Geller. Relative angles-only navigation and pose estimation for autonomous orbital rendezvous. *Journal of Guidance, Control, and Dynamics*, 30(5):1455–1469, 2007.

[136] Koji Yamanaka and Finn Ankersen. New state transition matrix for relative motion on an arbitrary elliptical orbit. *Journal of guidance, control, and dynamics*, 25(1):60–66, 2002.

[137] Max Williams Yates. *Angles-only navigation technique for maneuver-free spacecraft proximity operations*. PhD thesis, Massachusetts Institute of Technology, 2017.

[138] Renato Zanetti, Kyle J DeMars, and Robert H Bishop. Underweighting nonlinear measurements. *Journal of guidance, control, and dynamics*, 33(5):1670–1675, 2010.

[139] Gang Zhang and Di Zhou. A second-order solution to the two-point boundary value problem for rendezvous in eccentric orbits. *Celestial Mechanics and Dynamical Astronomy*, 107:319–336, 2010.